UNIVERSITY OF CALIFORNIA

Santa Barbara

Ultra-Narrow Bandwidth Optical Resonators for Integrated Low Frequency Noise Lasers

A dissertation submitted in partial satisfaction of the

requirements for the degree Doctor of Philosophy

in Electrical and Computer Engineering

by

Daryl T. Spencer

Committee in charge:

Professor John E. Bowers, Chair

Professor Rod Alferness

Professor Nadir Dagli

Professor Luke Theogarajan

March 2016

The dissertation of Daryl T. Spencer is approved.

_____

Rod Alferness

_____

Nadir Dagli

_____

Luke Theogarajan

_____

John E. Bowers, Committee Chair

March 2016

Ultra-Narrow Bandwidth Optical Resonators for Integrated Low Frequency Noise Lasers

Acknowledgements

There are many people to thank who have helped me along my journey. Beginning in the small town of Hillsboro, Missouri, my parents Daryl and Julie always encouraged me to strive for my dreams. There were no limits, but starting small gives you a good perspective to always achieve bigger and greater things. My passions led me out of Hillsboro to the University of Tulsa, where I quickly found a calling in the Physics department. Studying at a mostly undergraduate research university really nurtured my scientific research abilities, and Dr. Parameswar Hari was instrumental in my first experiences of conference presentations and publications.

TU gave me a great college experience, and it was where I met many lifelong friends as well as my wife, Elizabeth. We both had big dreams for post-undergraduate, and shared a passion for travel and new experiences. She has been willing to follow me across the country and be there for all of my joys and challenges at UCSB. Moving to the West Coast has broadened our Midwestern perspectives, and I'm so happy to have her celebrating with me for my PhD.

As I started my undergraduate internship in Professor Bowers' group, I knew that UCSB was a top tier school that I wanted to go to. My first summer in the group was indeed lucky with working devices and big on good impressions. John was great with all students and was always pushing us for great results. Di Liang was a fantastic mentor, and my NNIN group made my time fun and exciting. As I transitioned to graduate school, my first year TA was invaluable in developing my passion for teaching others. Professors Umesh Mishra, Luke

Theogarajan, and John Bowers challenged me all the way and gave me ample independent opportunities to hone my skills.

My graduate school career was made truly amazing under the mentorship of John. He has always pushed his students to greatness, while still knowing when to have some fun skiing or throwing parties with his wonderful wife Ariel. Dean Rod Alferness, Professor Nadir Dagli, Professor Theogaragan were a wonderful committee and helped to enhance my confidence while presenting well rounded research throughout my qualifier and defense. I'd also like to thank Professor Dan Blumenthal, Professor Adel Saleh, and the Lionix team of Arne Liense, Hans Vlekkert, Rene Heideman, and Theo Veenstra for their help throughout my thesis.

My research was launched under the guidance of Yongbo Tang, and many senior students helped me to become the experimenter I am today, including Jared Bauters, Jason Tien, Alex Fang, Jock Bovington, Geza Kurczveil, Ben Curtin, Hui-Wen Chen, Siddharth Jain, Abi Sivananthan, Mingzhi Lu, Erik Norberg, Rob Guzzon, Wenzao Li, Chin-han Lin, Kim Nguyen, John Garcia, Erica Lively, Demis John, and others. I am happy to finish my stint as the lab manager, passed on by Anand Ramaswamy and Molly Piels, other lab grinders who taught me a lot about practical lab work. My peers in the program have made this time special, from the screening exam, happy hours, surviving long lab hours, and up to my defense, including Sudharsanan Srinivasan, Mike Davenport, Chong Zhang, Prateek Choudhary, Bugra Kaytanli, Alan Liu, Tony Huang, Jared Hulme, Renan Moreira, Michael Belt, Lin Chang, Sarat Chandra, Alex Spott, Avantika Sodhi, Andreas De Groote, Eric Stanton, Minh Tran, Yichen Shen, Alfredo Torres, Nick Julian, Danielle Guerra, Aaron Bluestone, and others. Of course, no group of wild grad students can do anything efficiently without great postdocs and smart visiting scholars guiding them, including Martijn Heck,

Dedicated to my family

Curriculum Vitae

<u>PERSONAL</u>

Full Name: **Daryl Tipton Spencer II**
Born: Hillsboro, MO
Email: spencer.darylt@gmail.com

<u>EDUCATION</u>

University of California Santa Barbara, Santa Barbara, CA
M.S. in Electrical and Computer Engineering, March 2012
PhD. in Electrical and Computer Engineering, March 2016
• Focus: Electronics and Photonics
• Overall GPA 3.80/4.0

The University of Tulsa, Tulsa, OK
B.S. in Engineering Physics, May 2010
• Focus: Electronics
• Minor: Mathematics
• Overall GPA 3.89/4.0

<u>RELEVANT GRADUATE COURSEWORK & SKILLS</u>

• E&M, Semiconductor Lasers, Semiconductor Processing, Device Physics, Solid State Physics, Quantum Mechanics, Business Strategy
• Active/passive device testing, high resolution wavelength spectroscopy, high speed bulk/on chip characterization, wafer bonding, low microwave phase noise metrology

<u>EXPERIENCE</u>

Teaching Assistant, UCSB ECE Department, Santa Barbara, CA   2010-2011

Student Researcher, TU Physics Department, Tulsa, OK   2007-2010

Student Researcher, NNIN REU, UCSB, Summer 2009

Student Researcher, NanoJapan, Sendai University, Summer 2008

Tutor, TUTV, University of Tulsa, Fall 2008 – 2010

ACTIVITIES/ INTEREST

- IEEE Photonics Society
- Optical Society of America
- TU Club Volleyball
- Kappa Alpha Order
- Society of Physics Students
- Eagle Scout

AWARDS/HONORS

- National Science Foundation Graduate Research Fellowship
- UCSB ECE Dissertation Fellowship
- Mortar Board Honor Society
- Sigma Pi Sigma Physics Honor Society
- Tau Beta Pi Engineering Honor Society
- 2 Student Research Grants awarded by the University of Tulsa
- 3 Kappa Alpha Order Merit Based Scholarships

PATENTS

1) S. Srinivasan, J. Bowers, M. Heck, and **D. Spencer**, "Ultralow loss waveguide aided high Q filters for microwave applications," Submitted patent disclosure.

2) L. A. Johansson, J. Bowers, D. Guerra, L. Theogarajan, **D. Spencer**, M. Heck, S. Srinivasan, and Y. Tang, "Novel low phase noise optoelectronic oscillators," Submitted patent disclosure.

JOURNAL PUBLICATIONS

1) **D. T. Spencer**, M. L. Davenport, T. Komljenovic, S. Srinivasan, and J. E. Bowers, "Stabilization of heterogeneous silicon lasers using Pound-Drever-Hall locking to Si_3N_4 ring resonators," submitted to *Optics Express.*

2) **D. T. Spencer**, M. Davenport, S. Srinivasan, J. Khurgin, P. A. Morton, and J. E. Bowers, "Low kappa, narrow bandwidth Si_3N_4 Bragg gratings," *Opt. Express*, vol. 23, no. 23, p. 30329, Nov. 2015.

3) **D. T. Spencer**, J. F. Bauters, M. J. R. Heck, and J. E. Bowers, "Integrated waveguide coupled Si_3N_4 resonators in the ultrahigh-Q regime," *Optica*, vol. 1, no. 3, p. 153, Sep. 2014.

4) **D. T. Spencer**, D. Dai, Y. Tang, M. J. R. Heck, and J. E. Bowers, "Realization of a novel 1xN power splitter with uniformly excited ports," *Photonics Technology Letters, IEEE* , vol.25, no.1, pp.36-39, Jan. 1, 2013.

5) C. J. Krückel, V. Torres-Company, P. A. Andrekson, **D. T. Spencer**, J. F. Bauters, M. J. R. Heck, and J. E. Bowers, "Continuous wave-pumped wavelength conversion in low-loss silicon nitride waveguides," *Opt. Lett.*, vol. 40, no. 6, p. 875, Mar. 2015.

6) A. Bluestone, **D. T. Spencer**, S. Srinivasan, D. Guerra, J. E. Bowers, and L. Theogarajan, "An Ultra-Low Phase-Noise 20-GHz PLL Utilizing an Optoelectronic Voltage-Controlled Oscillator," *IEEE Trans. Microw. Theory Tech.*, vol. 63, no. 3, pp. 1–7, 2015.

7) M. J. R. Heck, J. F. Bauters, M. L. Davenport, **D. T. Spencer**, and J. E. Bowers, "Ultra-low loss waveguide platform and its integration with silicon photonics," *Laser Photon. Rev.*, vol. 20, no. 5, pp. 667–686, Sep. 2014.

8) D. Liang, S. Srinivasan, D.A. Fattal, M. Fiorentino, H. Zhihong, **D.T. Spencer**, J.E. Bowers, and R.G. Beausoleil, "Teardrop Reflector-Assisted Unidirectional Hybrid Silicon Microring Lasers," *Photonics Technology Letters, IEEE* , vol.24, no.22, pp. 1988,1990, Nov. 2012.

9) G. Kurczveil, M.J R. Heck, J.D. Peters, J.M. Garcia, **D. Spencer**, and J.E. Bowers, "An Integrated Hybrid Silicon Multiwavelength AWG Laser," *Selected Topics in Quantum Electronics, IEEE Journal of* , vol. 17, no. 6, pp. 1521-1527, Nov.-Dec. 2011.

10) S. Faralli, K. Nguyen, J. Peters, **D. Spencer**, D. Blumenthal, and J. Bowers, "Integrated hybrid Si/InGaAs 50 Gb/s DQPSK receiver," *Opt. Express*, vol. 20, no. 18, pp. 19726-19734, Aug. 2012.

11) M. Tien, J. Bauters, M. Heck, **D. Spencer**, D. Blumenthal, and J. Bowers, "Ultra-high quality factor planar Si_3N_4 ring resonators on Si substrates," *Opt. Express*, vol. 19, no. 14, pp. 13551-13556, Jul. 2011.

12) D. Liang, M. Fiorentino, T. Okumura, H. Chang, **D. Spencer**, Y. Kuo, A. Fang, D. Dai, R. Beausoleil, and J. Bowers, "Electrically-pumped compact hybrid silicon microring lasers for optical interconnects," *Opt. Express*, vol. 17, no. 22, pp. 20355-20364, Oct. 2009.

13) P. Hari and **D. Spencer**, "Surface morphology of zinc oxide nanorods grown by hydrothermal deposition technique," *Phys. Status Solidi C*, vol. 6: S150–S153, May 2009.

CONFERENCE PUBLICATIONS

1) **D. T. Spencer**, M. Davenport, S. Srinivasan, J. Khurgin, P. A. Morton, and J. E. Bowers, "An Experimental and Theoretical Comparison of Different Narrow Linewidth Bragg Gratings," in *IEEE Photonics Conference 2015*, 2015.

2) **D. T. Spencer** and J. E. Bowers, "Sub-kHz linewidth lasers using integrated Si3N4 Ring Resonators," in *The 76th JSAP Autumn Meeting*, 2015.

3) **D. T. Spencer**, S. Srinivasan, A. Bluestone, D. Guerra, L. Theogarajan, and J. E. Bowers, "A low phase noise dual loop optoelectronic oscillator as a voltage controlled oscillator with phase locked loop," in *2014 IEEE Photonics Conference*, 2014, pp. 412–413.

4) **D. T. Spencer**, M. Heck, R. Moreira, J. T. Bovington, J. E. Bowers, A. Leinse, H. H. van den Vlekkert, R. G. Heideman, M. Hoekman, and T. T. Veenstra, "Integrated single and multi-layer Si_3N_4 platform for ultra-low loss propagation and small bending radii," in *Optical Fiber Communication Conference*, 2014, p. Th1A.2.

5) **D. T. Spencer**, J. F. Bauters, and J. E. Bowers, "Design of Low Loss Directional Couplers for High Q Integrated Resonators," in *Advanced Photonics for Communications*, 2014, p. JT4A.5.

6) **D.T. Spencer**, Y. Tang, J. F. Bauters, M. J. R. Heck, and J. E. Bowers, "Integrated Si_3N_4/SiO_2 ultra high Q ring resonators," *Photonics Conference (IPC), 2012 IEEE*, pp.141-142, 23-27 Sept. 2012.

7) **D.T. Spencer**, D. Dai, Y. Tang, M. J. R. Heck, and J.E. Bowers,, "A uniform, low loss 1×16 power splitter based on a high Q Si_3N_4 ring resonator," *Group IV Photonics (GFP), 2012 IEEE 9th International Conference on* , pp.276-278, 29-31 Aug. 2012.

8) **D. Spencer**, A. Hor, H. Liang, and P. Hari, "Seed layer dependence of ZnO nanorod growth," presented at *APS March Meeting,* 19 Mar. 2010.

9) **D. Spencer**, D. Liang, and J. Bowers, "Hybrid Silicon Microring Lasers," presentation and poster at *NNIN REU Convocation*, 11 Aug. 2009.

10) **D. Spencer**, T. Kawamura, and G. Yusa, "Resistively Detected NMR in InSb," presentation and poster at *Rice Quantum Institute Colloquium,* 08 Aug. 2008.

11) M. Baumer, P. Hari, and **D. Spencer**, "Low temperature growth of ZnO nanorods by chemical bath method," presented at *APS March Meeting*, 12 Mar. 2008.

12) J. E. Bowers, **D. T. Spencer**, M. L. Davenport, and S. Srinivasan, "Integration of Pump Lasers with High Q Si_3N_4 Resonators," presented at *2014 Microresonator Frequency Combs and their Applications (MFCA)*.

13) D. Liang, S. Srinivasan, D.A. Fattal, M. Fiorentino, H. Zhihong, **D.T. Spencer**, J.E. Bowers, and R.G. Beausoleil, "Reflection-assisted unidirectional hybrid silicon microring lasers," *Indium Phosphide and Related Materials (IPRM), 2012 International Conference on* , pp.12-15, 27-30 Aug. 2012.

Abstract

Ultra-Narrow Bandwidth Optical Resonators for Integrated Low Frequency Noise Lasers

by

Daryl T. Spencer

The development of narrowband resonators has far reaching applications in integrated optics. As a precise reference of wavelength, filters can be used in sensors, metrology, nonlinear optics, microwave photonics, and laser stabilization. In this work, we develop record high quality factor (Q) Si_3N_4 waveguide resonators, and utilize them to stabilize a heterogeneously integrated Si/III-V laser.

To increase the Q factor of waveguide resonators, particular attention is given to loss mechanisms. Propagation loss of <0.1 dB/m is demonstrated on the ultra-low loss waveguide platform, a low index contrast, high aspect ratio Si_3N_4 waveguide geometry fabricated with high quality materials and high temperature anneals. Ideality in the directional couplers used for coupling to the resonators is studied and losses are reduced such that 81 million intrinsic Q factor is achieved. Additional results include 1×16 resonant splitters, low κ narrowband gratings, and a dual-layer waveguide technology for low loss and low bend radius in separate regions of the same device layer.

We then combine an ultra-high Q resonator and a heterogeneous Si/III-V laser in a Pound-Drever-Hall (PDH) frequency stabilization system to yield narrow linewidth

characteristics for a stable on-chip laser reference. The high frequency noise filtering is performed with Si resonant mirrors in the laser cavity. A 30 million Q factor Si_3N_4 resonator is used with electrical feedback to reduce close-in noise and frequency walk off. The laser shows high frequency noise levels of 60×10^3 Hz^2/Hz corresponding to 160 kHz linewidth, and the low frequency noise is suppressed 33 dB to 10^3 Hz^2/Hz with the PDH system.

TABLE OF CONTENTS

List of Figures

1   Introduction

1.1   *Photonic Integrated Circuits*

The integration of low loss optical waveguide technology with InP based lasers promises a new generation of devices and systems with high performance operation at lower costs and more portable form factors. By utilizing the best in class performance of different material systems, such as InP for gain, Si for low bend radius waveguides, and Si_3N_4 for low loss routing, higher performance systems can be realized with fewer tradeoffs. The largest application of integrated systems by volume is in the communication field. As aggregate internet bandwidth increases at highly exponential rates, projected to hit 1 ZB (10^{21} Bytes) per year in 2016 [1], interconnects between transmitters and receivers are pushed to higher operating speeds. In long haul (>200 km) and metro optical networks (1-200 km), commercially packaged lasers, modulators, and photodetectors have reached amazing capacities >100 GB/s with >1 TB/s total bandwidth. But future transmission formats using coherent phase and amplitude modulation, such as 16 and 64 QAM, require very stable lasers with linewidths below 100 kHz. As the optical link distance decreases to less than 1 km, massively parallel operations become necessary in point-to-point interconnected data centers, for instance. Additionally, very short electrical based chip-to-chip links are reaching speed limitations due to parasitic capacitances and complex routing [2]. In these chip-to-chip and sub-km regimes, novel photonic integrated circuits (PICs) have the ability to integrate massively parallel devices while leveraging the large scale of CMOS foundry capabilities.

Other exciting applications of PICs are in metrology and microwave photonics. In many ways, the signal-to-noise (S/N) ratio and control requirements for sensors, analog receivers, tunable filters, and precise timing references are much higher than in communications. These

applications present PICs with a unique challenge of reaching high performance at more portable form factors. A critical element in these systems is a low noise, well controlled laser, which we will discuss next. Then we will overview the fabrication technology available, and why we target the platforms of heterogeneous Si/III-V and Si$_3$N$_4$ waveguides.

1.2 Narrow Linewidth Laser Systems

First, we will review the different approaches to achieving low noise lasers. The fundamental generation of spontaneous emission noise in optical gain material results in both amplitude modulation (AM) and frequency modulation (FM) noise on the laser's output. The noise power spectral densities (PSD) are characterized as a function of offset, or Fourier, frequencies from the lasing wavelength of 1550 nm (193 THz). At threshold, the AM noise is suppressed due to clamping of spontaneous and nonradiative emission. The modified Schawlow-Townes linewidth describes these phenomenon in terms of the group velocity (v_g), spontaneous emission rate (n_{sp}), distributed mirror loss rate (α_m) and distributed optical losses of the unpumped cavity (α_{tot}). By modifying this formula with the linewidth enhancement factor, α^2, carrier dependent frequency noise is accounted for as well [3]:

$$\Delta v_{LW} = \frac{v_g^2 h v n_{sp} \alpha_m \alpha_{tot}}{8 \pi P} (1 + \alpha^2) \tag{1.1}$$

The total optical losses can include optical scattering loss, propagation loss, mirror loss, and other non-compensated losses in the gain region such as free carrier absorption.

Thus the first methods to decrease linewidth should be optimizing the gain material, which can be done with, for instance, strained quantum wells [4], and then lower the passive

2

cavity losses. Lowering cavity losses amounts to increasing the "cold cavity" quality factor (Q_{cold}), increasing photon lifetime (τ_{ph}), and decreasing $\alpha_{tot} = \alpha_m + \alpha_i$, related as:

$$Q_{cold} = \omega \tau_{ph} = \frac{\omega}{v_g (\alpha_m + \alpha_i)} \qquad (1.2)$$

A normal Fabry-Perot style laser cavity can be enhanced by obtaining a higher Q resonant cavity for a given length. This has two effects, filtering out higher order modes at the free spectral range (FSR) of the cavity to suppress mode competition noise, and increasing the photon lifetime of the cavity, which is proportional to Q_{cold}. These high Q devices can be Bragg reflectors in DFB or DBR style lasers, or ring resonator reflectors as shown in Figure 1.1.
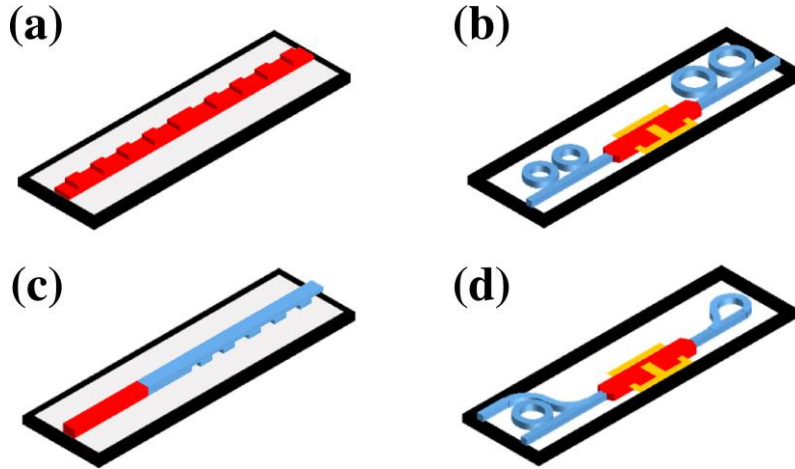
Figure 1.1) General layouts for InP based (a) DFB and (c) DBR style lasers, and heterogeneous Si/III-V (b) CRR and (d) loop mirror style lasers. Gain regions are shown in red, and tunable passive sections in blue.

To incrementally improve the performance further, an external cavity reflection at a certain distance away from the laser cavity can provide further reductions in linewidth. However, the FM noise reduction is now given as a ratio between the external (long) cavity length, L_{ext}, and laser cavity length, L_{cav}:

$$\Delta \nu_{LW} = \Delta \nu_{LW,o} \left(\frac{n_{g,cav} L_{cav}}{n_{g,cav} L_{cav} + n_{g,ext} L_{ext}} \right)^2 \tag{1.3}$$

All of the methods above suppress high frequency FM noise, generally above 10 MHz offset frequencies.

Once the laser cavity has been optimized with higher Q resonant mirrors, there is still the issue of low frequency walkoff and drift. Due to their electrical pumping, thermal sensitivity, and other reasons, flicker noise is written onto the laser's FM noise and increases as the offset frequencies decrease, usually below 1 MHz. Thus the high frequency noise determined by the laser cavity Q has a "white" or Gaussian noise profile, while the low frequency noise increases are termed "colored" or flicker noise. To suppress this unwanted noise, electrical feedback systems utilize optical discriminators, which is basically any device that converts the laser's FM noise to AM noise in an efficient manner. If the conversion is done efficiently on a high slope, then the feedback signal can be used to reduce the laser's detected FM noise within the feedback bandwidth, even reducing it below the white noise level. This not an easy task, since a high slope discriminator naturally has lower optical losses than the laser cavity itself. The discriminator essentially becomes the reference for the laser. The relative slope can be made high with closely integrated Mach-Zehnder interferometers, but utilizing the high slope phase response of a ring resonator can add additional benefits, such as improved conversion efficiency and reduced sensitivity to excess AM noise. In this thesis, we will pursue this ring resonator stabilization scheme, known as Pound-Drever-Hall (PDH) locking.

To achieve long term stability, vibration and thermal drift of the environment becomes an issue at time scales greater than 1 second. In this regime, advanced metrology techniques interrogate atomic references, such as Rb, and offer extremely accurate and stable

wavelength references for a narrow linewidth laser system [5]. However, these atomic references do not have as high of discrimination slope as resonant cavities, and are currently in gaseous form and thus difficult to integrate monolithically [6]. Another exciting development in long term wavelength stability is in integrated optical frequency combs. Using the nonlinear Kerr effect in a high Q and small mode volume Si_3N_4 ring resonator cavity, efficient frequency combs have been generated up to an octave in bandwidth. By frequency doubling the lowest frequency tone at f to 2f and detecting any difference, this signal can be compared to an electrical reference at much lower carrier frequencies. Thus a 10 MHz quartz electronic oscillator with Hz level stability can transfer this stability to the optical domain. Any laser locked to this frequency comb reference will benefit from the electronic oscillator stability, while generating an optical output of 193 THz with Hz level control, over 10^{-14} in frequency stability.

1.3   Material Platforms for PICs

The need for integration of various fiber-optic systems is driven by a variety of applications we have already mentioned. For low noise on-chip laser systems, the main photonic platforms are based on InP, silicon-on-insulator (SOI), and low index cores with silica claddings, each with their own tradeoffs that we will outline.

InP has inherent advantages in terms of active devices, such as lasers, detectors, and electroabsorption modulators, due to their direct bandgap in the wavelength range of 1250 nm – 1600 nm. This wavelength range is utilized heavily in long-haul communications due to the low propagation loss of optical fiber in this region. Active region regrowth technology allows high efficiency phase tuners and strong reflection grating structures to be monolithically integrated with gain regions, producing compact, robust active devices.

However, the propagation loss of the passive waveguides is generally a few dB/cm, limiting their use as very high Q discriminators and filters.

SOI has emerged as a high-volume, low-cost photonic platform due to its compatibility with very mature electronic CMOS foundries. The SOI platform gains active functionality with Ge growth, which has enabled efficient waveguide photodetectors and has recently demonstrated electrically pumped lasers, though these are currently troublesome to develop and reproduce [7]. The high index of Si near 3.5 allows for tight bends of a few μm and thus very compact devices, but sidewall roughness due to such a highly confined waveguide core creates scattering losses. This yields propagation losses of 27 dB/m at 300 μm bend radius [8] and 2.7 dB/m at 2.45 mm bend radius [9], in which the latter is a shallow ridge waveguide that emulates a low confinement, large area mode as seen in the silica platforms.

To reach the lowest propagation loss, it is necessary to move to lower refractive index contrast waveguides. Amorphous SiO_2, or silica, offers a highly transparent cladding material in the infrared that can be deposited and annealed in typical cleanroom facilities. The waveguide core of Ge-doped silica, silicon oxynitride (SiO_xN_y), or Si_3N_4 has a slightly higher index than the cladding ($\Delta n \approx 0.05 - 0.5$), and propagation losses can be <0.1 dB/m at >10 mm bend radius. A comparison of the planar waveguide platforms is shown in Figure 1.2. In this thesis, we develop Si_3N_4 waveguides for resonant devices, using what we will term ultra-low loss waveguides (ULLW).
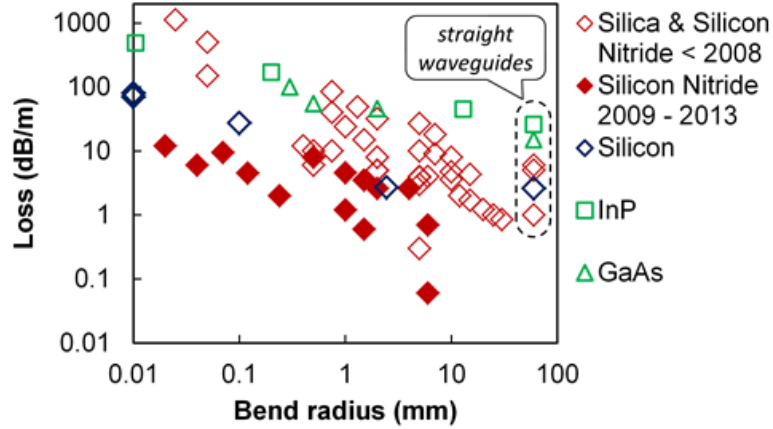
Figure 1.2) Propagation loss comparison of various platforms versus bend radius. UCSB Si₃N₄ results are shown in solid red diamonds. From [10] © 2014 Wiley.

An important figure of merit to achieve narrow bandwidth filters and lasers is the optical quality factor (Q factor). To give a brief introduction, the largest improvement in Q factor can be made by decreasing the propagation loss and any excess losses, which increases the "intrinsic" Q factor (Q_{int}). Q_{int} is the limitation of a given isolated resonator, as it does not have any variable "loading" due to output mirrors or coupling schemes ($Q_{coupling}$). Once coupled, we can then experimentally measure a total loaded Q factor (Q_{load}). These two terms have a relationship similar to parallel impedances due to the extraction of energy away from the resonator:

$$\frac{1}{Q_{load}} = \frac{1}{Q_{int}} + \frac{1}{Q_{coupling}}$$ (1.4)

For the purposes of this work, we use the frequency domain definition of Q most applicable to experiments, which is related to the measured FWHM (Δv) and carrier frequency (v):

$$Q_{load} = \frac{\Delta v}{v}$$ (1.5)

By numerically fitting the lineshape of the filter, you can extract the contribution of the propagation plus excess losses, or Q_{int}. In Figure 1.3 we overview the state of the art in integrated resonators. We choose to highlight waveguide coupled schemes due to their

7

planar nature and ability to be integrated in PICs, though much work is being pursued in the

whispering gallery mode resonator field [11], [12]. The work of this thesis is highlighted in

red triangles, and Chapter 3 will outline the progression to achieve the record high Q_{int} of

81 million using the ULLW platform.
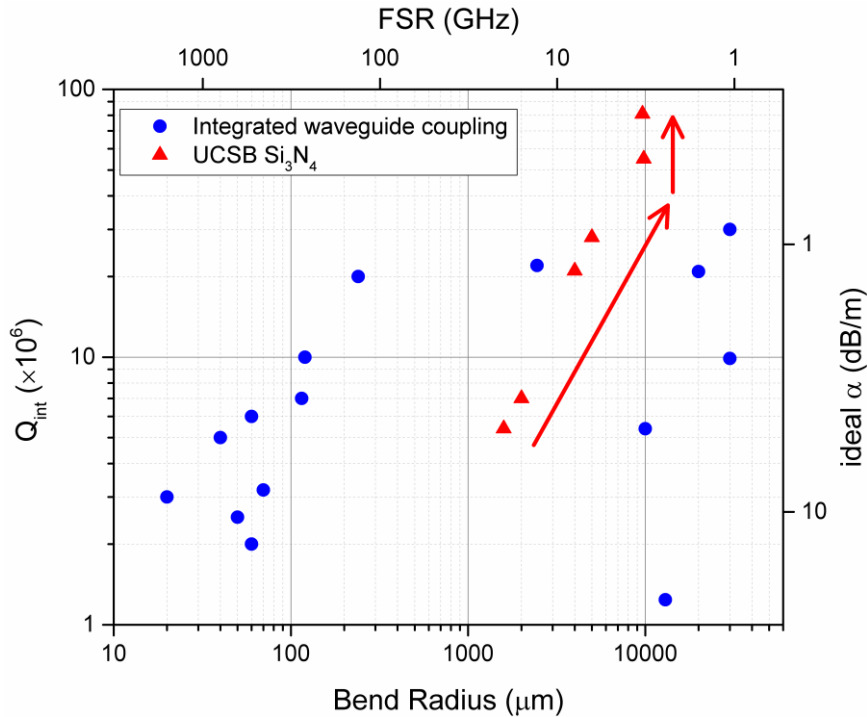
Figure 1.3) State of the art comparison of Q_{int} vs. bend radius for integrated waveguide coupled resonators [9], [13]–[21]. The propagation loss (α) and free spectral range (FSR) are scaled assuming λ=1550 nm, n_{eff}=n_g=1.5, and ideal directional couplers. UCSB Si_3N_4 results[13], [14], [22] are highlighted in red triangles. From [22] © 2014 OSA.

1.4   Heterogeneous Integration of Platforms

We are now interested in obtaining integration[1] of multiple material platforms to obtain

the best performance in active devices and passive narrowband filters for discriminators. In

addition to improvements in performance, weight, and costs, overall system performance can

also be greatly improved by avoiding chip to chip coupling loss, which is normally done

---

[1] The monolithic integration of platforms is referred to as "heterogeneous", as opposed to "hybrid" integration, which uses pick and place packaging techniques to assemble systems.

with ball or lensed fibers and has optical losses > 6 dB/facet. Especially when working with any detection system, this reduction in optical loss is critical as the electrical loss is twice the optical dB loss assuming square law photodetectors.

The heterogeneous Si//III-V platform is an intimate integration of Si waveguides and InP quantum well gain material pioneered at UCSB. By utilizing wafer bonding techniques, broad areas ($\approx$1×1 cm) of quantum well P-I-N diodes are monolithically integrated on top of lithographically patterned Si waveguides. The gain material is then processed in the same fabrication flow with lithographic alignment of the laser "mesa" to the Si waveguides. Tapers in the III-V layers convert the mode shape adiabatically between the hybridized Si//III-V waveguide (partial confinement in Si and III-V) and the input/output Si waveguide. Further details of importance will be provided in the experimental sections; for a review of the platform the reader is referred to [23]. A schematic of the ULLW platform and heterogeneous Si/III-V platform is shown in Figure 1.4a-b.
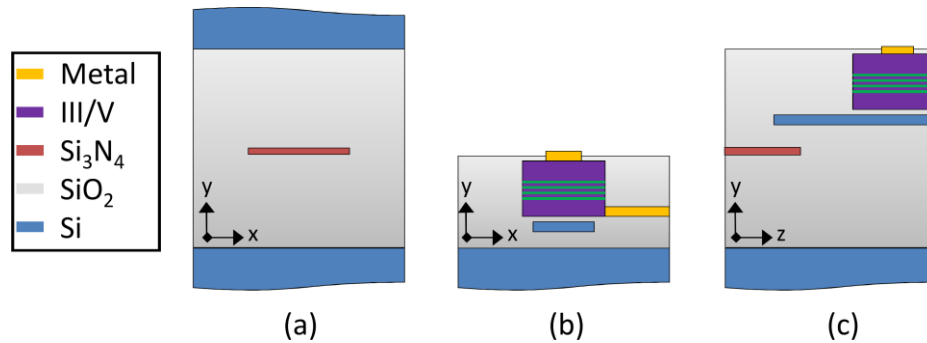
Figure 1.4) General layouts of the (a) ULLW, (b) heterogeneous Si/III-V, and (c) integrated SOUL platform. (a)-(b) are shown as cross sections, and (c) is a lateral view to show coupling between the layers (tapers not drawn).

The integration of material platforms to achieve superior passive performance has been of much interest recently. A few groups have implemented multiple material platforms in a backend process, whereby the low propagation loss layer is added after the temperature sensitive devices are fabricated. NTT has developed a silica on Ge-Si platform that has

9

achieved 0.9 dB/cm by carefully controlling the SiO_x material deposition. The use of Ge also allowed for photodetection out to a 20 GHz bandwidth. Georgia Tech. has developed a series of Si_3N_4 resonators on top of Si waveguides used for vertical coupling. After utilizing high temperature anneals, 20 million Q factor was achieved [15]. Finally, UCSB has been developing a front-end process whereby the ULLWs are fabricated and annealed before a multi-step wafer bonding of SOI and InP gain materials, as shown in Figure 1.4c. We have thus far demonstrated Si_3N_4 based AWG filters and InGaAs/InP detectors monolithically integrated [24], and hope to add lasers soon to complete the platform for use in a wide array of PICs.

1.5   *Overview of Thesis*

Chapter 2 will overview the ULLW platform, fabrication, and its main propagation loss results. The waveguide geometries utilized for the resonators fabricated in this thesis will be highlighted. Then, we will go through the derivations, spectra, and figures of merits for ring resonators.

Chapter 3 will outline our route to record high Q waveguide coupled resonators. We will present our learnings of the ULLW platform and how directional couplers play an important role in the overall loss of the device. Single and multimode resonators will be presented at different waveguide geometries to achieve the best result of 81 million Q factor.

Chapter 4 will describe two novel waveguide results. The first is a 1×16 resonant power splitter that shows excellent loss and uniformity compared to other high port count splitters. The second result is a new dual-layer Si_3N_4 technology to achieve low propagation loss and small bend radius. Two geometries are fabricated simultaneously at the wafer level with low

loss tapers for transition regions. Cascaded resonant devices will be shown to describe the functionality, and propagation loss numbers will be presented.

Chapter 5 will describe grating theory and how the ULLW platform can be used to produce single frequency, narrow bandwidth devices. Sampled, high order, and uniform Bragg gratings will be presented with good control of the perturbation. Additionally, quarter-wave shifted gratings are used to show Q factors of 204 thousand.

Chapter 6 will bring together an ULLW resonator and a heterogeneous Si/III-V laser to reduce the FM noise of the laser. The highly sensitive RF locking PDH scheme will be introduced and the important system metrics will be described. Finally, the FM noise characteristics will be measured and shown to be reduced to kHz linewidth noise levels.

Chapter 7 will conclude the thesis with a summary and overview of future work, including microwave photonics applications and the integration of material platforms.

1.6   References

[1]   Cisco, "The Zettabyte Era: Trends and Analysis," 2015.
[2]   D. Miller, "Device Requirements for Optical Interconnects to Silicon Chips," *Proc. IEEE*, vol. 97, no. 7, pp. 1166–1185, Jul. 2009.
[3]   K. Vahala, *Optical Microcavities*. Singapore: World Scientific, 2004.
[4]   M. Okai, M. Suzuki, T. Taniwatari, and N. Chinone, "Corrugation-pitch-modulated distributed feedback lasers with ultranarrow spectral linewidth," *Jpn. J. Appl. Phys.*, vol. 33, no. 5A, pp. 2563–2570, May 1994.
[5]   M. A. Lombardi, "The Evolution of Time Measurement, Part 3: Atomic Clocks," *Instrum. Meas. Mag.*, pp. 46–49, 2011.
[6]   J. Kitching, S. Knappe, L.-A. Liew, P. D. D. Schwindt, V. Gerginov, V. Shah, J. Moreland, A. Brannon, Z. Popovic, J. Breitbarth, and L. Hollberg, "Chip-Scale Atomic Frequency References," in *ION GNSS 18th International Technical Meeting of the Satellite Division*, 2005, no. September, pp. 1662–1669.
[7]   Z. Zhou, B. Yin, and J. Michel, "On-chip light sources for silicon photonics," *Light Sci. Appl.*, vol. 4, no. 358, Nov. 2015.
[8]   P. Dong, W. Qian, S. Liao, H. Liang, C.-C. Kung, N.-N. Feng, R. Shafiiha, J. Fong, D. Feng, A. V Krishnamoorthy, and M. Asghari, "Low loss shallow-ridge silicon waveguides.," *Opt. Express*, vol. 18, no. 14, pp. 14474–9, Jul. 2010.
[9]   A. Biberman, M. J. Shaw, E. Timurdogan, J. B. Wright, and M. R. Watts, "Ultralow-loss silicon ring resonators," *Opt. Lett.*, vol. 37, no. 20, pp. 4236–4238, Oct. 2012.

[10] M. J. R. Heck, J. F. Bauters, M. L. Davenport, D. T. Spencer, and J. E. Bowers, "Ultra-low loss waveguide platform and its integration with silicon photonics," *Laser Photon. Rev.*, vol. 8, no. 5, pp. 667–686, Sep. 2014.

[11] X. Zhang and A. M. Armani, "Silica microtoroid resonator sensor with monolithically integrated waveguides.," *Opt. Express*, vol. 21, no. 20, pp. 23592–603, Oct. 2013.

[12] H. Lee, T. Chen, J. Li, K. Y. Yang, S. Jeon, O. Painter, and K. J. Vahala, "Chemically etched ultrahigh-Q wedge-resonator on a silicon chip," *Nat. Photonics*, vol. 6, no. 6, pp. 369–373, May 2012.

[13] D. T. Spencer, Y. Tang, J. F. Bauters, M. J. R. Heck, and J. E. Bowers, "Integrated Si_3N_4 /SiO_2 ultra high Q ring resonators," in *IEEE Photonics Conference 2012*, 2012, pp. 141–142.

[14] M.-C. Tien, J. F. Bauters, M. J. R. Heck, D. T. Spencer, D. J. Blumenthal, and J. E. Bowers, "Ultra-high quality factor planar Si_3N_4 ring resonators on Si substrates.," *Opt. Express*, vol. 19, no. 14, pp. 13551–13556, Jul. 2011.

[15] Q. Li, A. A. Eftekhar, M. Sodagar, Z. Xia, A. H. Atabaki, and A. Adibi, "Vertical integration of high-Q silicon nitride microresonators into silicon-on-insulator platform," *Opt. Express*, vol. 21, no. 15, pp. 18236–18248, Jul. 2013.

[16] R. Adar, Y. Shani, and C. Henry, "Measurement of very low- • loss silica on silicon waveguides with a ring resonator," *Appl. Phys. Lett.*, vol. 58, no. 5, pp. 444–445, 1991.

[17] R. Adar, M. R. Serbin, and V. Mizrahi, "Less than 1 dB per meter propagation loss of silica waveguides measured using a ring resonator," *J. Light. Technol.*, vol. 12, no. 8, pp. 1369–1372, 1994.

[18] A. Gondarenko, J. S. Levy, and M. Lipson, "High confinement micron-scale silicon nitride high Q ring resonator," *Opt. Express*, vol. 17, no. 14, pp. 11366–11370, Jul. 2009.

[19] K. Luke, A. Dutt, C. B. Poitras, and M. Lipson, "Overcoming Si_3N_4 film stress limitations for high quality factor ring resonators," *Opt. Express*, vol. 21, no. 19, pp. 22829–22833, Sep. 2013.

[20] L. Zhuang, D. Marpaung, M. Burla, W. Beeker, A. Leinse, and C. Roeloffzen, "Low-loss, high-index-contrast Si_3N_4 /SiO_2 optical waveguides for optical delay lines in microwave photonics signal processing.," *Opt. Express*, vol. 19, no. 23, pp. 23162–23170, Nov. 2011.

[21] C. Ciminelli, F. Dell'Olio, M. N. Armenise, F. M. Soares, and W. Passenberg, "High performance InP ring resonator for new generation monolithically integrated optical gyroscopes," *Opt. Express*, vol. 21, no. 1, pp. 556–564, Jan. 2013.

[22] D. T. Spencer, J. F. Bauters, M. J. R. Heck, and J. E. Bowers, "Integrated waveguide coupled Si_3N_4 resonators in the ultrahigh-Q regime," *Optica*, vol. 1, no. 3, pp. 153–157, Sep. 2014.

[23] M. Heck, J. Bauters, M. Davenport, and J. Doylend, "Hybrid silicon photonic integrated circuit technology," *IEEE J. Sel. Top. Quantum Electron.*, vol. 19, no. 4, 2013.

[24] M. Piels, J. F. Bauters, M. L. Davenport, M. J. R. Heck, and J. E. Bowers, "Low-Loss Silicon Nitride AWG Demultiplexer Heterogeneously Integrated With Hybrid III–V/Silicon Photodetectors," *J. Light. Technol.*, vol. 32, no. 4, pp. 817–823, Feb. 2014.

2 ULLW Platform and Application to Resonant Structures

2.1 The ULLW Platform

2.1.1 Introduction

The material qualities and deposition methods of silica thin films make them ideal for use in a low loss waveguide platform. The early development of high quality planar waveguides involved a very low index contrast core surrounded by the silica cladding, $\Delta n < 1\%$, using Ge or Ph-doped SiO_2 as the core. With a low Δn, the confinement in the core needed to be >70% to achieve practical mm-level bend radii. In [1], 0.85 dB/m propagation loss is achieved with a Ph-doped silica ring resonator at 30 mm bend radius, yielding Q_{int}=30 million. Ge-doped cores from NTT yielded 5 mm bend radius waveguides with 0.3 dB/m propagation loss and low polarization dependence [2]. Due to the higher confinement, the core material quality is critical for low loss and high temperature anneals (>1000°C) were used to drive out impurities.

Using Si_3N_4, which has a higher $\Delta n \approx 50\%$, a high aspect ratio waveguide geometry allows for a large area mode that has low confinement, i.e. more dependent on the cladding material quality instead of the core. In this way, control of the thin film deposition and lithographic definition of the waveguide width define the allowed modes. The low confinement of $\approx$3% in the Si_3N_4 ULLW platform means that annealing a high quality silica cladding will produce a large loss reduction, and any roughness due to etching of the sidewalls will have a smaller effect on the propagation loss.

2.1.2 Fabrication

The ULLW fabrication begins with high quality Si_3N_4 deposited via low pressure chemical vapor deposition (LPCVD) on a 15-µm thick thermally grown SiO_2 layer on a silicon substrate at the Lionix foundry. For our work, a thin 40-100 nm film is chosen to lower the confinement factor and the exact thickness is chosen based on the application's bend radius requirement. Contact lithography on 4" wafers defines waveguide devices. 3.1 µm of SiO_2 is deposited via tetraethylorthosilicate (TEOS)-based LPCVD in three layers, with an 1150°C anneal after each layer. The sample is then chemically mechanically polished and shipped to our university for cladding deposition. For the lowest loss structures, a 15-µm thick thermal SiO_2 on Si top cladding is wafer bonded after plasma activation of the surfaces. The samples are annealed at 950°C for 3 hours and diced for testing. The completed cross section is shown in Figure 2.1a-b, and further fabrication details can be found in[3], [4]. Depending on the Si_3N_4 thickness used, we term this layout "40 nm bonded cladding" throughout the thesis.

Title	40 (45) nm bonded	90 (100) nm bonded	90 nm sputter
width	7 (11) μm	2.8 μm	2.8 μm
Γ_{core}	2.90%	12.6%	13.3%
A_{eff}	24 μm^2	4.9 μm^2	4.4 μm^2
n_{eff}	1.449	1.467	1.465
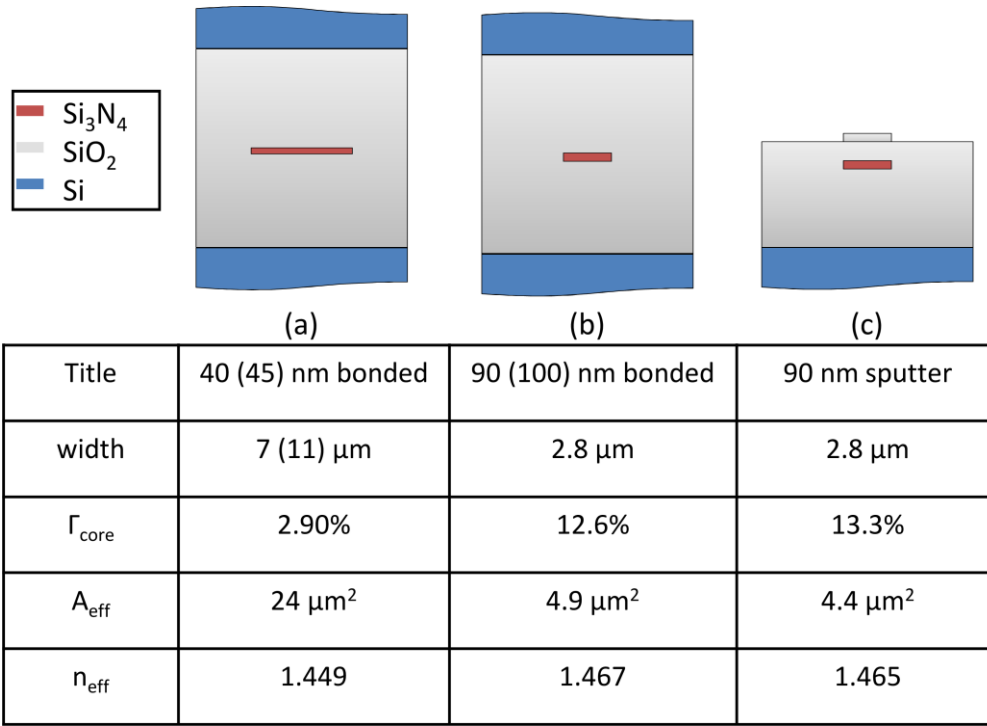
Figure 2.1) General layouts of the ULLWs used in this thesis. (a) 40-45 nm bonded cladding, (b) 90-100 bonded cladding, and (c) 90 nm sputtered cladding. Simulated numbers are for dimensions listed outside of parentheses.

We also utilize the in-house cleanroom facilities of UCSB to develop a sputtered top cladding that is compatible with integration of Si waveguides and thermal tuners on the SOUL platform. In this process flow, termed "90 nm sputtered cladding" layout, we use improved 248 nm DUV lithography, a 150°C thermal reflow to reduce line edge roughness, and $CF_4/CHF_3/O_2$ inductively coupled plasma etching of 90 nm core waveguides. The single CMOS compatible lithography step is done over areas ≈22×24 mm, suitable for 1 mm bend radii structures. Removal of the photoresist is achieved with a combination of oxygen plasma ashing and photoresist stripper. The Si_3N_4 is then stripped of organic contaminants in 6:1:1 $H_2O:H_2O_2:NH_4OH$. Following cleaning, the wafer is annealed at 1050°C in a tube furnace for seven hours to drive off residual hydrogen. The upper cladding of the waveguide consists of 1.3 μm SiO_2 deposited by reactive ion sputtering. A brief *in-situ* argon plasma clean is performed immediately before the deposition to ensure that the surface of the Si_3N_4

15

is completely clean. The sputtered film is then annealed in a rapid thermal annealer at 800°C for 1 minute to reduce absorption. The completed wafers are separated into devices by a dicing saw and edge-polished to form facets for characterization. This third variant of the ULLW platform is show in Figure 2.1c, and will be used for the grating based devices presented in the next chapter.

2.2   ULLW Performance

Next, we will highlight the record low propagation losses that have been achieved in the past few years using the ULLW platform [5]. While not the highlight of the thesis, it is necessary to review the results as the resonant structures in this thesis utilize the ULLWs.

To characterize the propagation loss of the ULLW platform, Archimedean spiral delay lines are implemented on the 40 nm bonded cladding structures. To characterize the waveguide properties, we use a coherent optical backscatter reflectometer (OBR), the Luna OBR 4400. This instrument uses a tunable laser with calibrated wavelength sweep to measure the backscatter of the waveguide (B) versus length (z). Figure 2.2a shows the OBR schematic, which uses an MZI structure with a circulator in one arm to probe the device under test (DUT). Two waveguide spiral structures are used to characterize the platform. The first variation is the s-bend spiral structure, which spirals into an inner s-bend at a minimum bend radius that will not affect the propagation loss. If designed properly, the backscatter from facet to facet is exponentially decaying at twice the propagation loss constant, thus the propagation loss is extracted as twice the slope of the backscatter in dB:

$$B_{dB}(z) = 2*\alpha_{dB/m}*z + B_{offset} \tag{2.1}$$

The second test structure is the spiral-in structure which intentionally spirals to a tight bend radius to extract the bend loss versus bend radius. In this test structure, the propagation

16

loss now has an exponential dependence versus bend radius (r), and can be used in conjunction with the layout geometry (bend radius versus length) and the previous equation:

$$\alpha_{dB/m} \propto e^{c_1 * r(z)} \tag{2.2}$$

Examples of both of these structures are shown in Figure 2.2a, with red light propagating through the entire delay line. The backscatter results are shown in Figure 2.2b, and the fits are highlighted in aqua.
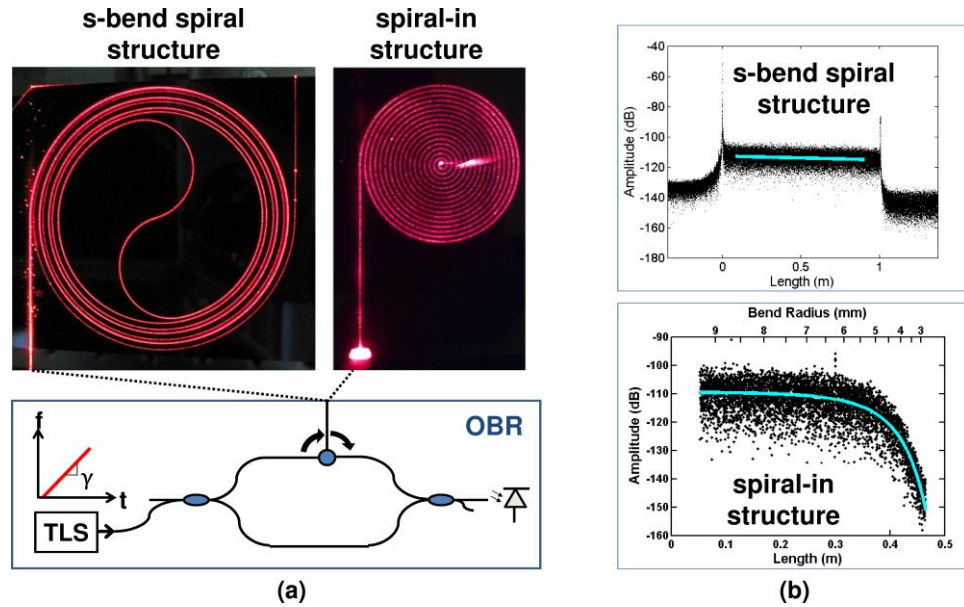
Figure 2.2) (a) Measurement schematic of spiral delay lines using Optical Backscatter Reflectometry (OBR), and top down view of red LED light propagating through the test structures. (b) Resulting backscatter signal versus length to extract propagation loss and bend loss [6]. © 2014 Wiley.

Additionally, the wavelength swept properties of the OBR measurement allow us to extract spectral properties of the waveguides. By filtering the backscatter data versus wavelength and fitting for propagation loss, we achieve the loss spectra. Figure 2.3 shows the loss spectra between 1540-1580 nm, and has multiple Gaussian features. These peaks are due to various hydrogen infrared absorption overtones, mostly due to Si-H and N-H bonds formed during fabrication. Using the high temperature anneals of the ULLW process reduces these absorption peaks to levels where the scattering loss becomes a limitation. The

17

scattering loss is due to the overlap of the waveguide mode with the sidewall roughness due to etching. By varying the waveguide width, we find a minimum propagation loss of 0.045 ± 0.04 dB/m for 40 nm×13 μm geometry. While this width does support three TE modes, they were excited with an adiabatic single mode taper for loss characterization. For the resonant devices presented in the next chapter, we will study both the single mode and multimode regimes of the ULLWs. Support of multiple modes creates challenges in mode excitation, with the tradeoff of lower scattering loss and thus total propagation loss.
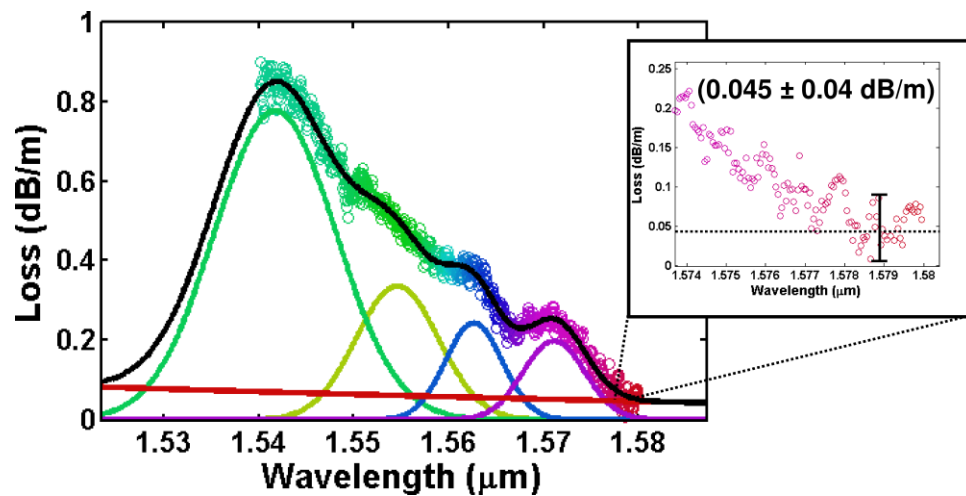
Figure 2.3) Propagation loss versus wavelength extracted from OBR measurements of the 40 nm bonded cladding waveguides. The inset highlights the record low loss of 0.045 ± 0.04 dB/m at 1579 nm. From [6] © 2014 Wiley.

Another unique quality of the ULLW platform is the polarization dependence. With such a high aspect ratio geometry, there is a naturally high birefringence to the platform. This bodes well for devices such as polarizers, as the TM mode can be filtered out through simple s-bends. The lower TM confinement causes the mode to leak out, and has been shown to yield over 75 dB of polarization extinction ratio for the 40 nm bonded cladding layout [7]. This is critical for resonant applications as we will prefer a single mode and easy excitation in experiments.

2.3   Theory of Ring Resonators

Resonant devices will benefit greatly from the record low planar waveguide loss of the ULLW platform. In this section, we will overview the theory of ring resonators and how low propagation loss plays a role in their spectral properties.

2.3.1   Q Factor and Other Figures of Merits

The basic traveling wave ring resonator has a circular geometry creating an infinite impulse response system. Resonances occur at $n_{eff}L = N\lambda$, where n_{eff} is the effective index of the mode, L is the cavity length, N is the mode number, and λ is the wavelength. For resonators in the infrared, the typical mode number is in the thousands, and thus has many closely spaced resonances. As shown in Figure 2.4, the "isolated" ring has Q_{int} which is then combined with directional coupler(s), Q_c, and any excess losses from mode mismatch or extra scattering in the coupling region(s), Q_{excess}, in a manner similar to parallel impedances. The main feedback loop has 1 or more directional coupler ports as the input/output which decrease the overall Q_{load}.

(a) Isolated   (b) Single Bus   (c) Add-Drop

$$\frac{1}{Q_{load}} = \frac{1}{Q_{int}}$$

$$\frac{1}{Q_{load}} = \frac{1}{Q_{int}} + \frac{1}{Q_{c1}} + \frac{1}{Q_{excess}}$$

$$\frac{1}{Q_{load}} = \frac{1}{Q_{int}} + \frac{1}{Q_{c1}} + \frac{1}{Q_{c2}} + \frac{1}{Q_{excess}}$$
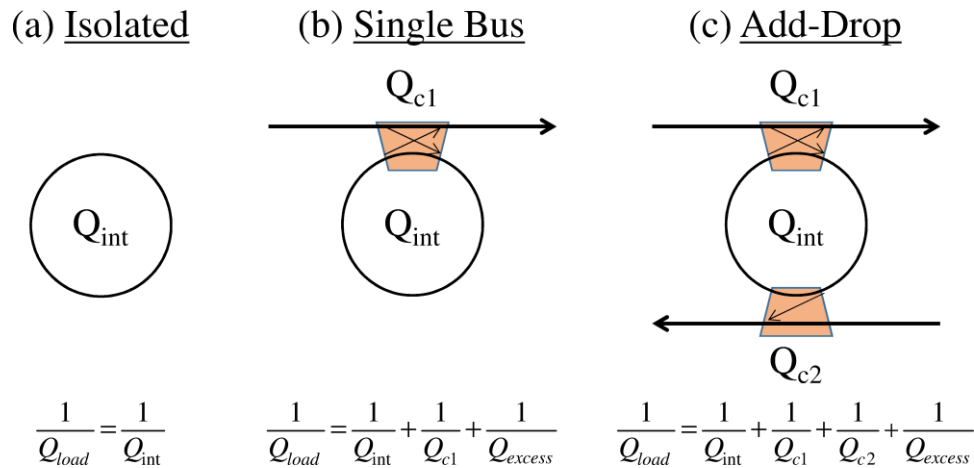
Figure 2.4) Schematics of (a) isolated, (b) single bus, and (c) add-drop ring resonators and their respective loaded Q factor relationships.

The Q factor of a resonant system can be interpreted in multiple domains [8]. The physical definition of Q factor is the rate of optical energy decay that is stored in the resonator, and is very useful at it directly relates Q_{int} to the intensity propagation loss constant α. For a low round trip loss resonator:

$$Q_{int} = \omega \frac{Stored\ Energy}{Power\ Loss} = \frac{2\pi n_{eff}}{\alpha_{Np/m}\lambda} = 10*\log_{10}(e)\frac{2\pi n_{eff}}{\alpha_{dB/m}\lambda} \qquad (2.3)$$

where ω is the optical angular frequency in rad/s. This relationship to α is critical in understanding the fundamental limits of most resonators, and Figure 2.5 shows how a waveguide platform's propagation loss limits the Q_{int} of a system. For 0.1 dB/m propagation loss, the maximum Q value is 250 million. Notice that the Q factor cannot be made larger by simply extending the cavity length.
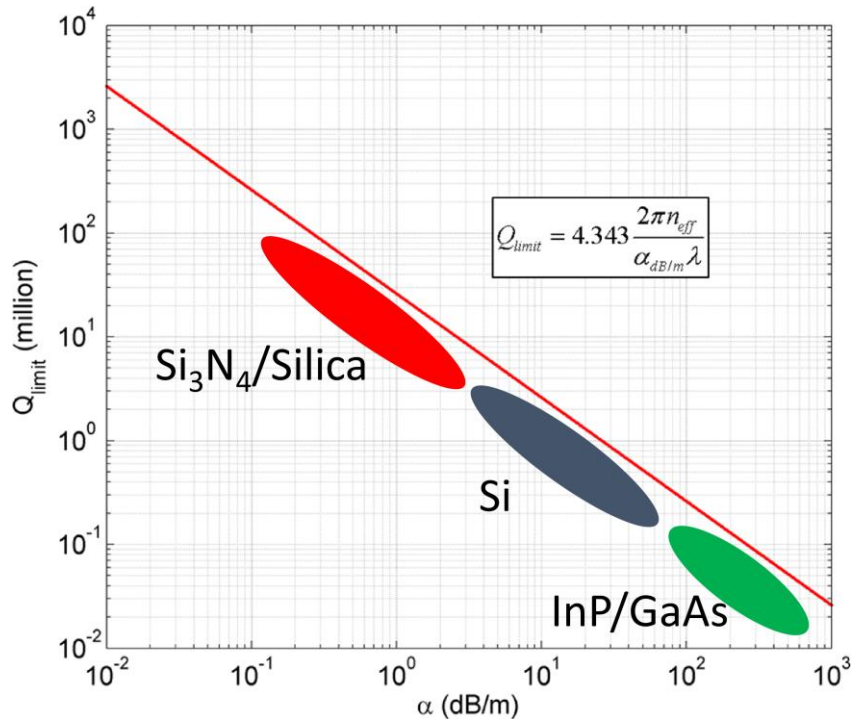
Figure 2.5) The limit of Q factor for a given propagation loss

A time domain picture of Q relates the photon lifetime (τ_{ph}), or 1/e decay rate of optical intensity in the cavity, to one optical cycle as:

$$Q = \omega \tau_{ph} \qquad (2.4)$$

In the time domain, any energy stored in the cavity has an exponential "ringdown" time with a constant of τ_{ph}. One way to measure the Q_{load} of the system is to input light at the resonance wavelength and quickly turn off the light to observe the cavity decay and derive the ringdown time [9]. The final representation of Q is in the frequency domain, where Q_{load} is simply related to λ and the experimentally measured FWHM ($\Delta\lambda_{3dB}$):

$$Q_{load} = \frac{\lambda}{\Delta\lambda_{3dB}} \qquad (2.5)$$

A few important features are worth pointing out in the spectra, including the free spectral range (FSR) and finesse (F) given as:

$$FSR = \frac{c}{n_g L} = \frac{\lambda^2}{n_g L} \qquad (2.6)$$

$$Finesse = \frac{FSR}{FWHM} = \frac{c}{n_g L \Delta v} \qquad (2.7)$$

As an example of the regime we'll be working in, for a 40 nm bonded Si_3N_4 ring with 9.8 mm radius and α=0.25 dB/m, the Q_{int} is 100 million, Q_{load} is 50 million, FSR is 3.3 GHz and finesse is 860. Adding just 0.05 dB of insertion loss decreases the Q_{load} to 20 million, and finesse to 330.

2.3.2   Spectrum Derivation

The spectral transfer function of resonators can be found in numerous ways, via equivalent RLC circuits, algebraic manipulation of infinite series, or feedback theory. We will begin with a simple model of a directional coupler. We define the amplitude cross coupling coefficient, κ_c, bar (non-coupled) coefficient, t, and overall power insertion loss of

the coupler, γ (γ=1 for lossless). For a given directional coupler geometry, κ_c^2 is usually determined analytically using coupled mode theory or numerically with simulations [10]. With the aid of Figure 2.6, the 4 port relation for a reciprocal coupler with excess loss is given as:

$$\begin{pmatrix} a_t \\ b_2 \end{pmatrix} = \begin{pmatrix} t & -j\kappa_c \\ -j\kappa_c & t \end{pmatrix} \begin{pmatrix} a_i \\ b_1 \end{pmatrix} \tag{2.8}$$

Such that the total power is conserved between the cross, bar, and insertion loss:

$$t^2 + k_c^2 = \gamma \leq 1 \tag{2.9}$$

And the round trip constant, ξ, is dependent on the round trip phase and amplitude propagation loss:

$$\xi = e^{-\left(j\frac{2\pi n_{eff} L}{\lambda}\right)} e^{-\left(\frac{\alpha_{Np/m} L}{2}\right)} \tag{2.10}$$
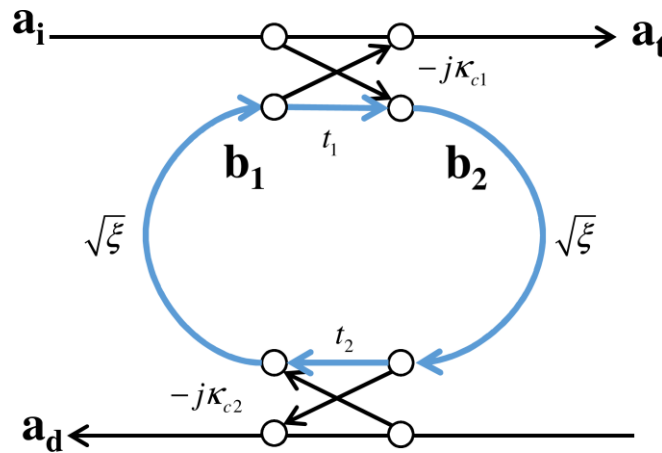
Figure 2.6) Schematic of ring resonator with nodes and paths labeled for analysis.

We will show the feedback theory method known as Mason's Rule, as it is applicable to many different devices and systems without much recalculation. To calculate the system, we find all k forward paths from beginning to end without repeating a node, labeled T_k. Then we

22

calculate the determinate by finding all feedback loops subtracted from 1, labeled Δ^2. Any feedback loop that shares a node with a forward path will be subtracted in the calculation of Δ to yield Δ_k. Then the transfer function is summed over each $T_k * \Delta_k$ product and divided by the determinate:

$$TF = \frac{\sum_k T_k \Delta_k}{\Delta} \tag{2.11}$$

For the add-drop ring from a_i to a_d, the drop port constants are:

$$
\begin{aligned}
T_1 &= (-jk_{c1})(-jk_{c2})\sqrt{\xi} \\
\Delta &= 1 - (\xi t_1 t_2) \\
\Delta_1 &= 1
\end{aligned} \tag{2.12}
$$

and finally:

$$T_{drop} = \frac{a_d}{a_i} = \frac{-k_{c1}k_{c2}\sqrt{\xi}}{1-(\xi t_1 t_2)} \tag{2.13}$$

For the add-drop ring from a_t to a_d, the through port constants are:

$$
\begin{aligned}
T_1 &= t_1 \\
T_2 &= (-jk_{c1})^2 \xi t_2 \\
\Delta &= 1 - (\xi t_1 t_2) \\
\Delta_1 &= \Delta \\
\Delta_2 &= 1
\end{aligned} \tag{2.14}
$$

and finally:

$$T_{through2} = \frac{a_t}{a_i} = t_1 - \frac{k_{c1}^2 \xi t_2}{1-(\xi t_1 t_2)} = \frac{t_1 - \gamma \xi t_2}{1-(\xi t_1 t_2)} \tag{2.15}$$

---

[2] Systems with multiple feedback loops require a different calculation of the determinate, but the resonators presented here don't require this.

23

For a single directional coupler, we simply ignore terms with t_2 and κ_{c2}, yielding the through port response of single bus ring:

$$T_{through1} = \frac{a_t}{a_i} = t_1 - \frac{k_{c1}^2 \xi}{1-(\xi t_1)} = \frac{t_1 - \gamma \xi}{1-(\xi t_1)} \qquad (2.16)$$
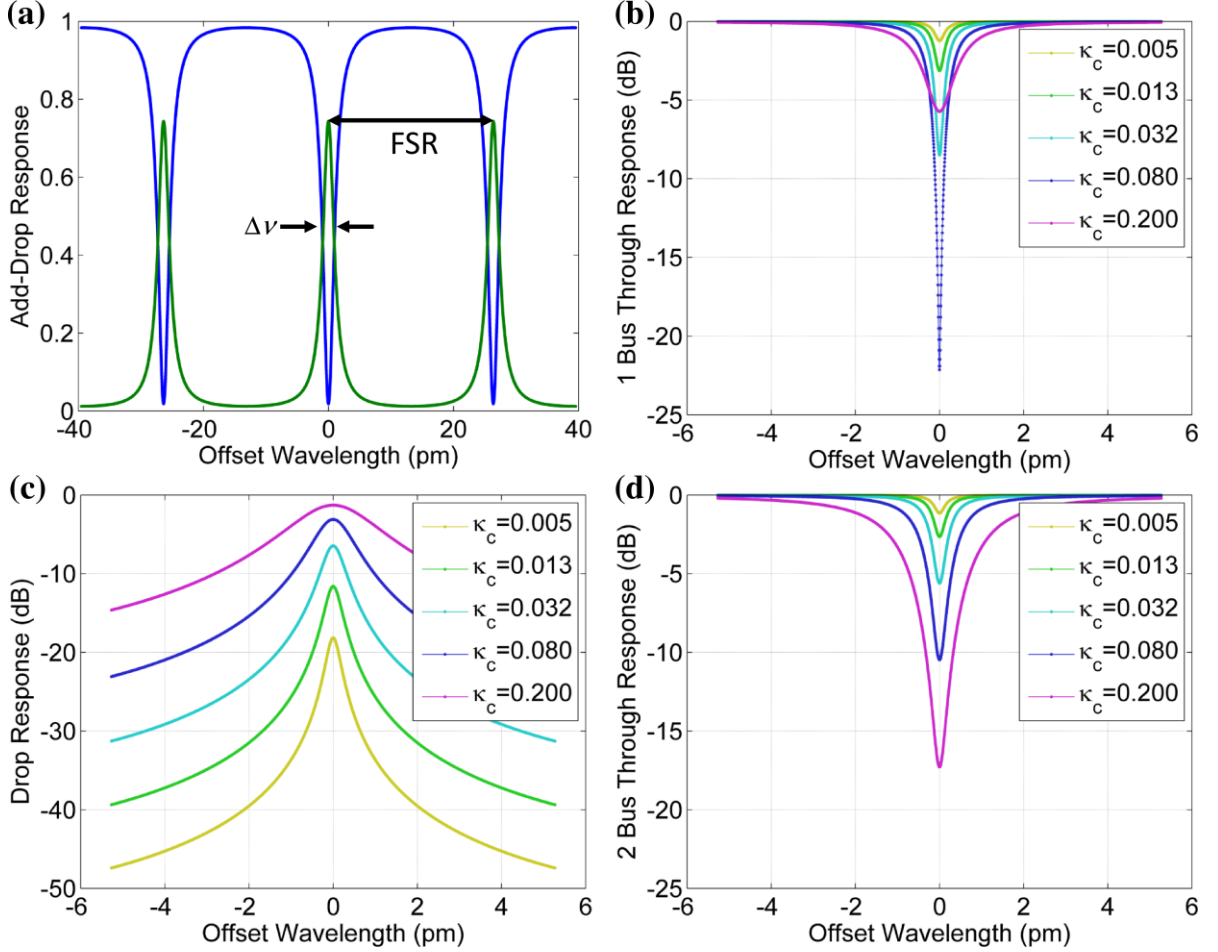
Figure 2.7) Ring resonator spectra at 1550 nm for R= 9.8 mm, α=5 dB/m, n=1.48. (a) Add-drop spectra highlighting the FSR and FWHM, and varying κ_c for (b) single bus ring, (c) drop port of 2 bus ring ($\kappa_{c1} = \kappa_{c2}$), and (c) through port of 2 bus ring ($\kappa_{c1} = \kappa_{c2}$).

An example of the spectra is presented in Figure 2.7, where we highlight the effect of varying coupling strength for a fixed propagation loss of 5 dB/m and lossless couplers. The spectra have a unique shape (but not unique extinction ratio) based on the propagation loss and coupling strength, which we use to perform fits to our data. When the round trip loss is

low, the effect of excess loss is the same as adding round trip loss, and directly effects the Q factor as shown below [11]:

$$Q_{load} = \frac{2\pi n_{eff} L}{\lambda} \left[\sum \kappa_c + \alpha_{Np/m} L + (1-\gamma) \right]^{-1} \tag{2.17}$$

2.4   Summary of Chapter

In this chapter, we have overviewed the main benefits of the ULLW platform and its application to narrow-band resonant structures. We outlined the ULLW fabrication and propagation loss results of 0.045 ± 0.04 dB/m for the $40\,\text{nm} \times 13\,\mu\text{m}$ bonded cladding geometry near 1580 nm. Then we gave a theoretical background for waveguide coupled ring resonators, including their Q factor and spectra dependence on coupling strength and device losses.

2.5   References

[1]   R. Adar, M. R. Serbin, and V. Mizrahi, "Less than 1 dB per meter propagation loss of silica waveguides measured using a ring resonator," *J. Light. Technol.*, vol. 12, no. 8, pp. 1369–1372, 1994.

[2]   T. Kominato, Y. Hida, M. Itoh, H. Takahashi, S. Sohma, T. Kitoh, and Y. Hibino, "Extremely low-loss (0.3 dB/m) and long silica-based waveguides with large width and clothoid curve connection," in *Proceedings of ECOC*, 2004, pp. 5–6.

[3]   J. F. Bauters, M. J. R. Heck, D. D. John, J. S. Barton, C. M. Bruinink, A. Leinse, R. G. Heideman, D. J. Blumenthal, and J. E. Bowers, "Planar waveguides with less than 0.1 dB/m propagation loss fabricated with wafer bonding.," *Opt. Express*, vol. 19, no. 24, pp. 24090–24101, Nov. 2011.

[4]   D. T. Spencer, Y. Tang, J. F. Bauters, M. J. R. Heck, and J. E. Bowers, "Integrated Si₃N₄/SiO₂ ultra high Q ring resonators," in *IEEE Photonics Conference 2012*, 2012, pp. 141–142.

[5]   J. F. Bauters, M. J. R. Heck, D. D. John, J. S. Barton, D. J. Blumenthal, J. E. Bowers, C. M. Bruinink, A. Leinse, and R. G. Heideman, "Ultra-low-loss (< 0.1 dB/m) planar silica waveguide technology," *IEEE Photonic Soc. 24th Annu. Meet.*, pp. 1–3, Oct. 2011.

[6]   M. J. R. Heck, J. F. Bauters, M. L. Davenport, D. T. Spencer, and J. E. Bowers, "Ultra-low loss waveguide platform and its integration with silicon photonics," *Laser Photon. Rev.*, vol. 8, no. 5, pp. 667–686, Sep. 2014.

[7]   J. F. Bauters, M. J. R. Heck, D. Dai, J. S. Barton, D. J. Blumenthal, and J. E. Bowers,

"Ultralow-Loss Planar Si$_3$N$_4$ Waveguide Polarizers," *IEEE Photonics J.*, vol. 5, no. 1, Feb. 2013.

[8] K. Hiremath and M. Hammer, "Circular Integrated Optical Microresonators: Analytical Methods and Computational Aspects," in *Photonic Microresonator Research and Applications*, I. Chremmos, O. Schwelb, and N. Uzunoglu, Eds. New York: Springer, 2010.

[9] B. J. Orr and Y. He, "Rapidly swept continuous-wave cavity-ringdown spectroscopy," *Chem. Phys. Lett.*, vol. 512, no. 1–3, pp. 1–20, Aug. 2011.

[10] Chin-Lin Chen, "Optical Directional Couplers and Their Applications," in *Foundations for Guided-Wave Optics*, New Jersey: John Wiley & Sons, Inc., 2007.

[11] O. Schwelb, "Transmission, Group Delay, and Dispersion in Single-Ring Optical Resonators and Add/Drop Filters—A Tutorial Overview," *J. Light. Technol.*, vol. 22, no. 5, pp. 1380–1394, May 2004.

3 Demonstration of Ultra-low Loss Si$_3$N$_4$ Resonant Devices

In this chapter we will overview our contributions to ultra-high Q ring resonators on the Si$_3$N$_4$ platform. By manipulating the waveguide core geometries and directional coupler layouts we will demonstrate single and multimode ring resonators with an ultra-high Q$_{int}$ of 81 million.

3.1 *Single Mode ULLW Resonators[3]*

3.1.1 Directional Coupler Design

We begin by studying the most basic ring resonator structures, namely single bus resonators and add-drop resonators with two identical directional couplers. To design the directional couplers, we utilize BeamProp simulations in addition to previous fabrication runs. Experimental coupler values are the most valuable as the simulated κ is dependent on the exact Si$_3$N$_4$ thickness and large area structures require large simulation domains and computing time. The corollary is that we get very few devices per mask as the minimum bend radius is close to 10 mm for the 40 nm bonded cladding layout and 1 mm for the 90 nm bonded and sputtered cladding layouts. An example of a BeamProp simulation is shown in Figure 3.1, with the dependence on gap and bend radius at 1550 nm.

---

[3] *Much of the analysis and figures of this section has been reproduced from* [2], [3].
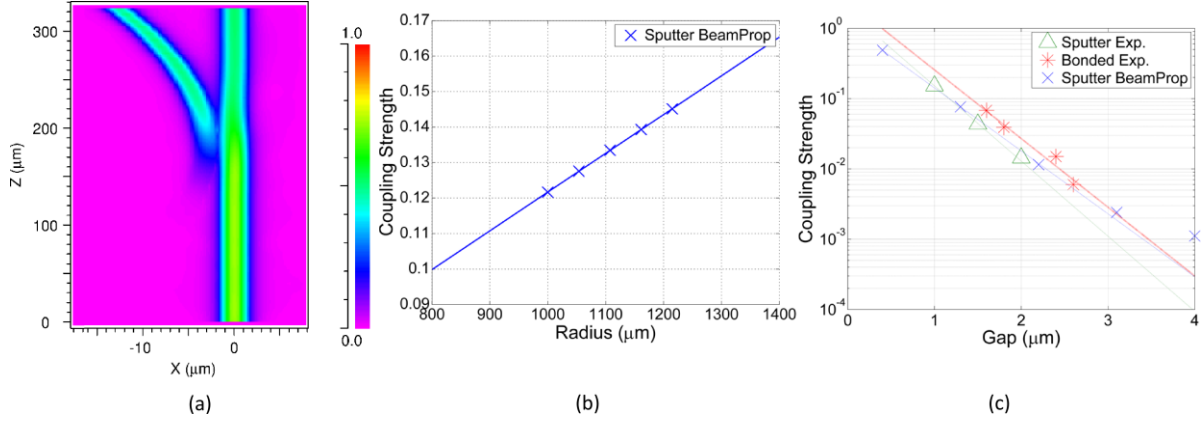
Figure 3.1) BeamProp simulations of a 2.8 µm×90 nm waveguide with sputtered top cladding. (a) Intensity map, (b) coupling vs. bend radius at 1.086 µm gap, and (c) coupling vs. gap compared to experimental bonded and sputtered top cladding.

3.1.2   Characterization Methods

With the appropriate coupling gaps now designed for standard directional couplers, we fabricate single mode rings on the various waveguide geometries. Measurement of the high Q resonators was done in the frequency domain using tunable external cavity lasers (Agilent 86142A: 1510-1640 nm, Thorlabs TLK-L1300M: 1310 nm, Thorlabs TLK-L1050M: 1060 nm). The slowest sweep speeds were used so as to avoid any ringdown effects that could occur [1]. Cleaved or 2 µm lensed SMF28 fiber was used for coupling in/out of the 40 nm and 90 nm devices, respectively. The output was then coupled to a high-responsivity InGaAs detector (Thorlabs DET01CFC) and terminated on a 1 GHz oscilloscope (Tektronix TDS5104B) to enable high data rate acquisition. A polarization controller was also used on the input to excite the lower loss TE polarization. The TM polarization, which has a lower confinement and higher bend loss than the TE_0 mode, was not excited due to the polarizing nature of s-bends on the Si_3N_4 platform as mentioned previously. All results are then averaged over multiple closely spaced resonances within 0.5 nm. A setup schematic is

shown in Figure 3.2, and top down view of an excited 1.54 mm resonator is shown in Figure

3.3
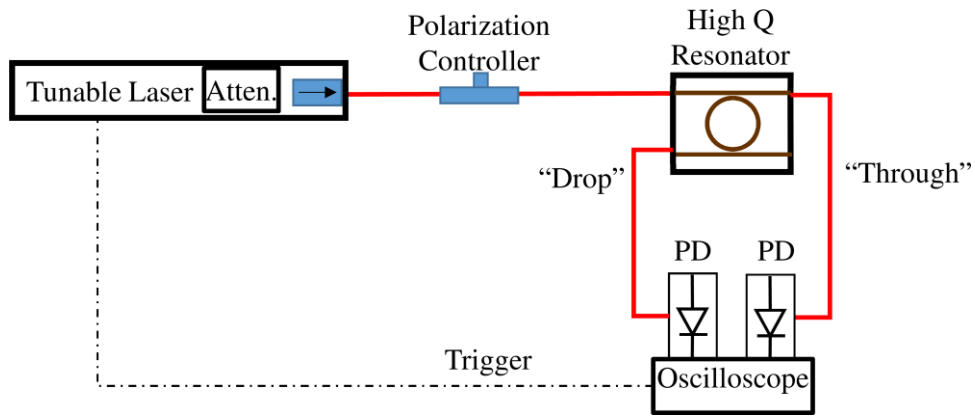
Figure 3.2) Frequency domain measurement setup for the high Q resonators.
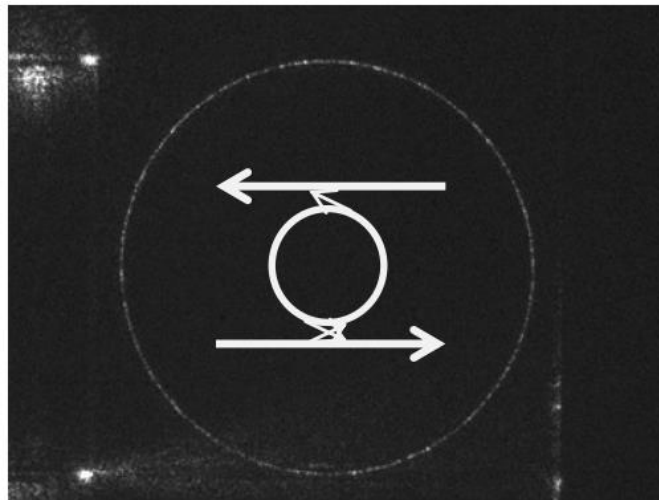
Figure 3.3) Top view infrared image of an ULLW resonator on resonance. The input and drop port facet reflections appear on the left side. From [2] © 2012 IEEE.

3.1.3 Initial Results

Initial single mode add-drop resonance results are highlighted in Table 3.1. For various

bend radii (R), waveguide width (w), and core thickness (t), we observe Q_{int} of 7 million at

1550 nm, 28 million at 1310 nm, and 19 million at 1060 nm. These results were fabricated

with a plasma enhanced chemical vapor deposition (PECVD) deposited upper cladding, and

have two important implications. First, for very thin waveguide cores, the bend loss becomes

too large at 1550 nm, concluding that we need higher quality cladding material and higher bend radius than 5 mm to confine the mode at low loss. Additionally, the increase in Q factor with decreasing wavelength means that undercoupled (lower κ_c) resonators are showing lower total losses and directional couplers could have a large effect on this loss. One would expect losses to increase at lower wavelengths if it were scattering loss limited, however, the total loss decreases with lower wavelength and requires study of the directional coupler's effect on loss.

Table 3.1) Overview of extracted Q$_{int}$ and Propagation Losses for Various Resonators. From [3] © 2011 OSA.

	1550 nm	1310 nm	1060 nm
R=5mm,t=40nm, w=5.3µm	No transmitted power *	High loss **	Q = 18 million
			2.1 dB/m
R=5mm,t=50nm, w=5.3µm	Q = 1 million	Q = 28 million	Q = 19 million
	20.8 dB/m	1.1 dB/m	2.0 dB/m
R=4mm,t=50nm, w=5.3µm	High loss **	Q = 21 million	Q = 11 million
		1.5 dB/m	3.5 dB/m
R=2mm,t=80nm, w=2.8µm	Q = 7 million	Multi-mode ***	Multi-mode ***
	2.9 dB/m		

* No transmitted power was observed through a straight waveguide due to large optical leakage to the substrate.
** The loss is too large to be extracted by ring resonance spectra. No resonance spectra are observed.
*** The waveguide dimensions cause the waveguide to be strongly multi-mode at the given wavelength

3.1.4 Improved Single Mode Resonators

The previous wavelength study shows that we need higher bend radius, better upper cladding, and improved directional couplers. The highest Q factor resonators are then fabricated on the 40 nm bonded cladding layout. The bend radius is increased to 9.8 mm and the waveguide width is maximized to 7 µm to keep it in a simulated single mode regime. The coupler gaps are also increased so as to achieve optimal coupling in the 1580 nm regime for traditional coupling geometries. The results for 1510-1580 nm are shown in Figure 3.4.
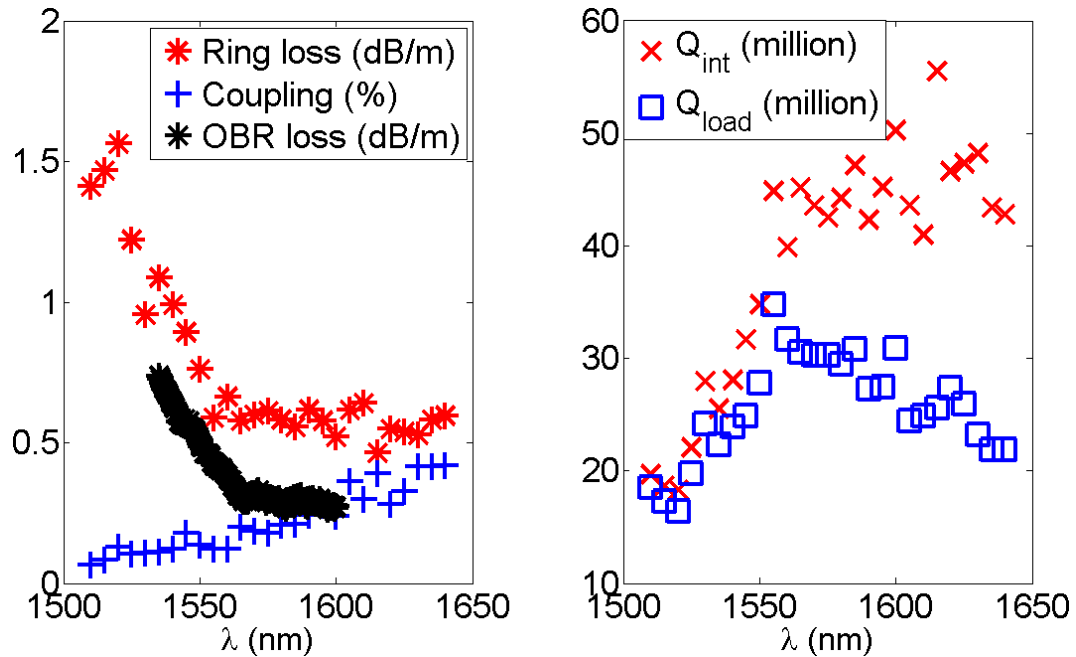
Figure 3.4) Extracted values of coupling loss, propagation loss, Q_{int}, and Q_{load} for the 40 nm×7 μm bonded cladding single mode resonator. From [2] © 2012 IEEE.

The extracted Q_{int} reaches higher levels than our previous results, up to 55 million at 1620 nm. We use Q_{int} to calculate the resonator propagation loss and compare to the measured OBR propagation loss for a 11 mm bend radius delay line spiral. We observe a 0.25 dB/m increase in resonator propagation loss for a similar bend radius spiral delay line. We can condclude that there is excess loss in the resonator system, and we hypothesize that directional couplers are adding the excess loss.

3.1.5   Directional Coupler Excess Losses Measurements
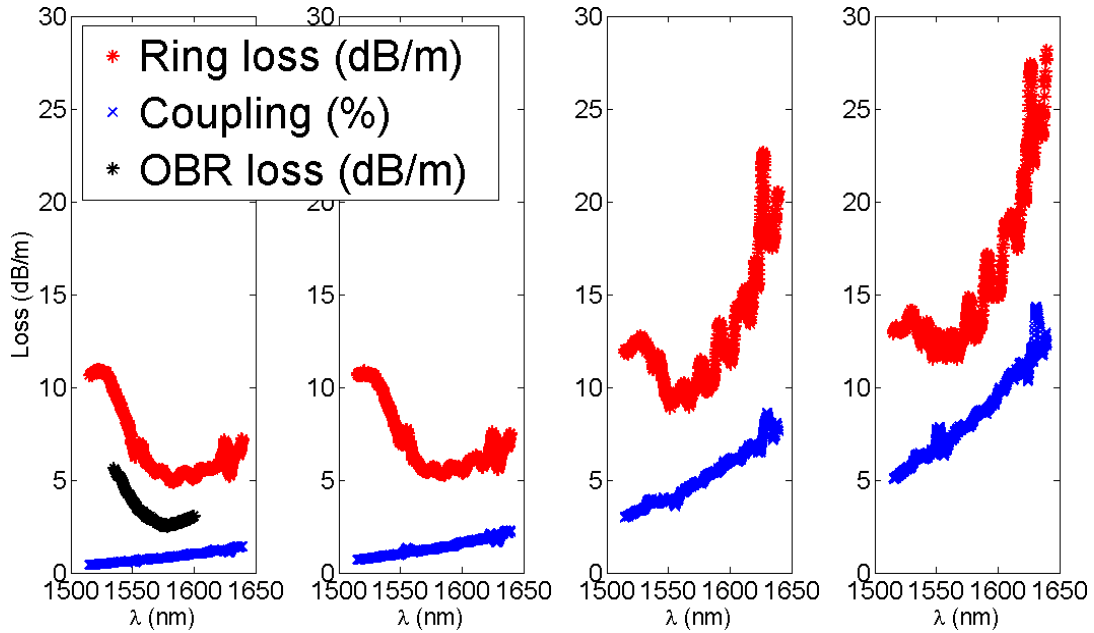
Figure 3.5) Extracted propagation loss and coupling strengths assuming ideal couplers for gaps of (left to right) 2.6, 2.4, 1.8, and 1.6 μm. A baseline OBR delay line spectra is shown on the first plot in black, and a large increase in loss is observed for increased coupler strength. From [2] © 2012 IEEE.

Table 3.2) Extracted values of coupling and excess directional coupler loss for varying gaps. From [2] © 2012 IEEE.

1580nm				
Gap (μm)	2.6	2.4	1.8	1.6
Coupling (%)	0.9	1.4	5.3	8.4
Round Trip Loss (dB)	0.30	0.33	0.60	0.78
Excess Loss (dB/coupler)	0.07	0.09	0.22	0.31

To study the directional coupler excess losses, we fabricate smaller 1.54 mm bend radius, 100 nm bonded cladding resonators. By varying the directional coupler gap, we can study the efficiency of the design. Varying the coupler gap across identical resonators has been a standard practice for extracting the value of κ so long as the round trip loss of the system remains constant. In Figure 3.5, we present our results of extracted round trip loss ($\alpha_{dB/m} * L$) for increasing directional coupler gaps. We observe an increase in loss with increasing coupler strength, thus concluding that a significant portion of the round trip loss is

due to the coupler layout, up to 0.31 dB/coupler as shown in Table 3.2. As we decrease the propagation loss of the waveguide technology, the excess coupler loss will become a limitation to increasing Q factors as it reaches levels on the order of the round trip loss, $\alpha_{dB/m}*L$. If we assume that excess coupler loss has limited our 40 nm bonded cladding high Q resonators presented earlier, this yields a loss of 0.03 dB/coupler, a very low insertion loss, but insufficient for higher Q beyond 55 million.

3.2   *Multimode ULLW Resonators[4]*

To improve upon the single mode resonators fabricated, we must solve two limitations that still persists. First, excess directional coupler losses must be improved with new designs. Second, propagation losses must be lowered by moving to wider waveguide widths in the multimode regime. We now fabricate 40 nm thick by 11 μm wide waveguides due to the fact that only two modes are supported in the geometry. If we utilize the absolute lowest loss width of 13 μm observed in spiral delay lines, there will be 3 supported modes and the coupling design becomes too difficult for system applications requiring efficient coupling to the fundamental TE_0 mode only.

3.2.1   Directional Coupler Design

With 11 μm waveguide widths, we next experiment with novel coupler designs that will lower excess losses while coupling efficiently to the TE_0 mode. Figure 3.6a-c overviews the available coupler layouts. The traditional "straight" directional coupler leaves the input/output bus waveguide at $R_2=\infty$, and we have shown that it creates appreciable excess loss in ultra-high Q resonators. An intuitive coupler design is the "symmetric" coupler, which has $R_2=-R_{ring}$, and creates the best mode matching to all supported modes of the

resonator. However, we are concerned with the most adiabatic, low loss transition from the coupling region to the output facet, and the symmetric coupler has the fastest transition. Previous studies have used pulley couplers with R_1 and R_2 concentric to achieve mode dependent coupling strengths in multimode resonators [4], so this style of coupler is naturally attractive. For our work, we design a weakly tapered pulley coupler using $R_{2=}1.3*R_{ring}$, which utilizes the mode dependence of the pulley coupler in addition to a more adiabatic gap transition that we hypothesize will lower the excess loss of the coupler, shown in Figure 3.6d.
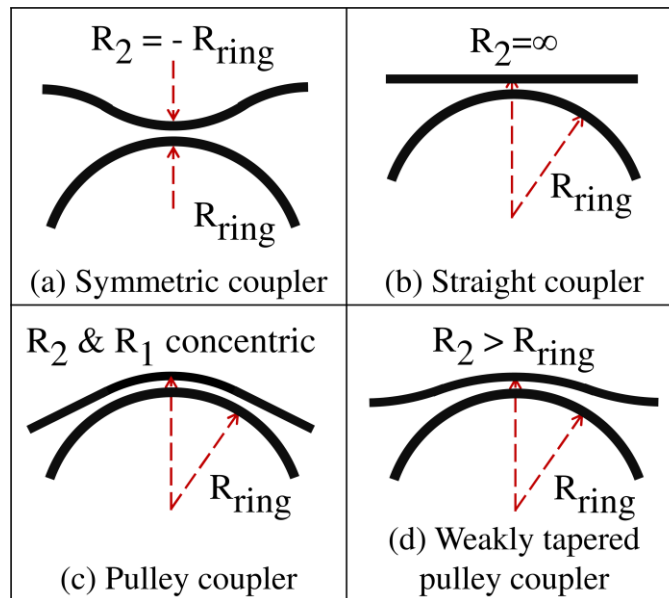
Figure 3.6) Directional coupler layouts for ring resonators. The tapering of the gap is strongest for (a) symmetric coupling and identical for the (b-c) straight and pulley couplers, while the (d) weakly tapered pulley coupler smoothes the gap transition. We fabricated straight and weakly tapered pulley couplers. From [5] © 2014 OSA.

3.2.2 Spectra Analysis and Results

We then implement the weakly tapered pulley coupler onto ULLW resonators with 11 µm × 40 nm core geometry and 9.65 mm bend radius, consistent with a FSR of 3.3 GHz

---

[4] *Much of the analysis and figures of this section has been reproduced from* [5].

near 1580 nm. Since we are working with multiple modes, we simulate the n_{eff} and n_g of the waveguide geometry's two TE modes, while taking into account waveguide and bulk material chromatic dispersion [6], [7]. The excitation of higher order modes can arise from input tapers and/or directional couplers, and can yield closely spaced resonances that would ruin many system applications. With a difference in n_g, a Vernier effect occurs, which we show schematically in Figure 3.7 along with mode simulations. The high n_g mode (TE$_0$) contains one extra resonance across a large wavelength span, termed the beat wavelength, λ_{beat}. The relative extinction ratio (ΔER) is referenced to the high n_g TE$_0$ mode (higher equals stronger TE$_0$ mode coupling). The separation between adjacent resonances of the two transverse modes, $\Delta\lambda_{res}$, increases with wavelength in reference to the high n_g mode. The TE$_0$ mode will thus have $m+1$ FSRs in λ_{beat}, where m is the number of TE$_1$ FSRs. The ratio of group indices is then:

$$\frac{n_{gTE_0}}{n_{gTE_0}} = 1 + \frac{1}{m} \tag{3.1}$$

This Vernier effect is utilized in the next section to detmine the correct mode that creates each resonance dip.
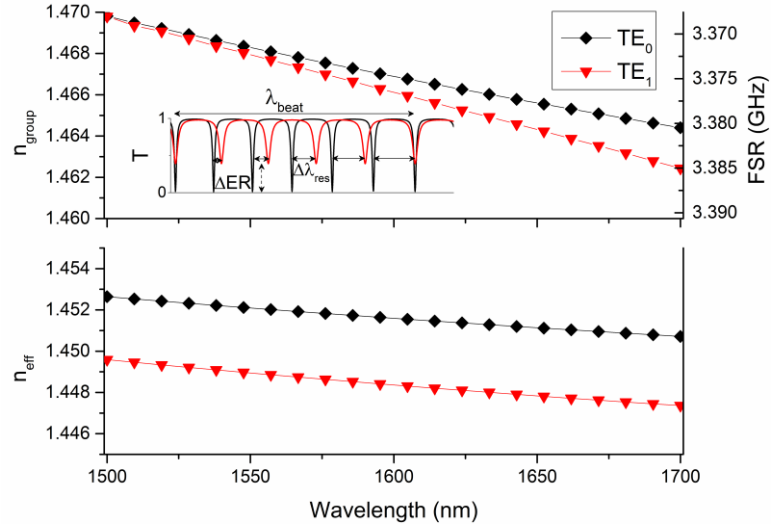
Figure 3.7) Simulated TE_0 and TE_1 effective and group index dispersion for the 11 µm × 40 nm Si_3N_4 multimode waveguides analyzed in this section. The higher n_g for the TE_0 mode creates a relative resonance wavelength separation, $\Delta\lambda_{res}$ and overall beat wavelength, λ_{beat} (inset). From [5] © 2014 OSA.
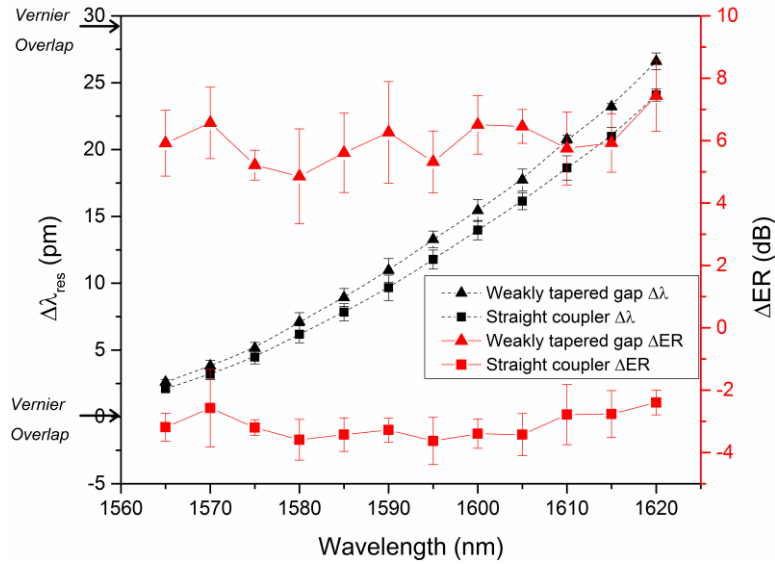
Figure 3.8) Relative resonance wavelengths and ERs for the TE_0 and TE_1 modes across the region of interest. All numbers are taken relative to the fundamental TE_0 mode and averaged over multiple closely spaced resonances every 5 nm. The weakly tapered pulley directional coupler resonator shows a similar beat wavelength of 73 nm as a straight directional coupler resonator, with an increase in absolute and relative ER. From [5] © 2014 OSA.

Initially, we find the relative resonant wavelengths and ER for resonators with straight and weakly tapered pulley directional couplers from 1565-1620 nm. Figure 3.8 compares a 5-µm gap straight coupler with a 3.8-µm weakly tapered pulley coupler. The beat wavelength, λ_{beat}, is extracted from the two overlap points by curve fitting a 2nd order

36

polynomial that accounts for dispersion. Both resonators have the same circumference and show $\lambda_{beat} = (73 \pm 2)$ nm, corresponding to ≈ 2500 resonances across this range. The ratio of n_g between TE_0 and TE_1 is found to be 1.00039 ± 0.00002, which matches well with our simulated ratio of 1.00040 ± 0.00002, for an n_g of 1.4674 and 1.4668, respectively, in the region of interest. Additionally, the ΔER between modes in the two directional coupler designs changes sign. Due to these observations, we conclude that we have achieved stronger coupling to the fundamental TE_0 mode with the weakly tapered pulley directional coupler as compared to the straight directional coupler.
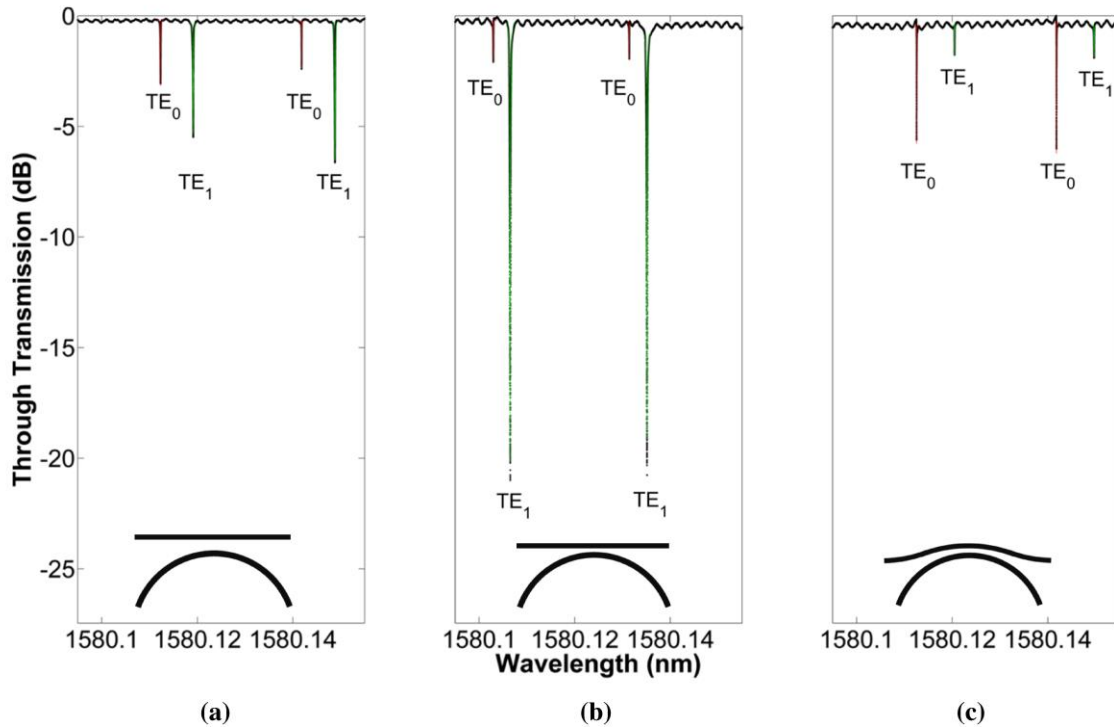
Figure 3.9) Resonator spectra and nonlinear fits near 1580 nm for the 3 different directional coupler designs, (a) 5 μm straight bus waveguide, (b) 3.8 μm straight bus waveguide, and (c) 3.8 μm weakly tapered pulley waveguide. From [5] © 2014 OSA.

Next we look at single resonances at 1580 nm for two different waveguide-resonator bus gaps, 3.8 μm and 5 μm, in Figure 3.9a and b, respectively. The modes are labeled according to the previous modal analysis, and all devices are undercoupled due to the identical coupler

layouts on the add and drop ports. For both straight coupler gaps, the higher order TE_1 mode is coupled much stronger than the lower loss fundamental mode, as observed by the magnitude of the ER. In this regime, the TE_0 mode has a maximum Q_{int} factor of 63 million at a 5-µm gap, similar to the results of the previous section. However, using a weakly tapered pulley directional coupler at a 3.8 µm minimum gap at bus radius of 12.545 mm, we couple stronger and more efficiently to the fundamental TE_0 mode. This has the consequence of a higher ER than for the TE_1 mode, as seen in Figure 3.9c, as well as an even higher Q_{int} factor of 81 million, outlined in Table 3.3. This is the largest Q_{int} factor for a monolithic waveguide coupled resonator system to date.

Table 3.3) Measured and extracted resonator parameters for the three directional coupler designs studied at 1580 nm, assuming no parasitic losses (γ=1).[5] From [5] © 2014 OSA.

gap (µm)	mode	Q_{int} (×10⁶)	Q_{load} (×10⁶)	RTL (dB)	α (dB/m)	κ (%)	ER (dB)
5.0	TE0	63	46	0.026	0.42	0.11	2.7
5.0	TE1	27	13	0.061	1.00	0.72	6.1
3.8	TE0	35	28	0.047	0.78	0.13	1.8
3.8	TE1	41	4	0.038	0.63	4.07	20.2
3.8-taper	TE0	**81**	**42**	**0.019**	**0.32**	**0.20**	**5.6**
3.8-taper	TE1	30	26	0.055	0.90	0.11	1.4

3.3   Summary of Chapter

In this chapter, we have outlined our route to record high 81 million Q factor using ULLW resonators. We reduce propagation loss with 11µm wide waveguides and 9.65 mm bend radius, and reduce excess directional coupler loss with new geometries. Based on the ULLW platform, weakly tapered pulley directional couplers show a critical path forward to higher Q factor integrated resonators that require increasingly efficient and low loss coupling. Improved design of beta matched weakly tapered pulley couplers should help

---

[5] *The bend radius is 9.65 mm and nominal gap widths are shown. The measured Q_{load} and ER allows extraction of the power coupling coefficient (κ), Q_{int}, propagation loss (α), and round trip loss (RTL). The RTL is the upper bound on γ for two directional couplers.*

reduce the loss of directional couplers, and full utilization of the Si_3N_4 platform, with record propagation loss of 0.05 dB/m, should be able to yield resonators with Q_{int} values of 600 million. With a critically coupled resonator ($Q_{int}=Q_c$) and negligible excess coupler loss, this corresponds to a 300 million Q_{load}.

3.4 References

[1]   A. A. Savchenkov, A. B. Matsko, V. S. Ilchenko, and L. Maleki, "Optical resonators with ten million finesse," *Opt. Expressxpress*, vol. 15, no. 11, pp. 6768–6773, May 2007.

[2]   D. T. Spencer, Y. Tang, J. F. Bauters, M. J. R. Heck, and J. E. Bowers, "Integrated Si_3N_4/SiO_2 ultra high Q ring resonators," in *IEEE Photonics Conference 2012*, 2012, pp. 141–142.

[3]   M.-C. Tien, J. F. Bauters, M. J. R. Heck, D. T. Spencer, D. J. Blumenthal, and J. E. Bowers, "Ultra-high quality factor planar Si_3N_4 ring resonators on Si substrates.," *Opt. Express*, vol. 19, no. 14, pp. 13551–13556, Jul. 2011.

[4]   Q. Li, A. A. Eftekhar, M. Sodagar, Z. Xia, A. H. Atabaki, and A. Adibi, "Vertical integration of high-Q silicon nitride microresonators into silicon-on-insulator platform," *Opt. Express*, vol. 21, no. 15, pp. 18236–18248, Jul. 2013.

[5]   D. T. Spencer, J. F. Bauters, M. J. R. Heck, and J. E. Bowers, "Integrated waveguide coupled Si_3N_4 resonators in the ultrahigh-Q regime," *Optica*, vol. 1, no. 3, pp. 153–157, Sep. 2014.

[6]   H. R. Philipp, "Optical Properties of Silicon Nitride," *J. Electrochem. Soc.*, vol. 120, no. 2, pp. 295–300, Feb. 1973.

[7]   T. Bååk, "Silicon oxynitride; a material for GRIN optics," *Appl. Opt.*, vol. 21, no. 6, pp. 1069–1072, Mar. 1982.

4 Novel Si$_3$N$_4$ Resonant Devices

In this chapter we will first overview a novel resonant splitting device based on the ULLW platform, and its excellent performance in terms of uniformity and insertion loss. Then we will highlight a dual layer Si$_3$N$_4$ technology of high and low confinement waveguides fabricated simultaneously, allowing for routing of low loss and low bend radius signals on the same wafer.

4.1   1×16 ULLW Resonant Splitter[6]

Here we will present the first experimental demonstration of a novel ring resonator based 1×N optical power splitter. The device is fabricated on the 40 nm ULLW bonded cladding platform, and can provide both low loss and high uniformity to applications requiring filtering and distribution of signals. A system requiring a large number of clock signals with optical interconnects could benefit from lower losses and higher uniformity across ports [1], [2]. Future passive optical networks requiring wavelength and time division multiplexing (hybrid-PON) across multiple FTTx nodes could gain additional benefit from a device with wavelength selectivity [3]. While our current Si$_3$N$_4$ design is not directly compatible with data communication applications, it is very useful for narrow linewidth laser applications as well as arbitrary splitting ratios, such as in arrayed waveguide gratings (AWG) [4], to be discussed later.

---

[6] *Much of the analysis and figures in this section are reproduced from* [5].
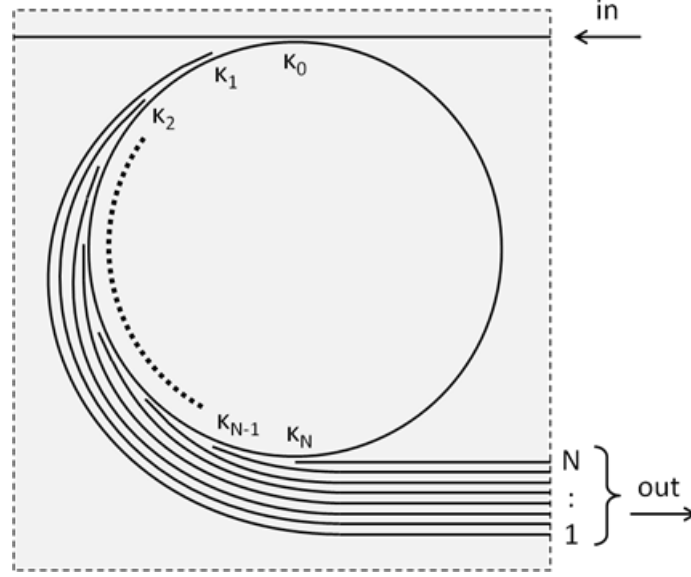
Figure 4.1) Schematic for a 1×N ring resonator based power splitter. From [5] © 2013 IEEE.

4.1.1 Device Design and Fabrication

Figure 4.1 illustrates the layout for a general 1×N wavelength selective power splitter. To demonstrate the usefulness of this device, we fabricate a 1×16 power splitter designed after the theoretical basis in [6]. N+1 directional couplers are added tangent to a waveguide ring resonator. To design a critically coupled system in which we can reduce the splitting loss, we use the following design rule

$$t_0^2 = \xi^2 \prod_{i=1}^{N} t_i^2 \tag{4.1}$$

where ξ is the round trip propagation loss in the ring and $\kappa_{c,o}(t_o), \kappa_{c,i}(t_i)$ denote the amplitude coupling (transmission) of the input and i^{th} output port, respectively. To achieve uniform coupling, we match the outputs at two neighboring couplers such that

$$\frac{P_{i+1}}{P_i} = \frac{\kappa_{c,i+1}^2}{\kappa_{c,i}^2} \xi^{\frac{\Delta\theta}{\pi}} t_i^2 \tag{4.2}$$

41

where $\xi^{\frac{\Delta\theta}{\pi}}$ is the propagation loss from the *i+1* to the *i*-th directional coupler spaced by $\Delta\theta$ radians. To design a perfectly uniform splitter such that Equation (4.2) equals unity, each coupler must be accurately fabricated to a designed coupling strength, which can be difficult to control. Our strategy is to reduce the coupling strength to avoid any large mismatch or nonideality and make identical output couplers. Since we have ULLW resonators with Q factors values in excess of 1 million, we assume $\xi^{\frac{\Delta\theta}{\pi}} \approx 1$, and finally choose $\kappa_o^2 \approx N\kappa_i^2$. According to calculations based on a designed κ_o / κ_i of 2%/0.1%, the theoretical nonuniformity is < 0.1 dB when the waveguide loss is <50 dB/m. Operation at 1550 nm was targeted and the directional couplers' optical bandwidth over which Equation (4.1) would apply was not measured in this study. Fabrication of the 1×16 ring resonator power splitter utilizes the ULLW bonded cladding platform with a single mode geometry of 7 μm × 40 nm. Figure 4.2 is a photograph of a fabricated device (outer ring) without the top silicon substrate.
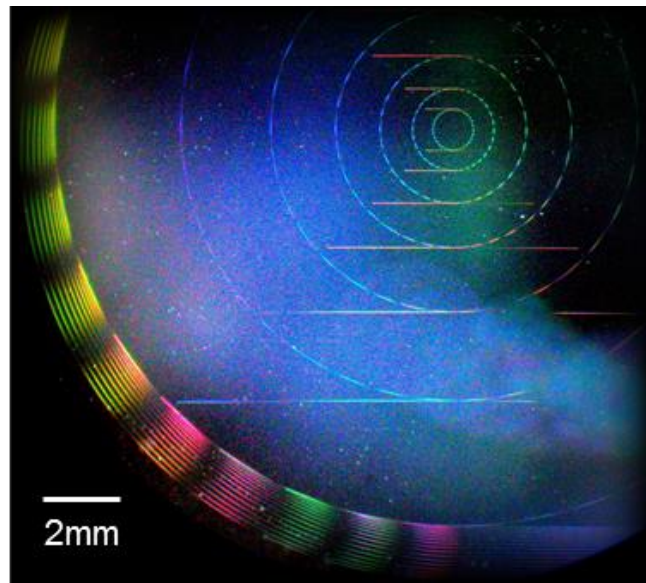
Figure 4.2) Top down photograph of the Si$_3$N$_4$ ring resonator power splitter. The 16 output drop ports are shown along the outer edge. From [5] © 2013 IEEE.

4.1.2 Measurement and Results

To characterize the 1×16 ring resonator power splitter, two measurements were performed. First, a near field image of each output facet was taken using a 20× objective, collimating optics, and an infrared camera. The stitched images of all 16 ports are shown in Figure 4.3, where an intensity mapping yields a uniformity of <0.4dB.
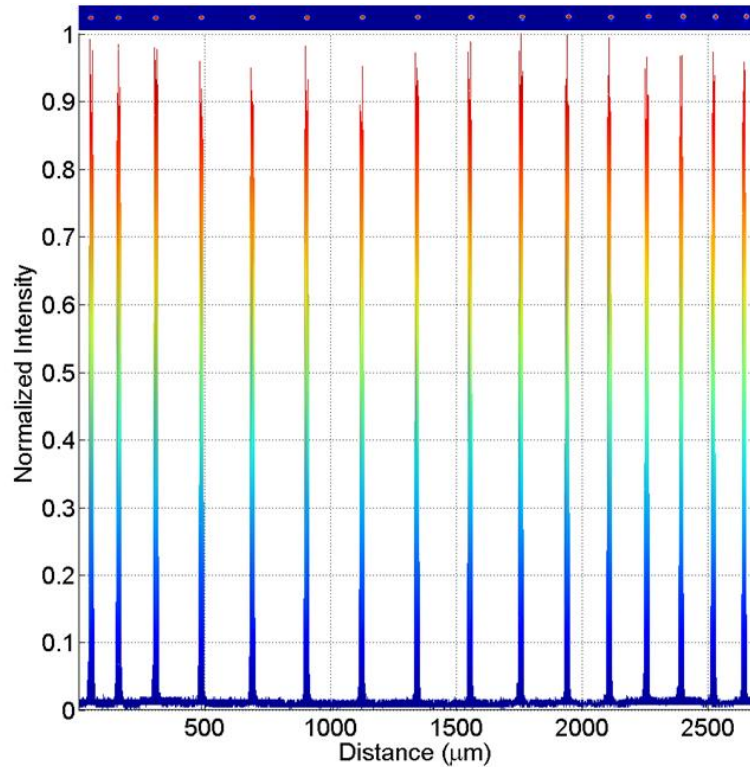
Figure 4.3) Near field intensity map of the 16 output port facets. Non-uniform output waveguide separation was allowed in the design. From [5] © 2013 IEEE.

Second, to study the excess loss as well as confirm the uniformity, we measure the resonance spectra using the same narrow linewidth laser sweep discussed previously. Cleaved SMF28 optical fiber was butt coupled to the waveguides, and index matching fluid was used to decrease facet loss and reflection. The coupling loss was measured in reference to fiber to fiber coupling and found to be 1.4 dB/facet assuming negligible straight waveguide loss. Each drop port was measured and assumed to have uniform collection

efficiency. A typical spectrum of the through port (red curve) and one output port (blue curve) is shown in Figure 4.4, which has a measured drop port extinction ratio of >25 dB and bandwidth of 33 MHz. The corresponding finesse and Q_{load} are 100 and 6 million, respectively.
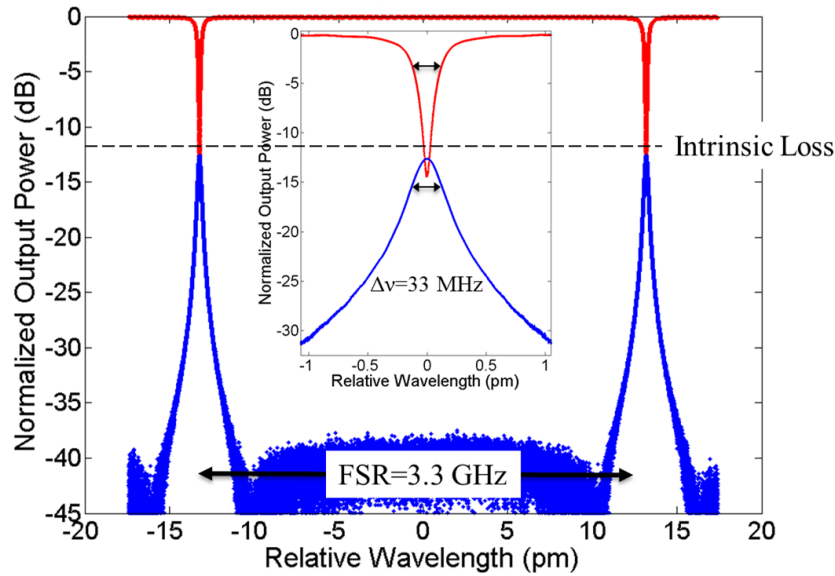
Figure 4.4) Optical spectrum of the through port (red) and a typical output drop port (blue). From [5] © 2013 IEEE.

The power measured on resonance at each port is normalized to the through port transmission off resonance (≈1 for high Q). After subtracting the intrinsic splitting loss of 12 dB (1/16), the ring power splitter shows excess loss of 0.9 dB and maximum to minimum uniformity of 0.4 dB. Most of the nonuniformity is due to ~0.2 dB alignment error when butt coupling the fiber and waveguides. The somewhat long propagation distance of ~5 cm at 1 dB/m (conservative estimate from Q_{load}) yields a negligible loss of <0.05 dB that is within our measurement error. The results are plotted in Figure 4.5 and compared to typical 1×16 MMI splitters, Y branches, and 19×19 star couplers. The resonant splitter shows good improvement of 0.3 dB excess loss and 0.2 dB uniformity over cascaded Y branch power splitters [7]. Compared to more recent cascaded Y branch power splitters written with deep

UV stepper lithography, we show 0.2 dB worse uniformity, but benefit from lower insertion loss by 1.3 dB [8]. When compared to MMI and star couplers, there is a substantial improvement in excess loss and uniformity of 1.8 dB and 1.1 dB, respectively [9], [10]. Additionally, recent AWG devices on the ULLW platform have shown very low excess loss of 0.5 dB using 2 star couplers with 16 channels [11].Overall, the ring power splitter performs nearly the same as conventional broadband power splitters in terms of excess loss and uniformity, but has some special features to be discussed in the next section.
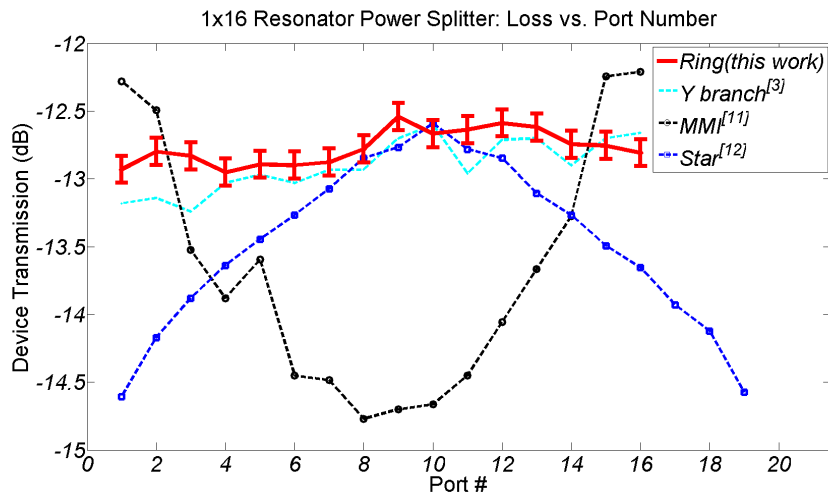
Figure 4.5) Transmission and uniformity device comparison between the 1×16 ring resonator power splitter of this work and typical Y branch, MMI, and star couplers seen in literature. From [5] © 2013 IEEE.

4.1.3 Applications

The ring based power splitter has some unique features as compared to the conventional splitters shown in Figure 4.5. While the narrow-band transmission rules out applications like data- and telecommunication routing, it is perfectly suitable for fields where spectrally pure laser lines and combs are required, e.g., in microwave photonics, metrology, biophotonics, and as a source for (D)WDM systems. Additionally, the splitting ratio can be arbitrarily chosen by tuning the directional coupler strengths of the *N* outputs. This adds significant

flexibility over the power splitters mentioned earlier. As an example, a ring based power splitter can replace a star coupler in an AWG. Such star couplers are inherently high loss due to the finite lithography and etch resolution [4]. Ring-based power splitters can be designed to impose a Gaussian profile over the array arms, ensuring low loss and low-crosstalk performance. When an integer FSR of the ring is matched to the AWG channel spacing, consecutive narrow passbands end up in adjacent channels.

A particularly interesting application of such an AWG is a multi-wavelength or digitally tunable laser [12], [13]. The concept is schematically shown in Figure 4.6. The *N* outputs of the ring splitter feed the array arms which have a length difference ΔL corresponding to an integer multiple of the ring FSR. A broadband star coupler can be used to combine the array arms, just like a conventional AWG, without requiring alignment of two narrow-band splitters. The laser cavity is then defined by the facets. By individually biasing the semiconductor optical amplifiers (SOAs) in the output channels, lasing is obtained at the wavelength corresponding to the AWG filter position. Due to the narrow AWG bandwidth, resulting from the high Q ring, very narrow linewidths are feasible. Moreover the wavelength grid is defined by the ring and mode-hopping is eliminated.
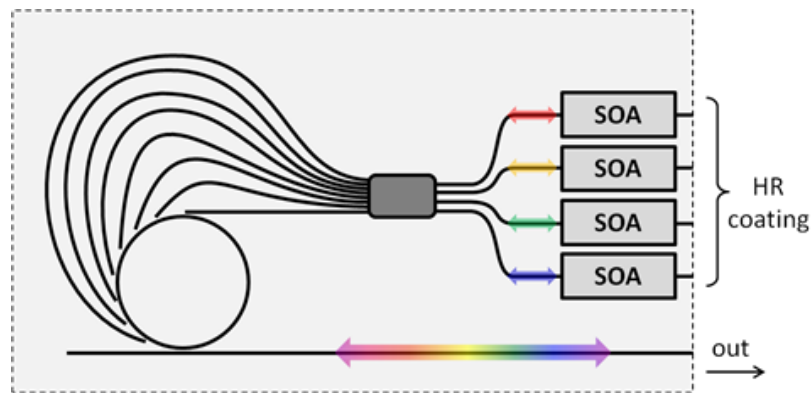
Figure 4.6) Schematic of a narrow-linewidth multi-wavelength laser. Semiconductor optical amplifiers (SOAs) provide the gain and the cavity is formed by the facets mirrors. From [5] © 2013 IEEE.

4.1.4   Conclusion

We have presented a novel splitter architecture based on a ring resonator that offers a uniform, low loss solution to wavelength selective power splitting. The fabricated devices show excess loss of 0.9 dB and uniformity of 0.4 dB across all 16 ports. In comparison to broadband power splitters, this approach offers improved uniformity and excess loss in a wavelength selective device that does not require cascaded stages. The narrowband nature of this device makes it especially useful for systems requiring high spectral purity, such as frequency combs. The layout and fabrication also make this device easily scalable to larger number of output ports while maintaining good uniformity.

4.2   *Dual Layer Si₃N₄ Platform*[7]

4.2.1   Introduction

While the 40 nm bonded cladding ULLWs have the advantage of absolute lowest propagation loss, there is a tradeoff if the application requires local thermal tunability or sub-millimeter bend radii. A dual stripe Si_3N_4 geometry is useful for this purpose, and tunable filters and beamforming devices have been demonstrated with a compact footprint of 70 μm bend radius [14]. In this section, we introduce a novel combination of these two regimes, ultra-low loss and small bend radii propagation, on the same wafer.

4.2.2   Fabrication

The dual layer waveguide fabrication is shown in Figure 4.7, and is somewhat different from the standard ULLW process. The wafer contains high contrast and low contrast regions, fabricated using the LioniX B.V. TriPleX™ technology [15]. To begin, a 500 μm

thick silicon wafer with 15µm of thermal oxide is used as a substrate for LPCVD. The layer stack is 40 nm Si_3N_4, 100 nm SiO_2, and 175 nm Si_3N_4. The thickness of the top Si_3N_4 layer is tapered to zero in the transition regions and low contrast regions. Both waveguide geometries are then patterned simultaneously. Three 1.1 µm layers of SiO_2 are deposited, with an 1150°C anneal after each deposition. The wafer is then smoothed with a chemical mechanical polish (CMP) to remove topography from the waveguide definition.
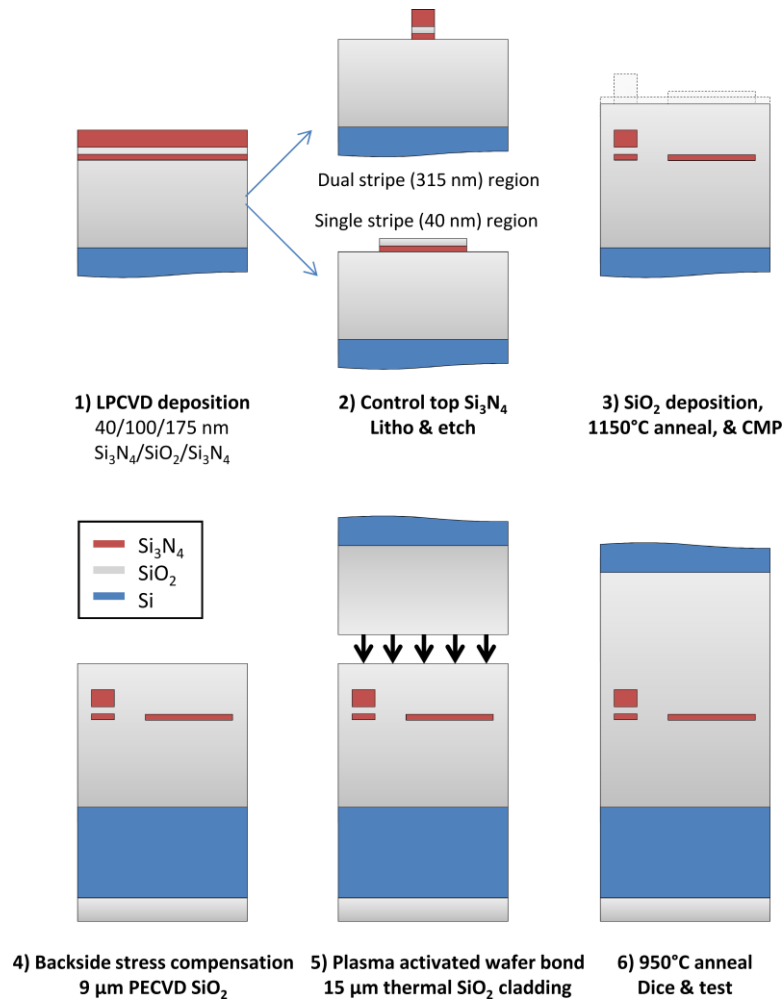
Figure 4.7) Process flow for the dual layer nitride platform.

	Dual stripe TE	Dual stripe TM		Single stripe TE	Single stripe TM
n_{eff}/n_g	1.529/1.741	1.472/1.576	n_{eff}/n_g	1.450/1.466	1.446/1.450
A_{eff}	1.7 μm^2	3.4 μm^2	A_{eff}	23 μm^2	97 μm^2
Γ_{Si3N4}	31%	11%	Γ_{Si3N4}	1.9%	0.3%
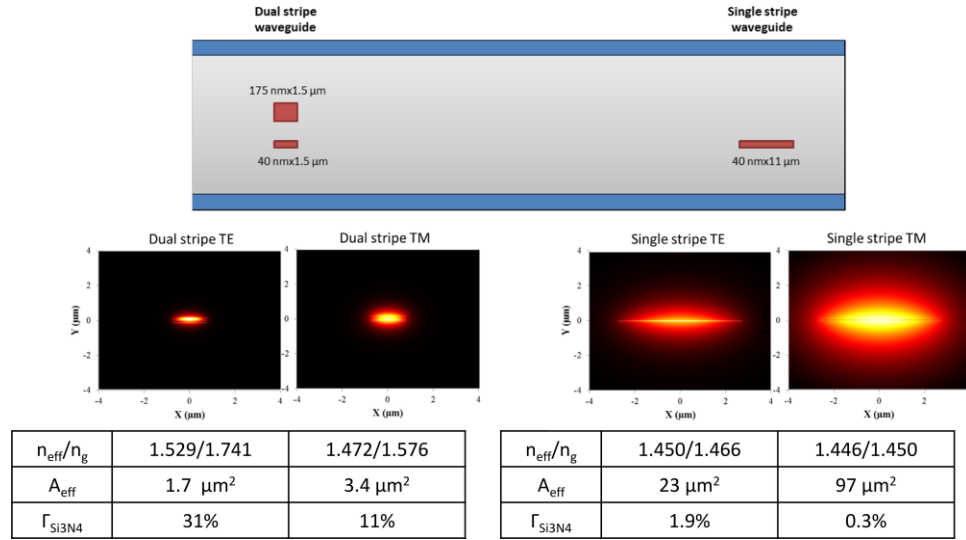
Figure 4.8) Waveguide geometries, mode profiles, and simulated properties that are integrated on the same wafer for high contrast TE/TM, and low contrast TE propagation. n_{eff}: effective index, n_g: group index, A_{eff}: effective mode area, Γ_{Si3N4}: confinement in Si$_3$N$_4$.

After the waveguide fabrication and CMP, the wafer's curvature, or bow, was quite high and required compensation. To achieve this, the wafer was inverted and 9 μm of inductively coupled plasma (ICP)-based plasma enhanced CVD (PECVD) oxide was deposited on the backside to reduce the total bow to 50 μm. A second 500 μm thick silicon wafer with 15 μm of thermal oxide was wafer bonded to the top surface after oxygen plasma activation. A one hour anneal at 300°C under pressure was used to improve the bonding, and a 950°C anneal and facet dicing finalized the process. The simulated TE and TM modes of the platform are shown in Figure 4.8, which achieve a large difference in waveguide confinement (Γ) and effective mode area (A_{eff}). These properties will help us to achieve low loss and low bend radius with the same wafer level technology.

4.2.3 Waveguide Characterization

To characterize the waveguide platform, spirals, ring resonators, and taper loss test structures were patterned for the low and high contrast regions. The input and output waveguides were in the low contrast geometry regardless of test structure, which allowed for

more efficient fiber to chip coupling. Using the OBR to test the propagation loss, low contrast spiral delays at >10 mm bend radius were measured to have a low TE loss of 0.48 ± 0.10 dB/m at 1590 nm. The high contrast waveguides supported two modes, with TE showing 20.1 ± 0.3 dB/m at 1600 nm down to 300 μm bend radius, and the TM mode showing 7.1 ± 0.3 dB/m at 1600 nm down to 650 μm bend radius.

With the two waveguide geometries available, we also fabricated cascaded resonators and measured the through response of the system. The difference in allowable bend radii and loss allow for novel combinations of FSRs and Q factors. Figure 4.9 shows a cascaded resonator system with a 9.65 mm radius ring in the low contrast region coupled to a 1.34 mm ring in the high contrast region. Laser frequency sweeps of the TE spectra are found to have group indices of 1.51 and 1.73, and Q_{load} of 15 million and 0.3 million for the low and high contrast regions, respectively.
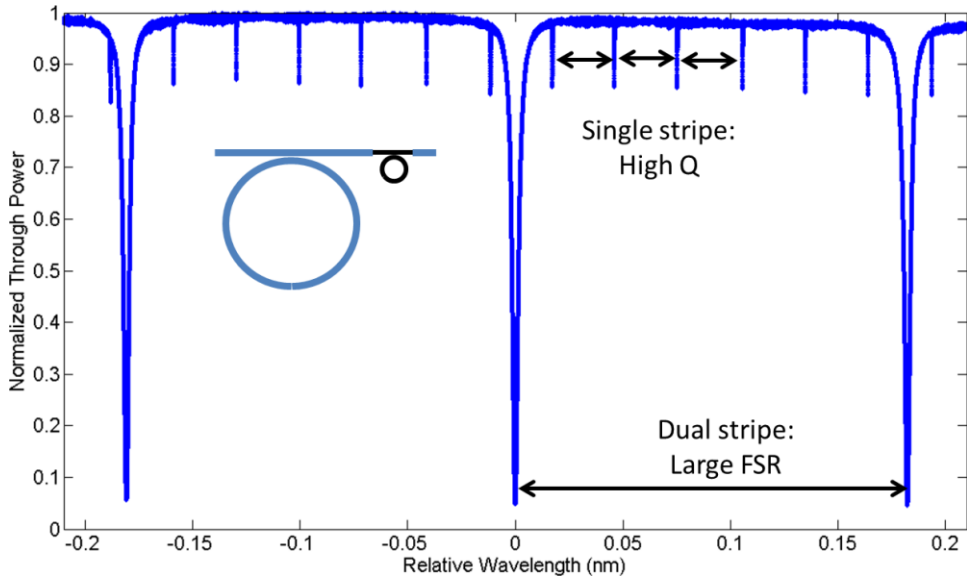
Figure 4.9) Ring resonator measurements of cascaded through ports for the high contrast (large FSR) and low contrast (narrow bandwidth) regions.

4.2.4 Taper Characterization

To determine the on chip transition loss between the two mode geometries, straight waveguides with an increasing number of taper regions were fabricated and tested. Due to difficulties in coupling a single wavelength source, the OBR was used to scan wavelength while observing spatially resolved backscatter in between the tapers. The OBR results of 22 tapers are shown in Figure 4.10. After the facet reflection region, we see an increase in waveguide backscatter at the first taper, since more of the high contrast mode overlaps with the sidewalls. The strongest reflections offset the data near the facets, but we observe 5 consecutive transition regions, each of which includes 2 tapers. Using the relative backscatter level in these regions, we extract a taper loss of 0.35 ± 0.06 dB/taper averaged over the C+L bands.
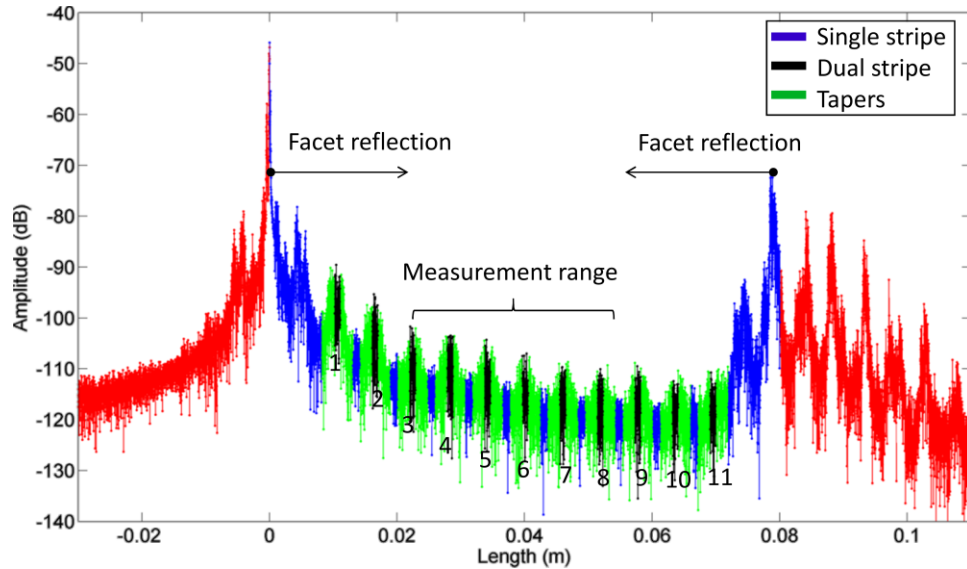
Figure 4.10) OBR trace of 11 mode transition regions (22 tapers). Facet reflections disturb measuring all but the 5-9 transitions, which are used to extract a taper loss of 0.35 ± 0.06 dB/taper.

4.2.5 Conclusion

We have shown a novel combination of Si_3N_4 waveguide platforms that is promising for integrating low propagation loss waveguides with tight bending radii regions. The ability to

transition between the two waveguides at a low coupling loss will allow for the integration of more complex integrated circuits that require varying loss and footprint requirements. For example, one could envision a cascade of resonators to create narrowband Vernier filters. The low contrast waveguides could be utilized for narrowband filtering, while the high contrast waveguides would provide a higher free spectral range for high frequency microwave photonic applications.

4.3   Summary of Chapter

In this chapter, we have expanded upon a novel resonant power splitter that utilizes ULLW resonators and well controlled coupling strengths to achieve excess coupling loss of 0.9 dB and maximum to minimum uniformity of 0.4 dB. In collaboration with Lionix, we have outlined the results of a novel dual-layer waveguide technology that achieves low TE loss of 0.48 ± 0.10 dB/m on the single stripe regions, 20.1 ± 0.3 dB/m for high contrast regions down to a 300 μm bend radius, and a transition loss of 0.35 ± 0.06 dB/taper.

4.4   References

[1]   A. V Mule, S. Member, E. N. Glytsis, S. Member, T. K. Gaylord, J. D. Meindl, and L. Fellow, "Electrical and Optical Clock Distribution Networks for Gigascale Microprocessors," vol. 10, no. 5, pp. 582–594, 2002.

[2]   P. J. Delfyett, D. H. Hartman, and S. Z. Ahmad, "Optical Clock Distribution Using a Mode-Locked Semiconductor Laser Diode System," *J. Light. Technol.*, vol. 9, no. 12, pp. 1646–1649, 1991.

[3]   L. G. Kazovsky, W.-T. Shaw, D. Gutierrez, N. Cheng, and S.-W. Wong, "Next-Generation Optical Access Networks," *J. Light. Technol.*, vol. 25, no. 11, pp. 3428–3442, Nov. 2007.

[4]   M. K. Smit and C. Van Dam, "Phasar-Based WDM-Devices: Principles, Design and Applications," *IEEE J. Sel. Top. Quantum Electron.*, vol. 2, no. 2, pp. 236–250, 1996.

[5]   D. T. Spencer, D. Dai, Y. Tang, M. J. R. Heck, and J. E. Bowers, "Realization of a Novel 1xN Power Splitter With Uniformly Excited Ports," *IEEE Photonics Technol. Lett.*, vol. 25, no. 1, pp. 36–39, Jan. 2013.

[6]   D. Dai and S. He, "Proposal of a Coupled-Microring-Based Wavelength-Selective 1 x N Power Splitter," *Photonics Technol. Lett. IEEE*, vol. 21, no. 21, pp. 1630–1632, 2009.

[7]   H. Hanafusa, N. Takato, F. Hanawa, T. Oguchi, H. Suda, and Y. Ohmori, "Wavelength-insensitive 2 x 16 optical splitters developed using planar lightwave circuit technology," *Electron. Lett.*, vol. 28, no. 7, pp. 644–645, 1992.

[8]   S. H. Tao, Q. Fang, J. F. Song, M. B. Yu, G. Q. Lo, and D. L. Kwong, "Cascade wide-angle Y-junction 1×16 optical power splitter based on silicon wire waveguides on silicon-on-insulator," *Opt. Express*, vol. 16, no. 26, pp. 21456–21461, Dec. 2008.

[9]   M. Zirngibl, "Efficient 1x16 optical power splitter based on InP," *Electron. Lett.*, vol. 28, no. 13, pp. 1212–1213, 1992.

[10]   C. Dragone, I. P. Kaminow, C. H. Henry, and R. C. Kistler, "Efficient Multichannel Integrated Optics Star Coupler on Silicon," *IEEE Photonics Technol. Lett.*, vol. 1, no. 8, pp. 241–243, 1989.

[11]   D. Dai, Z. Wang, J. F. Bauters, M.-C. Tien, M. J. R. Heck, D. J. Blumenthal, and J. E. Bowers, "Low-loss Si_3N_4 arrayed-waveguide grating (de)multiplexer using nano-core optical waveguides," *Opt. Express*, vol. 19, no. 15, p. 14130, Jul. 2011.

[12]   M. J. R. Heck, A. La Porta, X. J. M. Leijtens, L. M. Augustin, T. de Vries, B. Smalbrugge, R. Notzel, R. Gaudino, D. J. Robbins, and M. K. Smit, "Monolithic AWG-based Discretely Tunable Laser Diode With NanosecondSwitching Speed," *IEEE Photonics Technol. Lett.*, vol. 21, no. 13, pp. 905–907, 2009.

[13]   G. Kurczveil and M. Heck, "An Integrated Hybrid Silicon Multiwavelength AWG Laser," *Sel. Top. …*, vol. 17, no. 6, pp. 1521–1527, 2011.

[14]   L. Zhuang, D. Marpaung, M. Burla, W. Beeker, A. Leinse, and C. Roeloffzen, "Low-loss, high-index-contrast Si_3N_4/SiO_2 optical waveguides for optical delay lines in microwave photonics signal processing.," *Opt. Express*, vol. 19, no. 23, pp. 23162–23170, Nov. 2011.

[15]   A. Leinse, R. G. Heideman, M. Hoekman, F. Schreuder, F. Falke, C. G. H. Roeloffzen, L. Zhuang, M. Burla, D. Marpaung, D. H. Geuzebroek, R. Dekker, E. J. Klein, P. W. L. van Dijk, and R. M. Oldenbeuving, "TriPleX waveguide platform: low-loss technology over a wide wavelength range," in *SPIE Microtechnologies*, 2013, p. 87670E–87670E–13.

[16]   D. T. Spencer, M. Heck, R. Moreira, J. T. Bovington, J. E. Bowers, A. Leinse, H. H. van den Vlekkert, R. G. Heideman, M. Hoekman, and T. T. Veenstra, "Integrated single and multi-layer Si_3N_4 platform for ultra-low loss propagation and small bending radii," in *Optical Fiber Communication Conference*, 2014, p. Th1A.2.

5   Low κ ULLW Gratings[8]

5.1   Introduction

The last resonant devices we will present are Si_3N_4 gratings. With the low loss and low index contrast to the cladding, the ULLW platform is capable of lower perturbation and longer length gratings than have previously been achieved on-chip. These are useful for future ultra-low noise lasers with sub-kHz lasing linewidths and RIN levels below -160 dB/Hz that require lower cavity losses to achieve a long effective cavity length and high mode selectivity [1]. First we will overview the theory behind the periodic perturbations of Bragg gratings, and derive some spectral qualities of importance. Then we will discuss our ULLW based grating design and results, while relating the results to important integrated laser applications and previous fiber based Bragg grating results.

5.2   Theory of Gratings

Gratings have periodic index perturbations that create a reflection spectrum. They have the advantage of operating at very low mode numbers, usually 1, and thus only have one resonance near the wavelength of interest. For identical forward and backwards propagation modes, the reflection occurs at the Bragg wavelength, λ_{Bragg}, when the period, Λ, of the grating is a half wavelength in the medium, $\lambda_{Bragg} = 2n_{eff}\Lambda$. Generally, for a given grating length, L_g, and reflection strength per period, κ, the reflection peak is given by the series of multiple small reflections:

$$R_{peak} = \tanh^2(\kappa L_g) \tag{5.1}$$

---

[8] *Much of the analysis and figures in this section have been reproduced from* [13].

and the bandwidth, $\Delta \nu$, of the resonance will decrease with κ as the reflection peak is kept constant by adding length. For a high reflection grating:

$$\Delta \nu = c\kappa / \pi n_{eff} \qquad (5.2)$$

However, a low loss waveguide is required to lengthen the grating, or else the perturbations furthest from the input will have a negligible effect. The main figure of merits are the bandwidth, $\Delta \lambda_{3dB}$, peak reflection, R_{peak}, and side mode suppression ratio, SMSR, as shown in Figure 5.1.
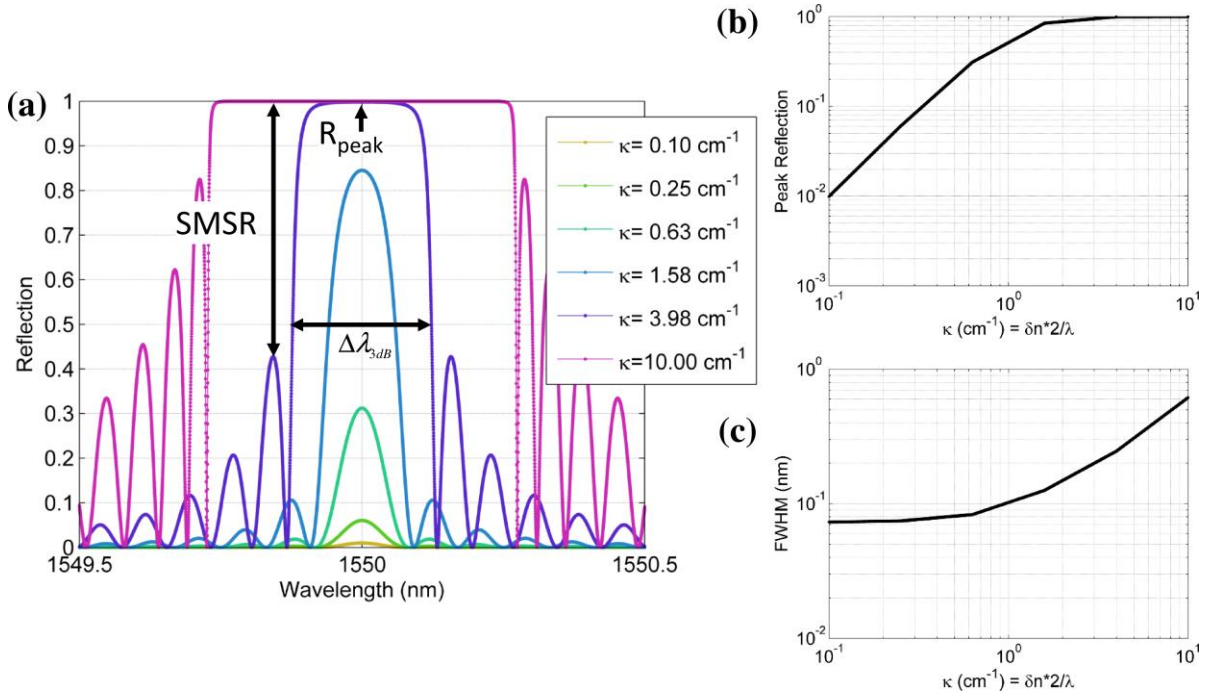
Figure 5.1) Uniform 1 cm long grating (a) reflection spectra, (b) peak reflection, and (c) FWHM for various κ values.

To model the grating, a T-matrix model is implemented as it can easily incorporate spurious facet reflections, controlled variation (apodization) of the grating strength, and loss or gain. Each matrix section can represent a single period or an appropriate sampling of a chirped grating. Assuming weakly guided modes, such as found in the ULLW platform, we translate each small reflection into an equivalent plane wave reflectivity using the difference

and summation of effective indices of the 2 regions, $\delta n = n_{eff1} - n_{eff2}$, and $\Sigma n = n_{eff2} + n_{eff1}$. Then

we define the reflectivity as:

$$r_{12} = -r_{21} = \frac{\delta n}{\Sigma n} \tag{5.3}$$

as shown in Figure 5.2.
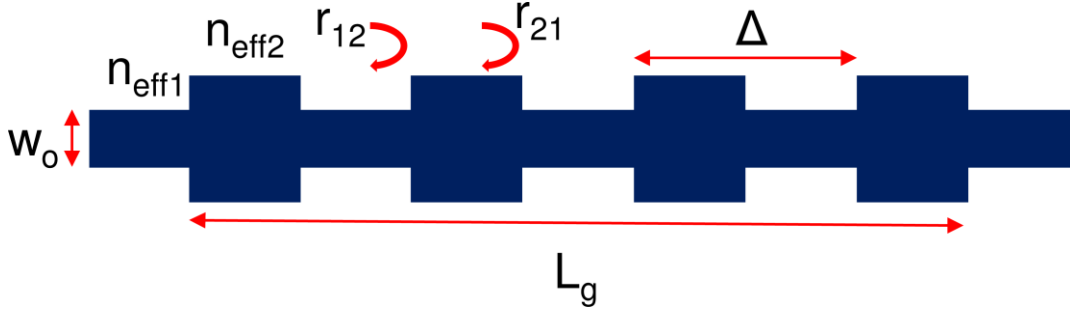
Figure 5.2) Schematic of a standard grating with 50% duty cycle, highlighting definitions used in the text.

This matrix approach is the so-called "Rouard's Method" [2], and coupled mode theory results can also be implemented in each matrix term [3]. The full matrix for a single grating section with two passive sections is given as:

$$\begin{bmatrix} a_1 \\ b_1 \end{bmatrix} = \begin{bmatrix} \dfrac{1}{\sqrt{1-r_{12}^2}} & \dfrac{r_{12}}{\sqrt{1-r_{12}^2}} \\[2mm] \dfrac{r_{12}}{\sqrt{1-r_{12}^2}} & \dfrac{1}{\sqrt{1-r_{12}^2}} \end{bmatrix} \begin{bmatrix} e^{j\tilde{\beta}L_2} & 0 \\ 0 & e^{-j\tilde{\beta}L_2} \end{bmatrix} \begin{bmatrix} \dfrac{1}{\sqrt{1-r_{12}^2}} & \dfrac{-r_{12}}{\sqrt{1-r_{12}^2}} \\[2mm] \dfrac{-r_{12}}{\sqrt{1-r_{12}^2}} & \dfrac{1}{\sqrt{1-r_{12}^2}} \end{bmatrix} \begin{bmatrix} e^{j\tilde{\beta}L_1} & 0 \\ 0 & e^{-j\tilde{\beta}L_1} \end{bmatrix} \begin{bmatrix} a_2 \\ b_2 \end{bmatrix}$$

$$\tag{5.4}$$

To relate the results to the more common metric κ, one must equate the net reflectivity from each half period to plane wave reflectivity to achieve:

$$\kappa = 2 * \delta n / \lambda_{Bragg} \tag{5.5}$$

This formula equates the two theories over the entire region of interest and will be used when we present the results in the next section.

56

Bragg gratings are important devices for reaching passive linewidths commensurate with >500k Q factors (sub-100 pm FWHM) while being readily integrated with a waveguide coupled gain element. Their single frequency nature and ability to be spatially sampled or apodized allows suppression of high order longitudinal modes in distributed Bragg reflector (DBR) and distributed feedback (DFB) lasers[4], [5]. Many integrated laser platforms have waveguide losses that have limited the grating lengths to less than a few mm, and higher index perturbations to the waveguide were necessary to increase the net reflection. With a ULLW, lower κ values can be utilized to lengthen the grating, thus reducing the linewidth to the performance level of fiber Bragg gratings[6] and lasers utilizing those gratings[7], [8]. These narrow bandwidths pave the way for sub-kHz lasing linewidths with monolithically integrated lasers, for instance, by coupling to Si/III-V active devices as previously demonstrated in the SOUL platform. Next, we demonstrate extremely low κ designs in three different waveguide perturbation geometries, and show κ values ranging from 0.23 cm^{-1} to 1.2 cm^{-1}. These results are useful for grating lengths up to 100 mm on the ULLW platform, and remain fully compatible with additional Si/III-V integration techniques. We also discuss the tradeoffs of these geometries in terms of lowest linewidth, apodization, and curved waveguide layouts.

5.3   Design of ULLW Gratings

A common way to implement weak κ gratings is by periodically varying the waveguide width[9], [10]. But this approach has limits when you need such a small κ due to lithography limits that can impose errors and broadening due to random fluctuations. Therefore, we investigate three different grating concepts with 8 versions each, shown in Figure 5.3a, termed "post", "sampled", and "high order", which are designed to produce

similar reflectivity over a fixed length of 7.8 mm by tailoring the gap (g), mode order (m), or waveguide width difference (Δw) from a nominal waveguide width (w_o)[11], [12]. We simulated a n_{eff} of 1.468 for the fundamental TE mode, yielding a period Δ of 528 nm at 1550 nm. The post gratings are designed to yield a low loss perturbation at the Bragg wavelength by placing a post of core material (250×264 nm) separated by g=0.8, 1.0, 1.2, 1.4, or 1.6 µm away from a w_o of 2.8 µm and 3.0 µm. The higher order gratings operate at the 3rd or 5th order, giving them a period of 5λ/2 or 3λ/2 to dilute the overall perturbation. The width of the waveguide is varied with a triangular or square shape, and the difference in width is Δw=0.2, 0.25, or 0.3 µm. The sampled gratings have a similar Δw, a fixed burst period (T) of 40.128 µm, and each burst contains N=4, 8, 11, or 15 teeth that act as symmetric sidewall gratings. The sampled gratings have a similar perturbation as [10], which demonstrated κ values between 13 cm^{-1} to 310 cm^{-1}, but dilute the κ by sampling the reflection across multiple peaks. To determine the gaps required of the post gratings, we used the FIMMWAVE mode solver software and the T-matrix method discussed previously to simulate perturbation levels on the order of $\Delta n_{eff} \approx 10^{-5}$, as required for κ values less than 1 cm^{-1}.
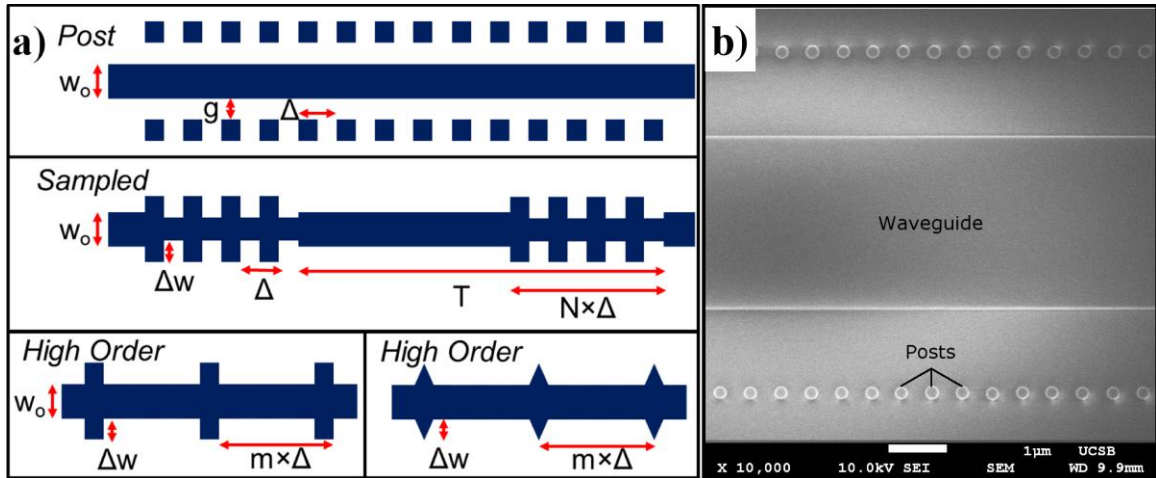
Figure 5.3) a) Layout and parameter definition of the grating geometries studied in this paper. w_o: nominal waveguide width, Δ: Bragg period, g: gap, Δw: waveguide width perturbation, T: sampling period, N: number of grating periods in one sample, and m: order of the grating. b) SEM of a completed post grating device. From [13] © 2015 OSA.

5.4   Waveguide Characterization

The grating structures were fabricated in-house by Michael Davenport and utilized the 90 nm sputtered cladding fabrication flow outlined in Chapter 2. An SEM of a completed post grating section is shown in Figure 5.3b, which shows a rounded profile due to etching, a measured period of 531 nm, and a post diameter of 227 nm. The completed devices were first tested for waveguide propagation loss with the OBR system on a 0.5 m Archimedean spiral test structure. Losses below 5 dB/m were achieved across the C+L bands, and <3.5 dB/m near 1550 nm. The grating spectra were then tested using an Agilent tunable laser, circulator, and 2 µm spot size lensed fiber. The input facet was angled at 15°, and the TE mode was excited by optimizing the reflected power. The facet loss was measured to be 0.85±0.1 dB/facet, and the TM mode did not show appreciable reflection from the gratings.
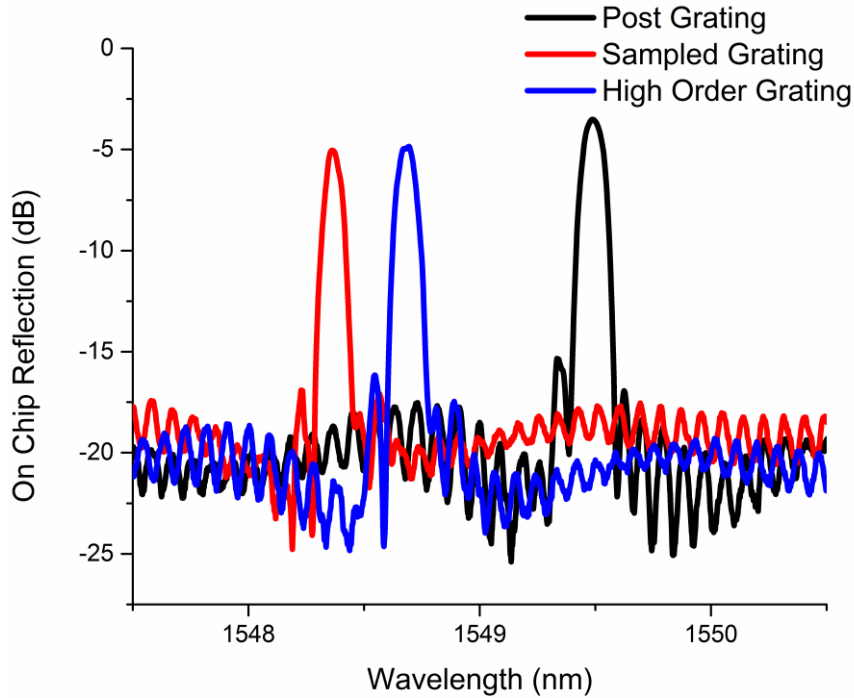
Figure 5.4) Comparison of spectra for the three grating geometries. Post grating: w_o=3.0 µm, g=0.8 µm; sampled grating: w_o=2.8 µm, N=11, Δw=0.25 µm; high order grating: w_o=2.8 µm, m=3, square shape, Δw=0.2 µm. From [13] © 2015 OSA.

5.5 *Uniform Gratings Results*

Figure 5.4 shows examples of reflection spectra from all three grating designs at similar peak reflection values. The spectra for all the grating geometries have similar features, which show fairly strong Fabry-Perot resonances from the facet reflection and finite return loss of the lensed fiber (-27 dB specification). Figure 5.5 shows the results of all 8 versions of the post gratings, in which the two groups correspond to the two different waveguide widths of 2.8 µm and 3.0 µm. With proper control of the gap and waveguide width, the grating reflection can be chirped or apodized in any fashion for future applications.

60
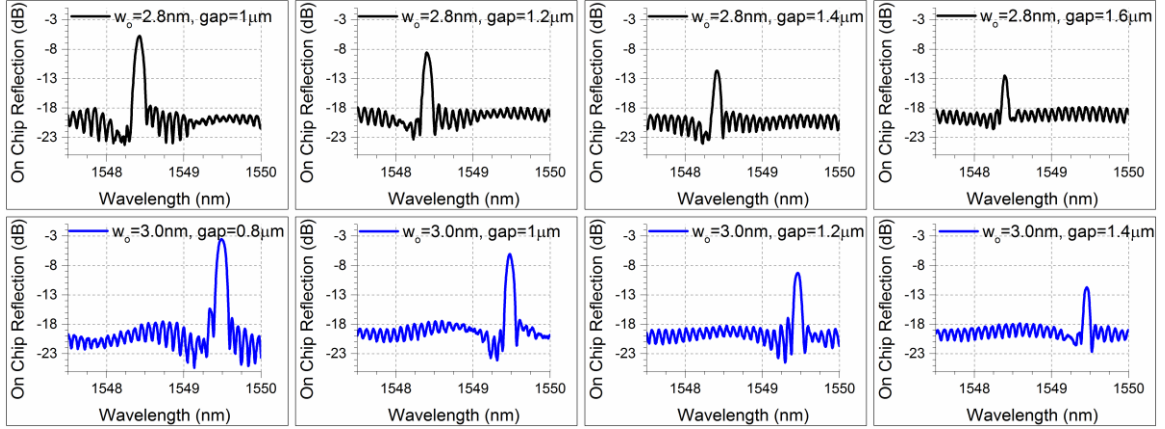
Figure 5.5) Post grating spectra vs. gap for two waveguide widths. From [13] © 2015 OSA.
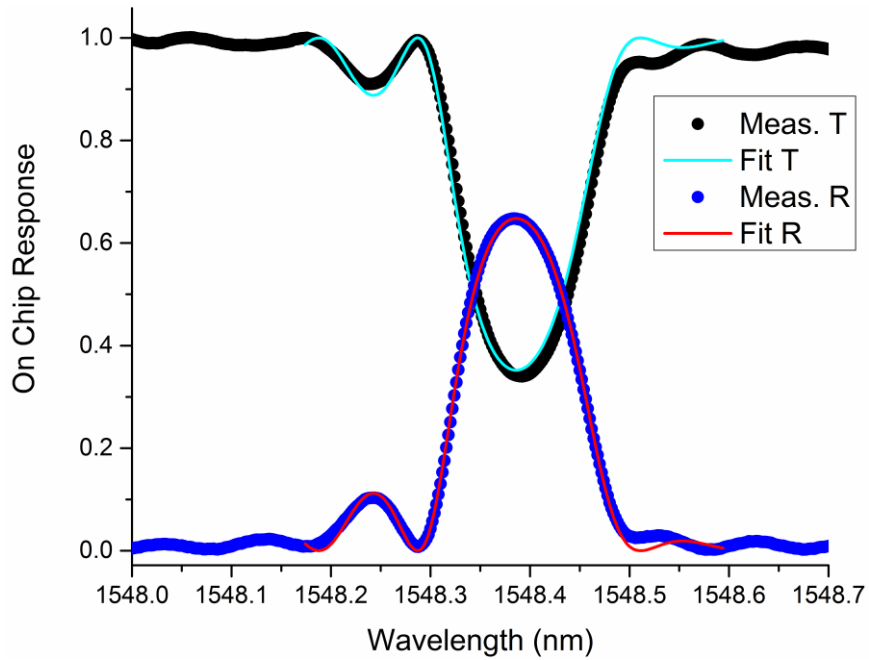
Figure 5.6) Results and fit of the reflection and transmission of a sampled grating device with 15 grating teeth/burst and Δw=0.25 μm. The asymmetries appear due to Fabry-Perot effects of the chip facets, and are accounted for in the matrix model of the gratings. From [13] © 2015 OSA.

We performed a nonlinear fit to match the n_{eff} and κ values of the gratings using the T matrix method outlined previously. To show the robustness of the fits, we perform the fits on the reflection of the device, and then use these parameters to overlap with the normalized transmission spectrum. One example of this is shown in Figure 5.6 for a sampled grating with 15 grating teeth/burst and Δw=0.25 μm. Due to the non-zero transmission at the grating

wavelength, the output facet reflection has a small effect on the grating spectrum, which is accounted for in the fitting. This Fabry-Perot effect causes a lower FWHM value than expected for a given κ value. The sum of transmission and reflection in the gratings show that the excess loss is less than our measurement uncertainty of 0.5 dB. While the T-matrix method is useful for fitting and future grating design based on experimental data, the effective index mode solver predicted approximately 50% weaker reflections. Matching the results to simulation would require a full FDTD simulation and further understanding of the exact amount of material refractive index change during the annealing steps.

Figure 5.7 and Table 5.1 summarize the main results of the different grating geometries, all of which achieved a κ value less than 1 cm^{-1}. It is important to note that achieving a low loss κ is the critical achievement, as higher reflection gratings for applications such as laser mirrors can be made by extending the grating length without adding appreciable propagation loss. There is a clear trend in κ and thus reflection versus gap in the post gratings and versus the number of teeth and waveguide width change Δw in the sampled gratings. The high order gratings with square perturbations also showed an increase in κ compared to triangular perturbations, due to the higher fill factor. However, the high order gratings were less controlled with waveguide width changes, possibly due to loss from coupling to radiation modes when the duty cycle is not well controlled [12]. The post gratings showed the lowest κ (0.28 cm^{-1}) and FWHM (74 pm) values, which is much improved compared to silicon-on-insulator waveguide results of κ =90 cm^{-1} (FWHM=1700 pm) [11] and 90 pm FWHM over 1 mm length [9]. Combined with their easier fabrication tolerance as discussed later, post gratings are the most attractive for laser mirrors and apodization profiles.
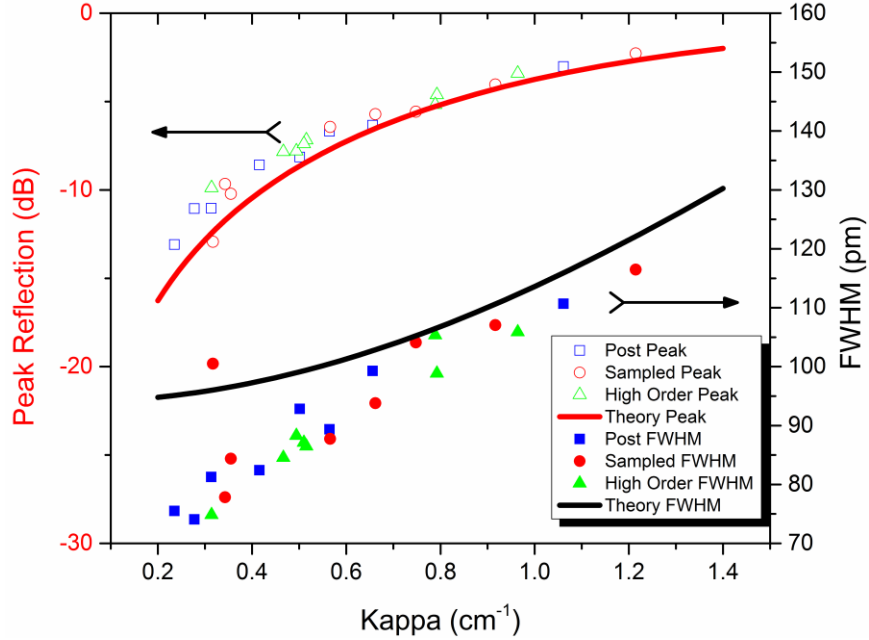
Figure 5.7) Overview of the peak reflection and FWHM vs. κ values for the 7.8 mm long Bragg gratings. The measured results show slightly higher reflection and lower FWHM than ideal linear gratings due to the small amount of facet reflection. From [13] © 2015 OSA.

Table 5.1) Results of the post, sampled, and high order gratings after removing system and facet coupling losses. From [13] © 2015 OSA.

	Post					Sampled					High Order				
w_o	g	κ (cm^{-1})	FWHM (pm)	Peak R (dB)	N	Δw	κ (cm^{-1})	FWHM (pm)	Peak R (dB)	Order, Shape	Δw	κ (cm^{-1})	FWHM (pm)	Peak R (dB)
2.8 μm	1.0 μm	0.66	99	-6.3	4	0.20 μm	0.32	101	-12.9	3, triangle	0.20 μm	0.47	85	-7.8
	1.2 μm	0.50	93	-8.1		0.25 μm	0.36	84	-10.2	3, square	0.20 μm	0.79	99	-4.6
	1.4 μm	0.31	81	-11.0	8	0.20 μm	0.34	78	-9.7	3, square	0.25 μm	0.96	106	-3.4
	1.6 μm	0.24	76	-13.1		0.25 μm	0.75	104	-5.6	3, square	0.30 μm	0.79	105	-5.2
3.0 μm	0.8 μm	1.06	111	-3.0	11	0.20 μm	0.57	88	-6.4	5, triangle	0.20 μm	0.31	75	-9.9
	1.0 μm	0.56	89	-6.7		0.25 μm	0.92	107	-4.0	5, square	0.20 μm	0.52	86	-7.2
	1.2 μm	0.42	82	-8.6	15	0.20 μm	0.66	94	-5.7	5, square	0.25 μm	0.49	88	-7.8
	1.4 μm	0.28	74	-11.1		0.25 μm	1.21	116	-2.3	5, square	0.30 μm	0.51	87	-7.4

5.6 λ/4-shifted Gratings

While low κ Bragg gratings operating in reflection mode are one of the ways to attain

narrow cavity linewidth, one can attain the same effect by using a high grating κ with a λ/4

shift operating in the transmission mode, where it would act as an integrated Fabry-Perot

equivalent. In this device, the perturbation used was similar to the sampled gratings, but with a higher Δw=1.2 µm over a 2 mm length. The measured on chip reflection and transmission spectra are shown in Figure 5.8. A similar T-matrix method was used to fit the data with an average n_{eff} of 1.5709 and a transmission floor due to a finite polarization extinction ratio of 17 dB. The larger perturbation yielded a κ of 30 cm^{-1}, and increased the propagation loss to 20 dB/m and device insertion loss to -2.5 dB in reflection and -1.1 dB in transmission. The measured FWHM is 7.6 pm (946 MHz), with a corresponding Q factor of 204 thousand.
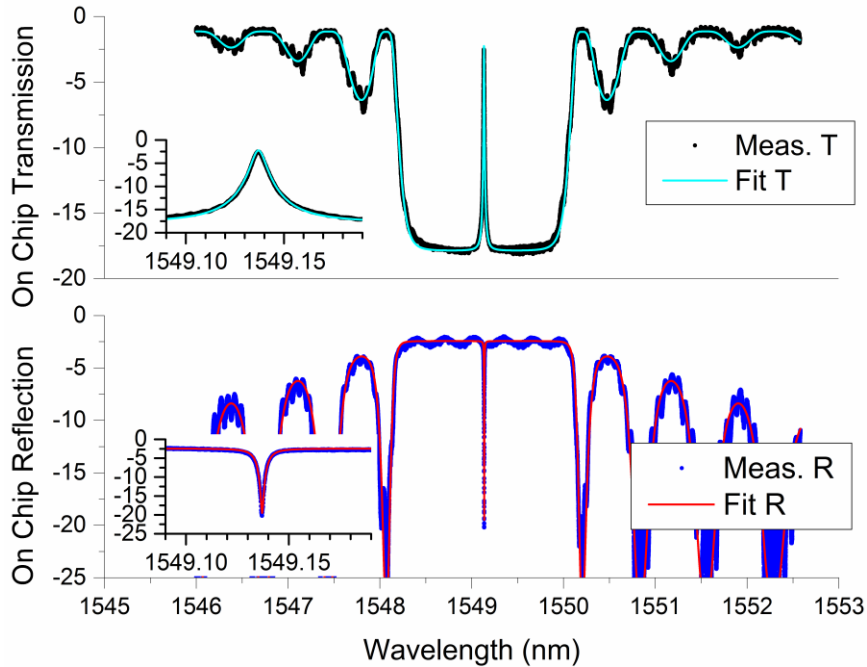
Figure 5.8) Results and fit of the reflection and transmission with identical parameters for a 2 mm long grating with a λ/4-shift in the center. The transmission floor in the experiment and theory is due to a finite polarization extinction ratio, which is fit to be 17 dB. From [13] © 2015 OSA.

5.7 *Discussion*

From a fabrication perspective, particularly lithography, the post grating can be advantageous for producing ultra-low κ gratings. Since the κ is well controlled by the space between the post and the waveguide, as demonstrated, very low κ can be attained without having to use a feature smaller than the 250 nm post. In principle, the κ in a post grating can

be as low as desired, as opposed to the sidewall grating used on the sampled and high order gratings, which will eventually become too small to resolve.

When implementing apodization functions that vary the κ versus length, the sidewall gratings can result in less than 100 nm features that are difficult to resolve in projection lithography systems, while the post gratings are only limited by the mask writing grid which defines the gap, typically less than 5 nm for the same systems. This is most beneficial in high side mode suppression laser design and thus low RIN performance. A tradeoff occurs if curved waveguides are required for longer delays in a more compact area, such as an Archimedean spiral. In this case the effective index and thus Bragg wavelength can vary with bending radius, and sidewall gratings may be preferable to post gratings due to their proximity to the center of the waveguide. High order gratings show the least promise, as they showed little trend with Δw perturbation.

These gratings have a thin 1.3 μm top cladding and can be readily integrated with Si waveguides and hybrid Si/III-V devices through multiple wafer bonds and substrate removal of SOI and InP epitaxial material, as demonstrated in the SOUL platform The narrow bandwidth nature of the gratings allows for >10 mm long laser cavities that are still high Q and single mode, while apodization can produce very high side mode suppression and low RIN levels. The Bragg wavelength will also shift with temperature when used with active devices, mainly due to the thermo-optic effect, which will change the index by 10^{-5}/°C, or ≈0.01 nm/° C[14].

5.8   *Summary of Chapter*

In this chapter, we have reviewed the motivation and theory behind Bragg gratings, and demonstrated low κ gratings for three geometries with narrow bandwidths ULLW platform.

The very low κ values ranged from 0.23 cm^{-1} to 1.2 cm^{-1}, with bandwidths of 74 pm to 116 pm. We have also demonstrated λ/4-shifted gratings with a Q$_{load}$ of 204 thousand, suitable for DFB style lasers. These gratings can be further utilized in apodization profiles, curved waveguides, or combinations such as sampled post gratings or high order post gratings. These gratings should find applications in narrow linewidth integrated lasers and narrow bandwidth filters, where the low index and ease of waveguide to waveguide coupling enables monolithic integration with Si/III-V active devices.

5.9   References

[1]   C. T. Santis, S. T. Steger, Y. Vilenchik, A. Vasilyev, and A. Yariv, "High-coherence semiconductor lasers based on integral high-Q resonators in hybrid Si/III-V platforms.," *Proc. Natl. Acad. Sci. U. S. A.*, vol. 111, no. 8, pp. 2879–2884, Feb. 2014.

[2]   L. A. Weller-Brophy and D. G. Hall, "Analysis of waveguide gratings: application of Rouard's method," *J. Opt. Soc. Am. A*, vol. 2, no. 6, pp. 863–871, Jun. 1985.

[3]   R. Kashyap, *Fiber Bragg Gratings*. Academic Press, 1999.

[4]   M. Okai, M. Suzuki, T. Taniwatari, and N. Chinone, "Corrugation-pitch-modulated distributed feedback lasers with ultranarrow spectral linewidth," *Jpn. J. Appl. Phys.*, vol. 33, no. 5A, pp. 2563–2570, May 1994.

[5]   L. A. Coldren, S. W. Corzine, and M. L. Masanovic, *Diode Lasers and Photonic Integrated Circuits*, 2nd ed. Hoboken, NJ: John Wiley & Sons, Inc., 2012.

[6]   M. Poulin, Y. Painchaud, M. Aubé, S. Ayotte, C. Latrasse, G. Brochu, F. Pelletier, M. Morin, M. Guy, and J.-F. Cliche, "Ultra-narrowband fiber Bragg gratings for laser linewidth reduction and RF filtering," in *Proc. of SPIE 7579*, 2010, p. 75791C.

[7]   P. A. Morton, V. Mizrahi, T. Tanbun-Ek, R. A. Logan, P. J. Lemaire, H. M. Presby, T. Erdogan, S. L. Woodward, J. E. Sipe, M. R. Phillips, A. M. Sergent, and K. W. Wecht, "Stable single mode hybrid laser with high power and narrow linewidth," *Appl. Phys. Lett.*, vol. 64, no. 20, pp. 2634–2636, May 1994.

[8]   W. Loh, F. J. O'Donnell, J. J. Plant, M. A. Brattain, L. J. Missaggia, and P. W. Juodawlkis, "Packaged, high-power, narrow-linewidth slab-coupled optical waveguide external cavity laser (SCOWECL)," *IEEE Photonics Technol. Lett.*, vol. 23, no. 14, pp. 974–976, Jul. 2011.

[9]   Z. Chen, J. Flueckiger, X. Wang, F. Zhang, H. Yun, Z. Lu, M. Caverley, Y. Wang, N. A. F. Jaeger, and L. Chrostowski, "Spiral Bragg grating waveguides for TM mode silicon photonics.," *Opt. Express*, vol. 23, no. 19, pp. 25295–25307, Sep. 2015.

[10]   M. Belt, J. Bovington, R. Moreira, J. F. Bauters, M. J. R. Heck, J. S. Barton, J. E. Bowers, and D. J. Blumenthal, "Sidewall gratings in ultra-low-loss Si$_3$N$_4$ planar waveguides.," *Opt. Express*, vol. 21, no. 1, pp. 1181–1181, Jan. 2013.

[11]   S. Zamek, D. T. H. Tan, M. Khajavikhan, M. Ayache, M. P. Nezhad, and Y. Fainman,

"Compact chip-scale filter based on curved waveguide Bragg gratings.," *Opt. Lett.*, vol. 35, no. 20, pp. 3477–3479, 2010.

[12] A. Hardy, D. F. Welch, and W. Streifer, "Analysis of second-order gratings," *IEEE J. Quantum Electron.*, vol. 25, no. 10, pp. 2096–2105, 1989.

[13] D. T. Spencer, M. Davenport, S. Srinivasan, J. Khurgin, P. A. Morton, and J. E. Bowers, "Low kappa, narrow bandwidth Si_3N_4 Bragg gratings," *Opt. Express*, vol. 23, no. 23, p. 30329, Nov. 2015.

[14] M. Belt and D. J. Blumenthal, "High temperature operation of an integrated erbium-doped DBR laser on an ultra-low-loss Si_3N_4 platform," in *Optical Fiber Communication Conference*, 2015, p. Tu2C.7.

6 Narrow Linewidth Integrated Lasers with Ultra-high Q Feedback[9]

In this chapter, we will implement an ultra-high Q resonator and heterogeneous Si/III-V laser in a laser frequency stabilization scheme known as Pound-Drever-Hall (PDH) locking [1]. This system is used by the most stable laser locking systems to date, which reduces the frequency noise of a tunable laser via an RF lock to a reference resonator. A requirement of PDH modulation is a very high Q, such that the modulator speed is much greater than the FWHM. This requirement has typically been satisfied using free space coupled resonators with ultra-low expansion glass and placed in a vacuum chamber for thermal stability [2]. Our work bridges this gap by utilizing 30 million Q factor ULLW resonators that can sustain PDH locking [3], and narrow (160 kHz Lorentzian) linewidth heterogeneous Si/III-V lasers [4]. We will show a system demonstration of the noise suppression capability using these integrable devices, yielding up to 33 dB reduction in FM PSD at a few kHz offset frequencies. This result can be extended to realize a fully integrated stable narrow linewidth laser source on a single chip which can provide large improvements in consumed power and cost.

6.1 The PDH System & Components

The PDH system is a laser frequency stabilization scheme that requires RF phase modulation of a tunable laser beyond the full width half maximum (FWHM) of the reference high Q resonator. The resonator acts as a frequency discriminator and performs the FM to AM conversion, more efficiently in the through port (notch filter) configuration than the drop port due to higher carrier suppression and sideband recovery outside the bandwidth [5].

---

[9] *Much of the analysis and figures of this section have been reproduced from* [12].

The optical signal is then detected on a high speed photodetector (PD) and transimpedance amplifier (TIA). This RF signal is demodulated on a mixer with the same signal generator driving the laser modulation to yield the discriminator constant, D_v (V/Hz). The baseband error signal contains information on the difference between the laser frequency and resonance frequency from DC to the modulation frequency. This error signal is then filtered with op-amps and has a transfer function of G (V/V). Finally the signal is fed back to the DC portion of the laser's current injection pads in negative feedback, with an actuator constant of K (Hz/V). A block diagram is shown in Figure 6.1 [6].
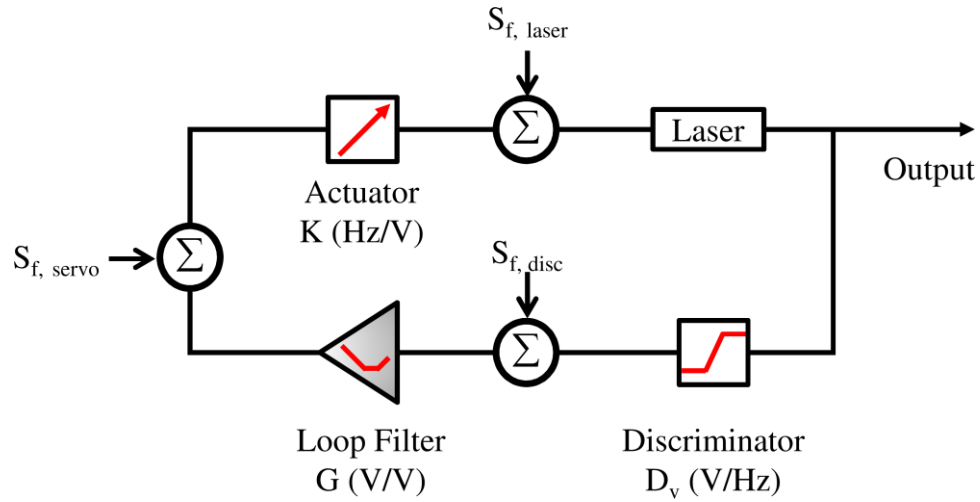
Figure 6.1) Block diagram of the PDH frequency locked loop with added noise sources.

The closed loop laser FM PSD, $S_{v,cl}$, is calculated with amplitude values S_f (Hz/√Hz) of the free running laser, and added amplitude noise of the op-amp servos and discriminator detection scheme:

$$\sqrt{S_{v,cl}} = S_{f,cl} = \frac{\sqrt{S_{f,laser}^2 + \left|KS_{f,servo}\right|^2 + \left|KGS_{f,disc}\right|^2}}{\left|1 + KGD_v\right|} \tag{6.1}$$

For negligible servo noise and discriminator noise, i.e. high Q resonator and high optical powers, the closed loop FM PSD becomes:

69

$$\sqrt{S_{v,cl}} = S_{f,cl} = \frac{S_{f,laser}}{\left|1 + KGD_v\right|} \tag{6.2}$$

As we move to very high servo gain (G large), the ultimate limit of the system becomes entirely dependent on the discriminator slope, thus the importance of a high Q factor resonator to achieve best performance:

$$\sqrt{S_{v,cl}} = S_{f,cl} = \frac{S_{f,disc}}{D_v} \tag{6.3}$$

For our experiment, the system schematic is shown in Figure 6.2, and a photograph of the lab setup is shown in Figure 6.3. We will go over the components in the next section.
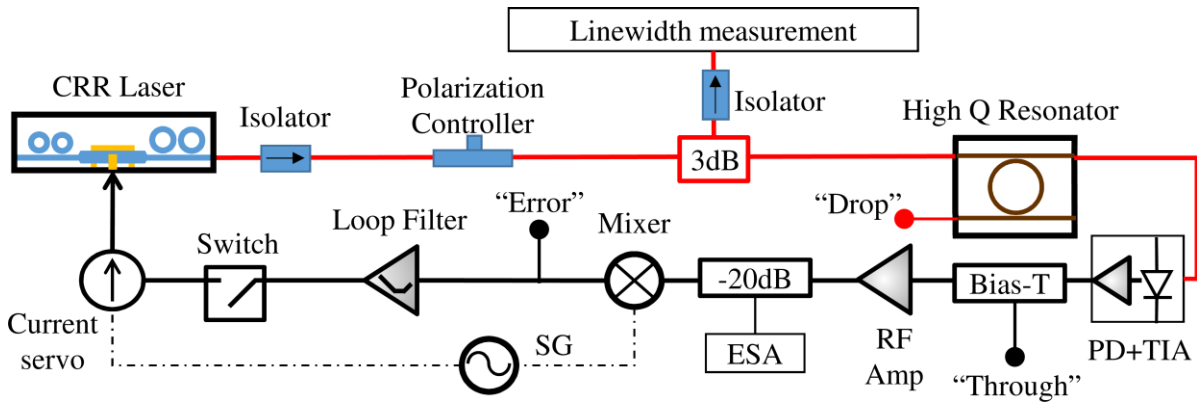
Figure 6.2) Schematic of the PDH setup. The coupled ring resonator (CRR) laser is isolated from any spurious reflections and the resonator is packaged with cleaved fiber. Optical fibers are shown in red, with electronic signals shown in black. The black and red bubbles denote monitor points in the system.
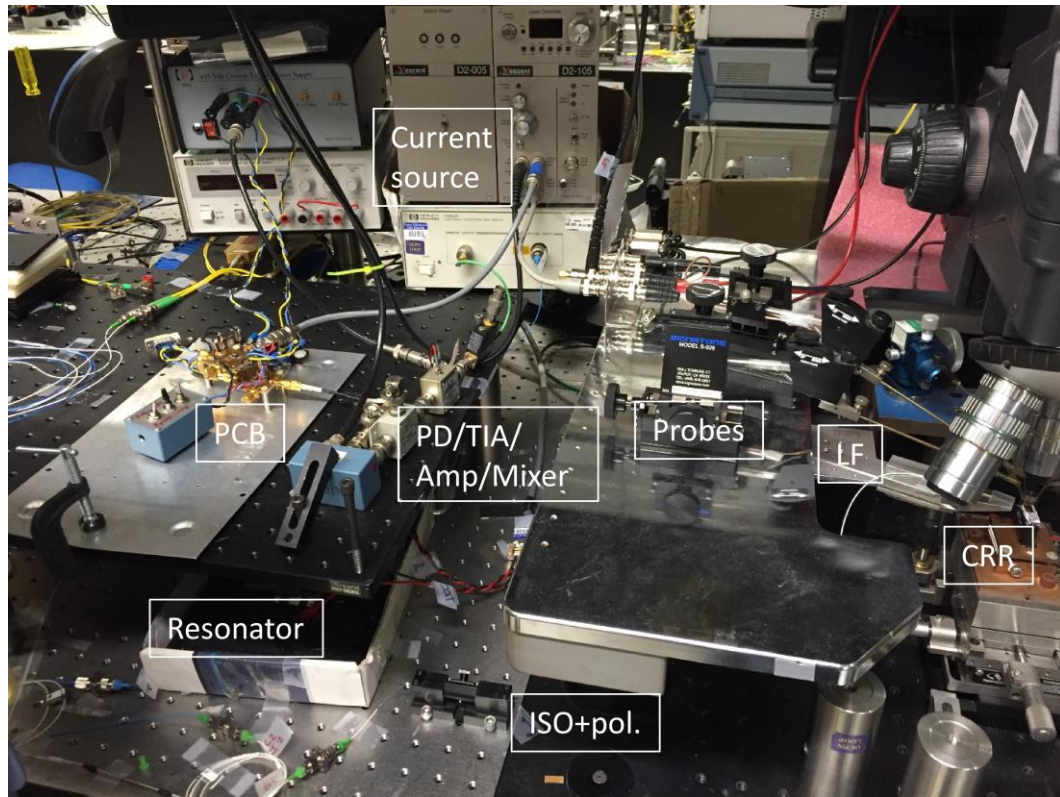
Figure 6.3) Photograph of the PDH setup in lab, CRR: coupled ring resonator laser, LF: lensed fiber, ISO+pol.: isolator + polarization controller, PCB: printed circuit board electronics.

6.1.1 The Heterogeneous Si/III-V CRR Laser

The laser has $7\times$ InGaAs/InGaAlAs quantum well gain material heterogeneously integrated with Si waveguide based CRR mirrors via wafer bonding [4]. Each mirror contains 2 resonators that are appropriately coupled and fabricated with micro-heaters to produce a high Q tunable Vernier in conjunction with the opposite mirror. The lasing wavelength for this study was 1577 nm, and the linewidth was 160 kHz measured via the self-heterodyne method. Photographs of the CRR laser are shown in Figure 6.4.
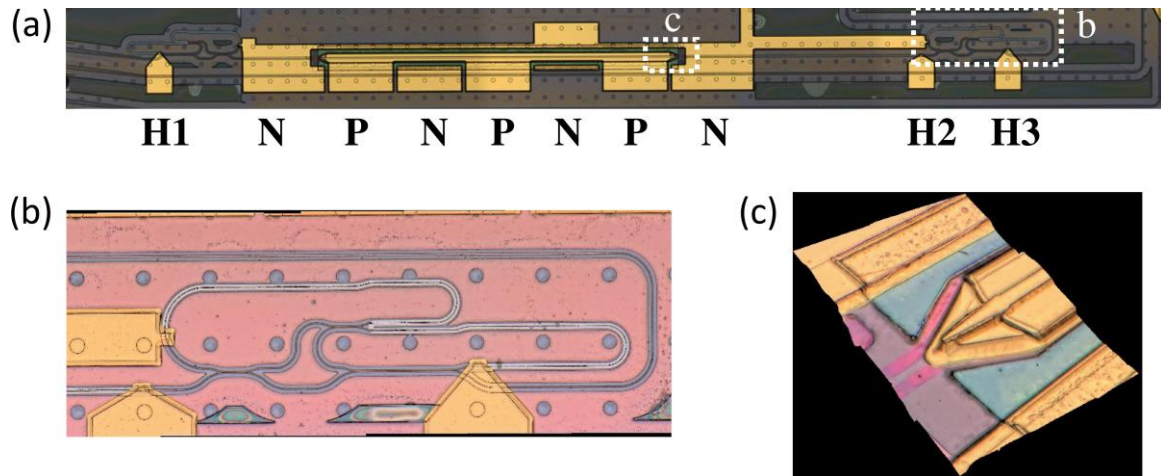
Figure 6.4) (a) Top down photograph of the full CRR device, with P, N, and Heater pads labeled. (b) A single CRR mirror containing two path length matched Si resonators. (c) 3D photograph of the InP mesa taper region.

The current bias, RF frequency drive, and feedback signal are combined in a Vescent D2-105 current servo and probed to the CRR chip on a TEC stage. The laser's output is coupled with a 2 µm spot size lensed fiber, and spliced to an inline fiber isolator and polarization controller to control the polarization launched into the ring resonator. The laser's FM modulation frequency characteristics are measured by low frequency locking a 10 cm unbalanced Mach-Zehnder interferometer (MZI) at both quadrature slopes, while performing a network analyzer test [7] with a SRS 770 (500 Hz – 100 kHz) and HP 4396B (100 kHz – 20 MHz), shown in Figure 6.5. The laser shows a single pole role off at 70 kHz and resonant peaking at 7.6 MHz. The residual amplitude modulation is a minimum of 12 dB lower than the frequency tuning of the laser at 1 MHz. The electrical response of the Vescent servo is also shown in Figure 6.5, with a DC response of 1 mA/V and usable bandwidth of 1 MHz before additional phase lag is added.
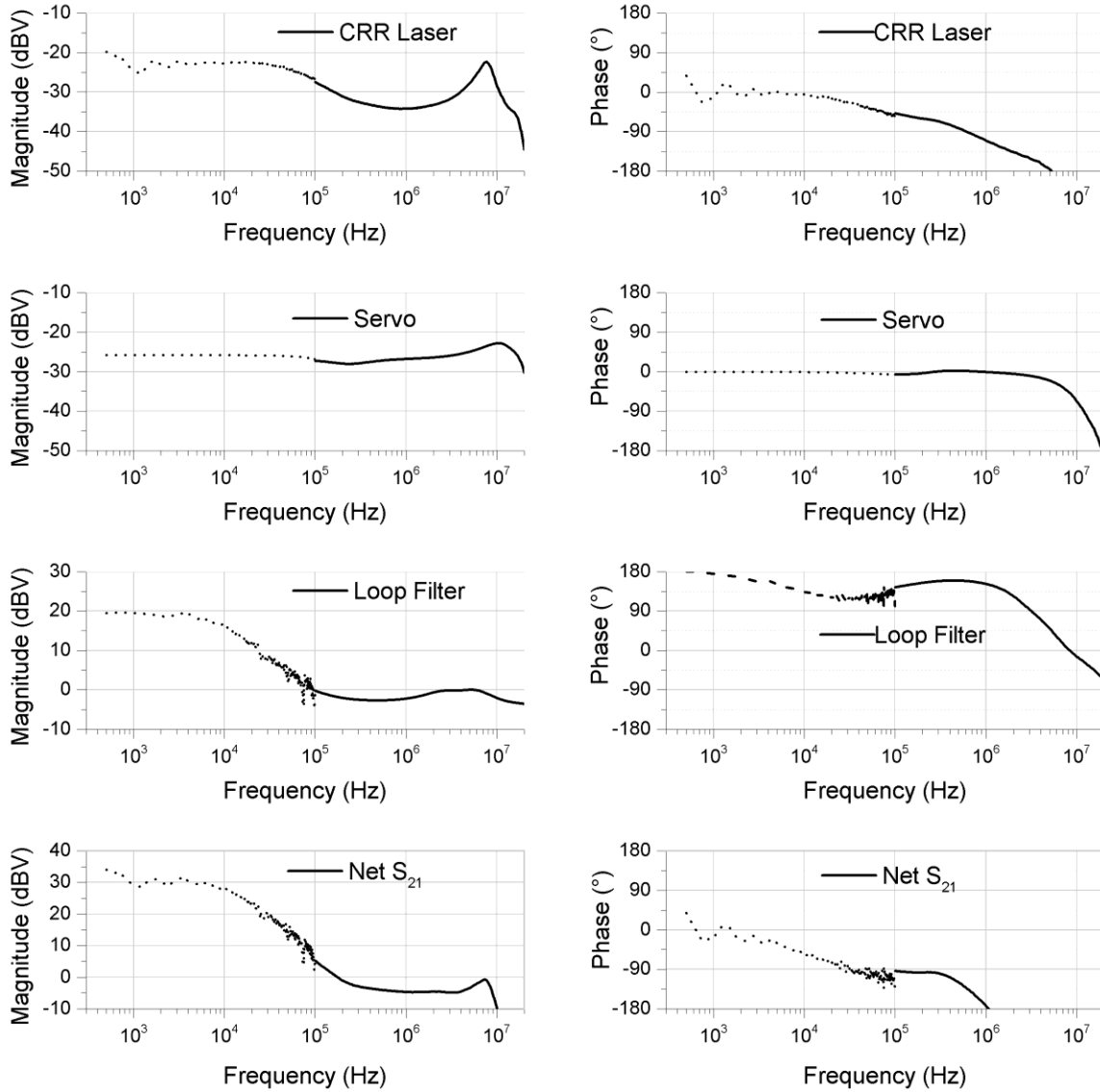
Figure 6.5) Bode plots of the CRR laser FM tuning, Vescent servo supply, loop filter electronics, and total transfer function of the feedback loop used in this study. Dotted lines correspond to measurements using a SRS 770 (500 Hz – 100 kHz), and solid lines using a HP 4396B (100 kHz – 20 MHz).

6.1.2 The ULLW Resonator

For the PDH work, we use a bend radius of 9.8 mm and core thickness of 40 nm Si_3N_4 with bonded thermal SiO_2 cladding and high temperature anneal, but stay in the single mode regime with a waveguide width of 7 μm for system simplicity. This yields a Q_{load} of 30 million and extinction ratio of 3.5 dB at the operating wavelength of 1577 nm. The

73

resonator has been packaged in an Al case with cleaved fiber, transparent epoxy, and a TEC for slow macro alignment. A picture of the packaged resonator is shown in Figure 6.6.
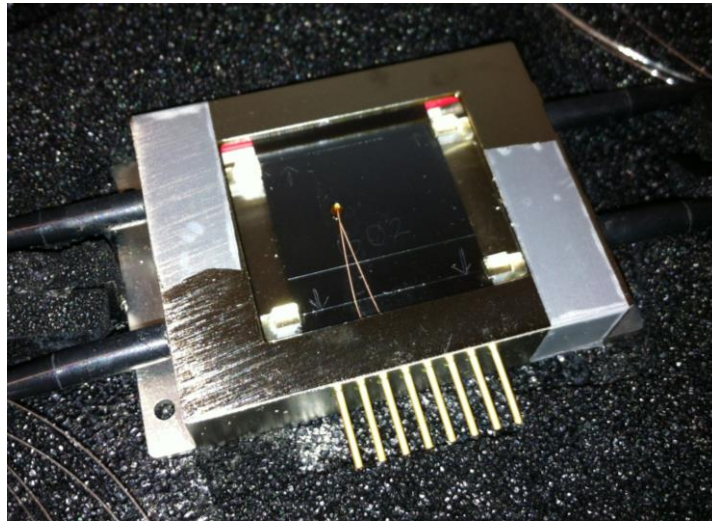
Figure 6.6) Photograph of the packaged ULLW ring resonator used for PDH locking.

6.1.3   Electronic Demodulation and Filtered Feedback

The PDH electronics are implemented with commercial components in close proximity to the other components to reduce phase lag due to excess delay. The PD+TIA is an Agilent 11982A with 15 GHz bandwidth, and a bias-T is used to monitor the through port DC signal. A broadband RF amplifier increases the RF signal before reaching a -20 dB monitor tap and ZAD-1+ double balanced mixer. The loop filter is implemented with OP27 and AD797 op-amps that are soldered onto evaluation boards, as shown in Figure 6.7. A maximum driving capacitance of 1 nF is used to place a low frequency integrator pole at 8 kHz, and a differential gain for compensating the laser roll off is placed at 70 kHz. The frequency response of the loop filter is shown in Figure 6.5, and a good reference for design is given in [8].
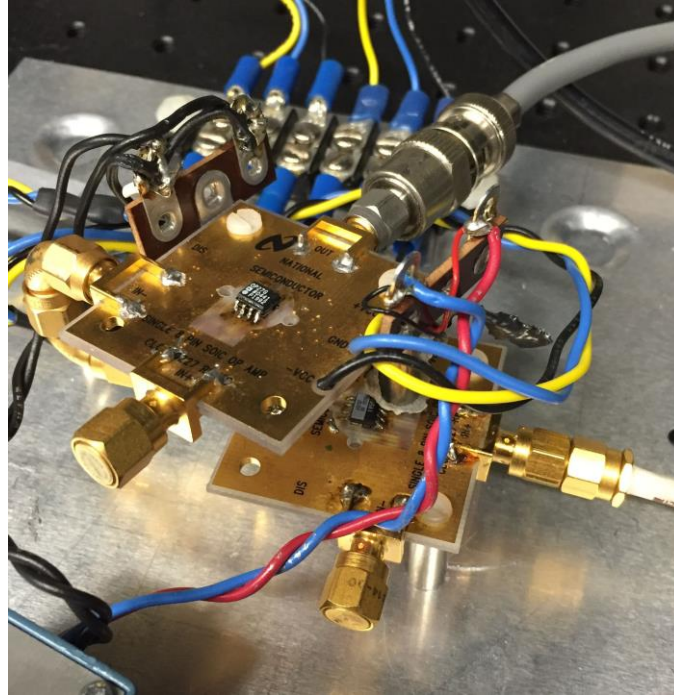
Figure 6.7) Photograph of the PCB electronics.
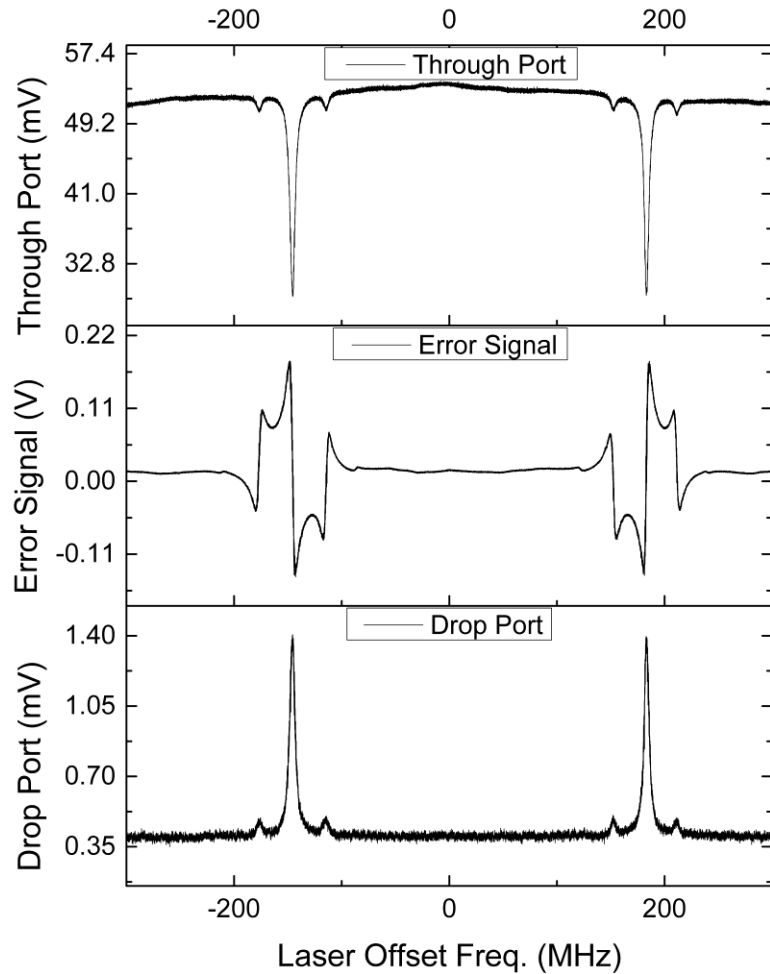
Figure 6.8) Open loop calibration of the through port, error signal, and drop port with a ramp signal applied to the laser servo.

6.2   PDH System Results

The open loop response of the system is measured by removing the loop filter, applying a 25 Hz, 3 Vpp ramp and a 30 MHz RF sinusoid to the laser servo, and monitoring the 3 labeled points shown in Figure 6.2 on an oscilloscope. The results are shown in Figure 6.8, where the through port is monitored via a bias-T, the error signal is taken through an in-line electrical splitter after the mixer, and the drop port is measured on a Thorlabs DET 01CFC photodetector. Using the 30 MHz sidebands as the reference, the laser FM efficiency is 201 MHz/V, and the error signal slope is 86 mV/MHz, yielding a transfer function of

17 V/V near DC. With the DC response and frequency characteristics of the loop, we then lock the laser to the resonance wavelength by connecting the loop filter electronics and a variable electronic attenuator, up to 10 dB to achieve stability.

To properly characterize the system performance, we utilize two signals in the PDH system. The first is an absolute measurement on the laser's FM PSD by taking a 3 dB optical tap after the laser output to an isolator, 13 m unbalanced fiber based MZI and PD+TIA. The interferometer contains a fiber stretcher in one arm, and the PD has a monitor tap, which we use to apply a low frequency quadrature or peak locking circuit to measure the FM and AM response, respectively. Once the MZI is locked, the PD+TIA output put goes through a DC block (2 Hz - 40 MHz) and the noise PSD is measured across different spans of a Rhode and Schwarz FSU spectrum analyzer with RMS filters and corrected to the appropriate units of Hz^2/Hz. The RF loss and calibrated transfer function of the MZI are subtracted from the result to yield the laser's FM PSD [7].

The unlocked laser's high frequency FM PSD (S_ν) is measured to be 60×10^3 Hz^2/Hz, which aligns perfectly with the previously measured 160 kHz linewidth ($\Delta\nu$) by self-heterodyne method ($\Delta\nu = \pi S_\nu$ for Lorentzian lineshapes) [4]. This high frequency noise is $\approx 15\times$ better than conventional InP DFB lasers, however, at low frequency, there is considerable walk off and the PSD increases as $1/\sqrt{f}$ yielding an unstable laser at microsecond and greater time scales. The locked PDH system suppresses this noise considerably beginning at 200 kHz, and reduces the noise to 10^3 Hz^2/Hz at 3 kHz offset frequency, a reduction of 33 dB compared to the unlocked laser. A common phase bump is seen at 1 MHz, and effects of the laser's FM response appear near 4 MHz. The measured AM noise shows that further FM noise reduction is limited by this floor, since the laser servo

is unable to further distinguish laser FM noise from AM system noise. Next, we will investigate the source of this noise limit.
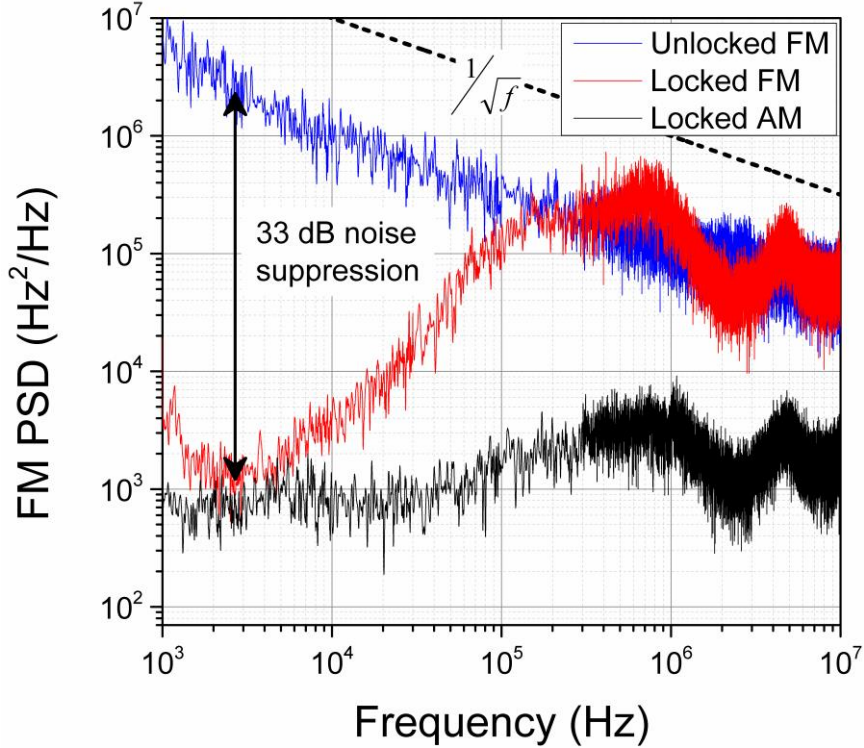
Figure 6.9) PSD of the PDH system measured through an unbalanced MZI. At quadrature, the unlocked (blue) and locked (red) FM PSD is given, while the locked AM PSD (black) is measured at the peak of the MZI.

The second measurement used to characterize the system is the 30 MHz RF signal in the feedback circuit. Since this is made inside the feedback loop, the exact noise levels are only good for relative comparison, not absolute measurement. The effect of the locked feedback circuit on the laser's FM noise is written onto the 30 MHz signal, and shows the same phase bump near 1 MHz, and reduction at frequencies less than 200 kHz. The limit of this reduction is found by measuring the shot noise plus laser relative intensity noise (RIN) floor, which is obtained by bypassing the resonator and matching the photocurrent level of the locked system, in this case the dip of the through port. The thermal noise floor is measured with the laser off and amplifiers on, and found to be >8 dB below the shot noise plus RIN

floor. The minimum locked noise level is found to be within a few dB of system noise floor, as shown in Figure 6.10.
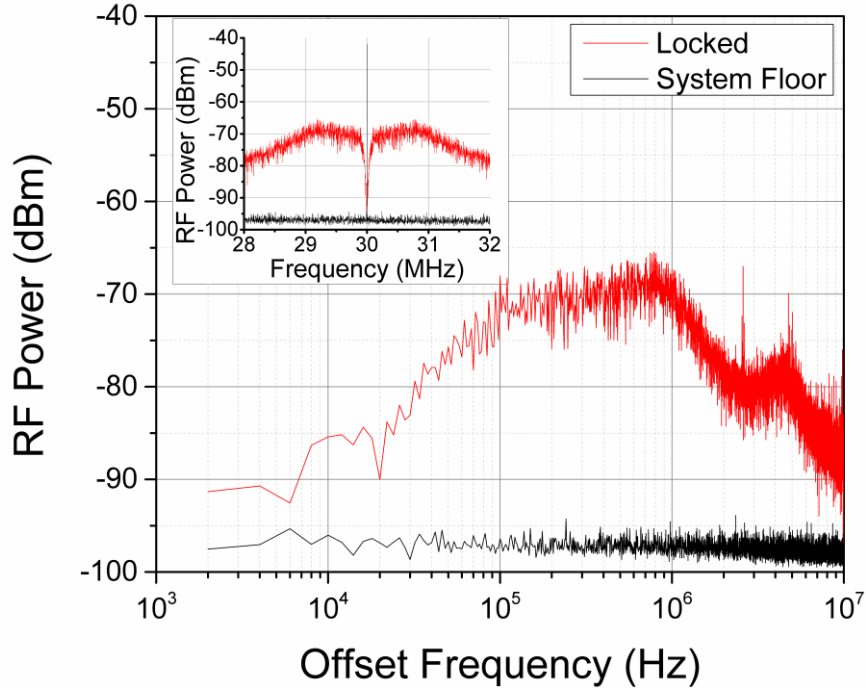
Figure 6.10) In-loop characterization of the 30 MHz RF signal in linear (inset) and log scale.

6.3   Discussion and Improvements

Now we will examine the system performance compared to the expected noise suppression from loop measurements, utilizing Equation (6.2). We use the free running laser linewidth and net loop S_{21} measurement of Figure 6.5 to compare the measured results, shown in Figure 6.11. The expected result is very near the measured result in the 10-100 kHz, but does not align near the unity gain bandwidth. This is most likely due to spurious phase bumps appearing in the locked system as additional phase lag is encountered in the 100 kHz-1 MHz range.

Figure 6.11) Expected result (black) from Net S$_{21}$ measurement and free running laser FM PSD (blue), compared to measured result (red).

Next, we will plot the expected laser FM PSD assuming a few improvements to the system. First, the loop could be made with more efficient chip-to-fiber coupling or monolithic waveguide-to-waveguide coupling [9]. This could yield a lower shot noise floor by an estimated 15 dB (9 dB facet loss versus 1.6 dB monolithic), where we would then be limited by thermal noise giving us a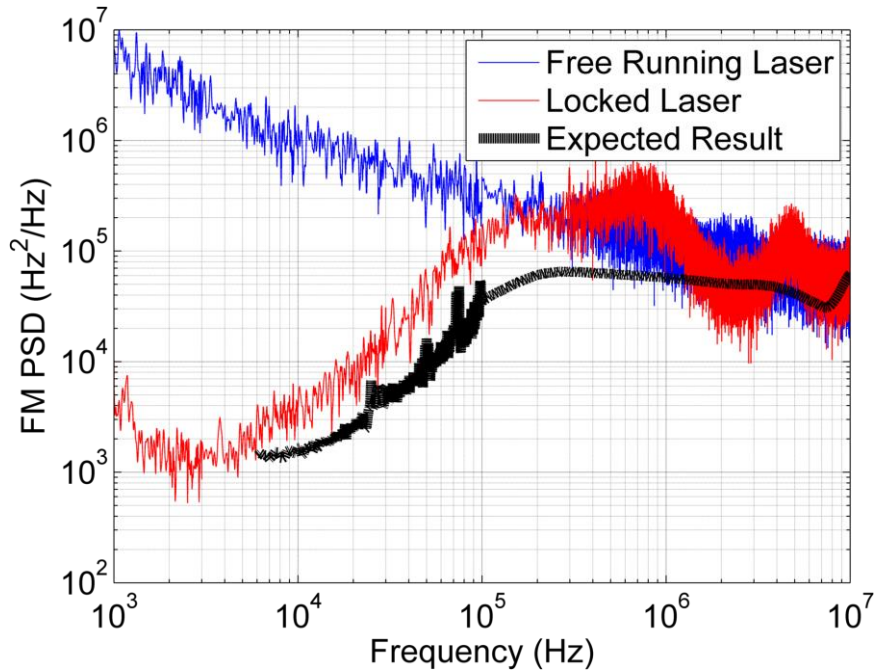n 8 dB improvement. With higher power, D$_v$ increases accordingly, and we need less loop gain. The improvement increases to 11 dB by removing the 10 dB electrical attenuator so we wouldn't require one of the broadband amplifiers, thus eliminating it's noise figure (NF) (ZFL-500LN: 24 dB gain, 3 dB NF). Currently, 11 dB would be the maximum noise floor improvement we would envision, as residual laser AM would appear at levels of -12 dB of the FM efficiency, although this may be improved with a high ER critically coupled resonator that suppresses residual AM at the carrier. In terms of frequency response, the resonator creates a pole at the FWHM, and the CRR laser cavity yields a nonlinear FM tuning response beyond the loop bandwidth of 200 kHz, most likely

due to the combination of thermal and carrier plasma effects. Programmable digital loop filters can design for these nonlinear effects and closer monolithic or system-in-package integration of the full optoelectronic loop [9]–[11] will keep the phase lag due to loop delay low. With such systems, a fully compensated integrator servo could be envisioned (f^{-2} slope) out to a bandwidth of 1 MHz, after which laser parasitics become a problem. Figure 6.12 shows the theoretical reduction in laser FM noise to 65 Hz^2/Hz, assuming an 11 dB improvement in noise floor, and a -20 dB/decade compensated loop filter out to 1 MHz unity gain bandwidth. The free running laser data is multiplied by the filter transfer function and Gaussian noise was numerically added for the floor. These improvements would produce an integrated linewidth close to 100 Hz.
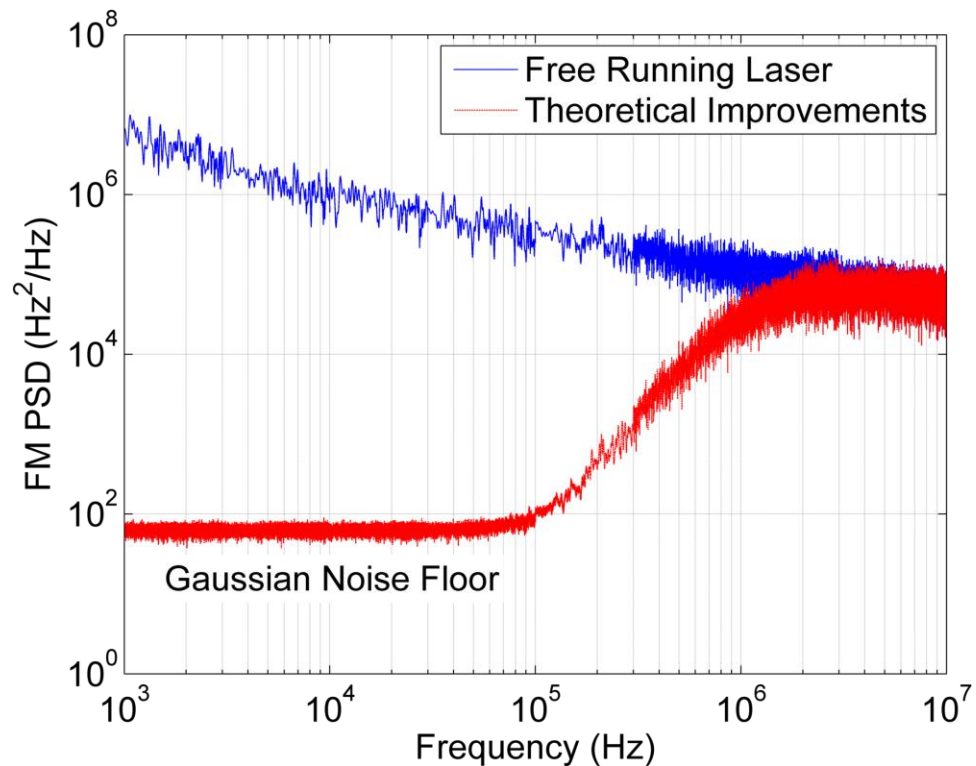

Figure 6.12) Theoretical reduction of the laser FM PSD with improved PDH metrics of improved laser power and loop filter bandwidth of 1 MHz.

6.4   Summary of Chapter

In this chapter, we have presented a PDH frequency stabilization system using a heterogeneous Si/III-V CRR laser, waveguide coupled Si_3N_4 resonator, and appropriate feedback electronics. The high frequency FM noise is measured to be 60×10^3 Hz^2/Hz consistent with a 160 kHz linewidth. Within the loop bandwidth of the PDH lock, the low frequency noise is suppressed up to 33 dB, to 10^3 Hz^2/Hz. The ultra-high Q Si_3N_4 cavity allows for 60× reduction of noise below the spontaneous emission noise of the laser, making it very promising for further integration work. Lower coupling losses on a monolithic platform will improve the system performance, and programmable electronics in closer proximity to the devices will allow for higher loop bandwidths and noise suppression. To reduce noise even further, higher power lasers and higher Q factor resonators will increase the discriminator constant and reduce the shot noise limited noise floor.

6.5   References

[1]   E. D. Black, "An introduction to Pound–Drever–Hall laser frequency stabilization," *Am. J. Phys.*, vol. 69, no. 1, pp. 79–87, 2001.

[2]   W. Zhang, M. J. Martin, C. Benko, J. L. Hall, J. Ye, C. Hagemann, T. Legero, U. Sterr, F. Riehle, G. D. Cole, and M. Aspelmeyer, "Reduction of residual amplitude modulation to 1×10^-6 for frequency modulation and laser stabilization," *Opt. Lett.*, vol. 39, no. 7, pp. 1980–1983, Mar. 2014.

[3]   D. T. Spencer, J. F. Bauters, M. J. R. Heck, and J. E. Bowers, "Integrated waveguide coupled Si_3N_4 resonators in the ultrahigh-Q regime," *Optica*, vol. 1, no. 3, pp. 153–157, Sep. 2014.

[4]   S. Srinivasan, M. Davenport, T. Komljenovic, J. Hulme, D. T. Spencer, and J. E. Bowers, "Coupled-Ring-Resonator-Mirror-Based Heterogeneous III–V Silicon Tunable Laser," *IEEE Photonics J.*, vol. 7, no. 3, p. 2700908, Jun. 2015.

[5]   N. M. Sampas, "A ring laser gyroscope with optical subtraction," 1990.

[6]   T. Day, "Frequency stabilized lasers for coherent optical communications," 1990.

[7]   D. M. Baney and W. V. Sorin, "High Resolution Optical Frequency Analysis," in *Fiber Optic Test and Measurement*, D. Derickson, Ed. New Jersey: Prentice Hall, Inc., 1998.

[8]   R. Fox, C. Oates, and L. Hollberg, "Stabilizing diode lasers to high-finesse cavities," in *Experimental Methods in the Physical Sciences: Cavity-Enhanced Spectroscopies*, R. D. van Zee and J. P. Looney, Eds. Academic Press, 2003.

[9]   M. J. R. Heck, J. F. Bauters, M. L. Davenport, D. T. Spencer, and J. E. Bowers, "Ultra-low loss waveguide platform and its integration with silicon photonics," *Laser Photon. Rev.*, vol. 8, no. 5, pp. 667–686, Sep. 2014.

[10]   A. Sivananthan, H. Park, M. Lu, J. S. Parker, E. Bloch, L. A. Johansson, M. J. Rodwell, and L. A. Coldren, "Monolithic Linewidth Narrowing of a Tunable SG-DBR Laser," in *Optical Fiber Communication Conference/National Fiber Optic Engineers Conference 2013*, 2013, p. OTh3I.3.

[11]   L. Chen, A. Sohdi, J. E. Bowers, L. Theogarajan, J. Roth, and G. Fish, "Electronic and photonic integrated circuits for fast data center optical circuit switches," *IEEE Communications Magazine*, vol. 51, no. 9, pp. 53–59, 2013.

[12]   D. T. Spencer, M. L. Davenport, T. Komljenovic, S. Srinivasan, and J. E. Bowers, "Stabilization of heterogeneous silicon lasers using Pound-Drever-Hall locking to Si$_3$N$_4$ ring resonators," submitted to Optics Express, 2016.

7   Conclusion

7.1   Summary of Thesis

In this thesis, we have overviewed the ULLW platform and how it can greatly benefit resonant structures and integrated laser systems. Beginning with single mode ring resonators with standard directional couplers, we found that appreciable loss is added when the propagation loss is very low. This has led us to design weakly tapered pulley couplers on multimode waveguide widths, and we have reported record high Q factors of 81 million. Further work on directional coupler design and reaching the limits of the ULLW platform could produce Q_{int} factors of 500 million.

The low loss and controllable coupling of the ULLW platform has helped us demonstrate a novel 1×16 resonant splitter with excess coupling loss of 0.9 dB and maximum to minimum uniformity of 0.4 dB. This device has applications in future narrow linewidth laser systems and parallel distribution of filtered signals. A variation of the ULLW platform was outlined, and the results of a novel dual-layer waveguide technology that has low propagation loss regions and low bend radius regions was presented. The TE loss was 0.48 ± 0.10 dB/m on the single stripe regions, 20.1 ± 0.3 dB/m for high contrast regions down to a 300 µm bend radius, with a transition loss of 0.35 ± 0.06 dB/taper.

Low perturbation gratings using post structures and sidewall variation on ULLWs was then presented. The κ values ranged from 0.23 cm^{-1} to 1.2 cm^{-1}, with bandwidths of 74 pm to 116 pm. We have also demonstrated λ/4-shifted gratings with a Q_{load} of 204 thousand, suitable for DFB style lasers and other systems relying on high Q single mode filters.

We then presented a PDH frequency stabilization system using a heterogeneous Si/III-V CRR laser, waveguide coupled Si_3N_4 resonator, and appropriate feedback electronics. The high frequency FM noise is measured to be 60×10^3 Hz^2/Hz consistent with a 160 kHz linewidth. Within the loop bandwidth of the PDH lock, the low frequency noise is suppressed up to 33 dB, to 10^3 Hz^2/Hz. The ultra-high Q Si_3N_4 cavity allows for $60\times$ reduction of noise below the spontaneous emission noise of the laser, making it very promising for further integration work. Lower coupling losses on a monolithic platform will improve the system performance, and programmable electronics in closer proximity to the devices will allow for higher loop bandwidths and noise suppression. Integrated linewidths of monolithic frequency locked lasers of 100 Hz was envisioned.

7.2 *Future Work*

7.2.1 Integration of Platforms

We have touched briefly on the silicon on ultra-low loss (SOUL) platform in the introduction, and will highlight a few specific PICs that are very interesting given the results presented. We highlight some integration feats from UCSB in Figure 7.1, and all of these components can be integrated on a single monolithic platform for microwave photonic applications. These systems would use Si_3N_4 for delay lines and high Q resonators, heterogeneous Si/III-V for high powered lasers, modulators, and detectors on the SOUL platform, and finally a CMOS or Si-Ge based electronics chip that has been demonstrated in [1]. The integration of platforms would allow for reduction in inter-component coupling losses, reduced spurious facet reflections, and improved performance by utilizing the best material platforms available.
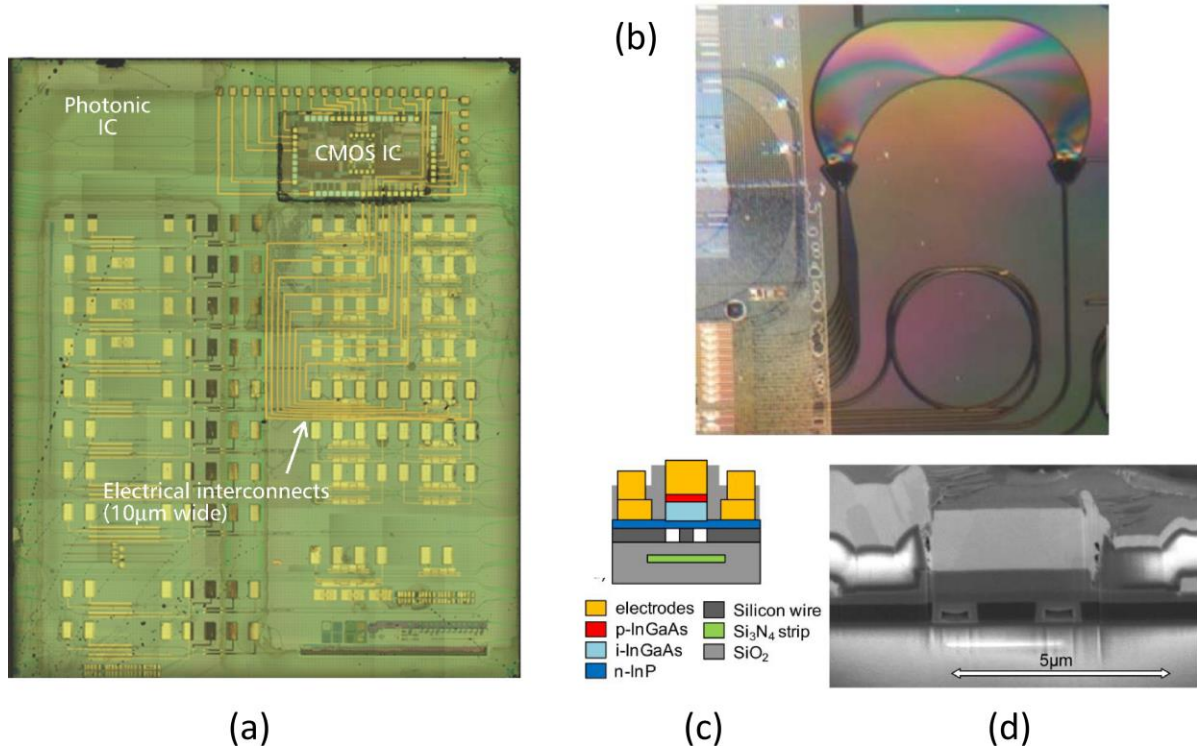
Figure 7.1) (a) CMOS electronics integrated with photonic switch network [1] © 2013 IEEE. Si$_3$N$_4$ AWG integrated with heterogeneous Si/III-V photodetectors, (b) top down photograph, (c) layer schematic, (d) SEM of cross section from [2] © 2013 IEEE.

7.2.2 Resonant Optical Gyroscope

The high Q factor of the ULLW ring resonators makes them very attractive for future integrated sensors that require high sensitivity in a compact package. Any variation in refractive index, either through the Sagnac effect under rotation or n_{eff} change when the optical mode is perturbed with a gas or particulate, will have an enhanced sensitivity due to the resonator's high frequency (and phase) to amplitude conversion efficiency. For an example of a gas sensor application with ULLW resonator, see [3]. Here we will overview the benefits of implementing the ULLW resonators in a resonant waveguide optical gyroscope (RWOG), also called resonant micro-optic gyroscope (RMOG).

86

For each order, m, of a resonator, the rotational Sagnac effect produces a splitting of modes ($\Delta \nu$) in counter-propagating directions that is proportional to the area (A), length (L), optical mode frequency (f_m), and rotation rate (Ω) in the plane of the resonator:

$$\Delta \nu = \frac{4Af_m}{cL}\Omega \xrightarrow{circular} \frac{2Rf_m}{c}\Omega \qquad (7.1)$$

To detect the mode splitting, one can essentially build PDH feedback loops to detect the shift in the frequency domain, or other readout systems based on acousto-optic modulators and lock-in amplifiers [4]. A laser's output is split and sent in each counter-propagating direction and to photodetectors. The shot noise limited performance (angular random walk) is then limited by the Q*L product and optical power hitting the detector (P_{PD}) at a responsivity ($\Re$) in the detection bandwidth (B) [5]:

$$\delta \Omega = \frac{\sqrt{2}c}{QL}\sqrt{\frac{Bhf_m}{\eta_{PD}P_{PD}}} = \frac{\sqrt{2}c}{QL}\sqrt{\frac{Bq}{\Re P_{PD}}} \qquad (7.2)$$

The main advantage of the RWOG over a delay line gyroscope is the theoretically higher resolution for a given area by a factor of $\frac{Finesse}{2\sqrt{2}}$ [6], but nonlinearities such as backscatter and bias drift instabilities are still an issue when using a narrow linewidth laser for detection. Figure 7.2 plots the attainable shot noise sensitivity versus Q factor and ring radius, assuming 1-10 mW P_{PD}. The ULLW resonator has an achievable 1 deg/hr sensitivity, which is very attractive for automotive and even space grade navigational systems.
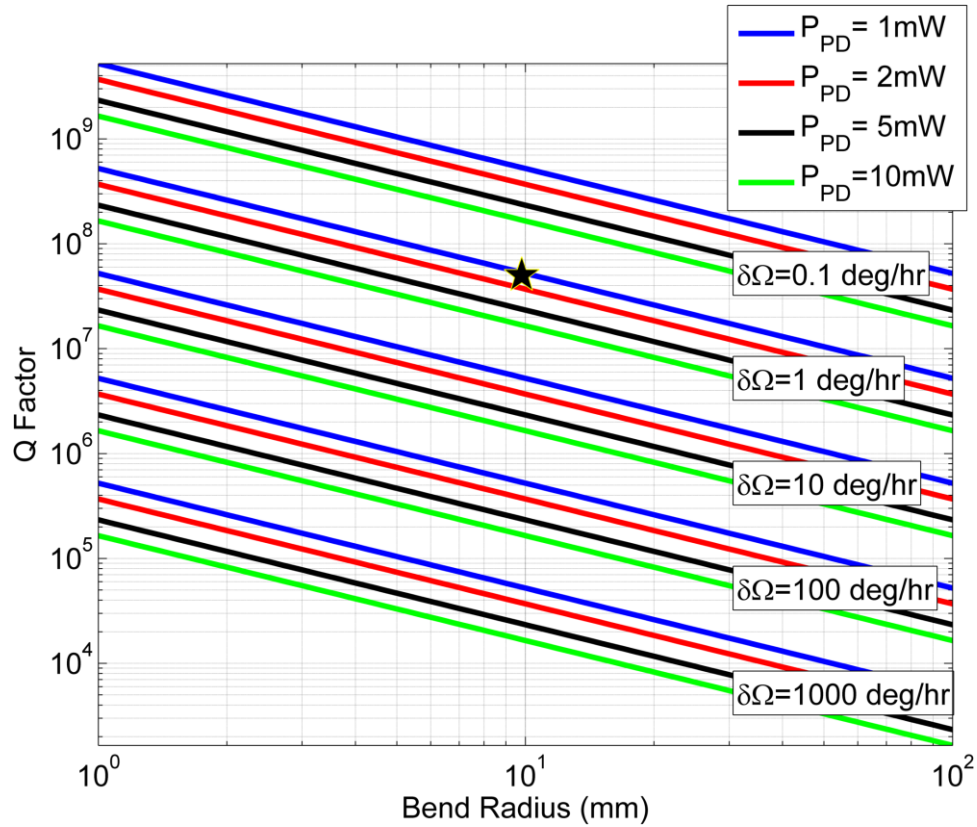
Figure 7.2) Ring gyroscope sensitivity (δΩ) across detector powers (P$_{PD}$) for a given circular resonator versus Q factor and bend radius. The work of this thesis is highlighted with a star.

7.2.3   Photonic Microwave Generator

Microwave photonic systems can generally be defined as optoelectonic links that utilize the superior spectral qualities of optical elements to produce or detect high S/N microwave signals. Since infrared optics operates at 193 THz, microwave signals are added to the envelope of the optical carrier, and then manipulated by, for instance, long fiber delays or high Q factor filtering. After this, the signal is detected on a photodetector, which downconverts the signal to the microwave domain. One immediate application of the low frequency noise lasers of this work is in microwave generation. Mixing two narrowly tunable lasers, such as PDH locked CRR lasers, and beating them on a high speed photodetector

produces a microwave signal at the difference in optical frequency of the lasers, as shown in
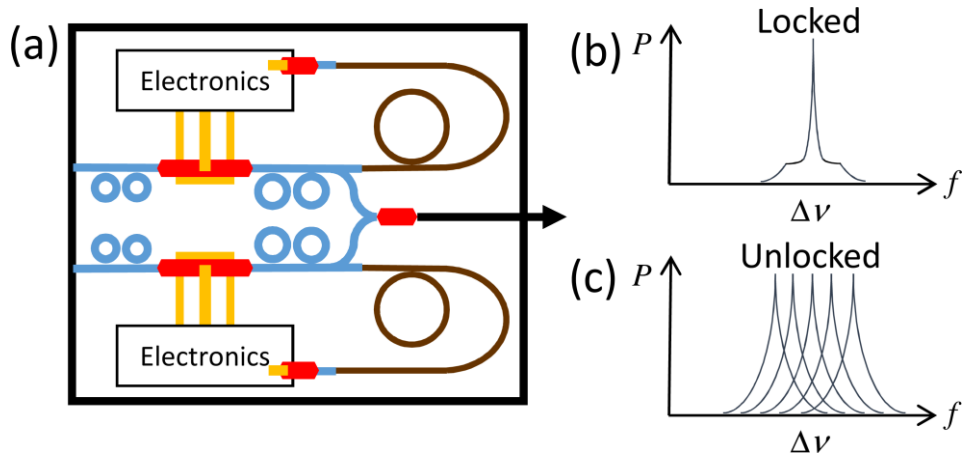
Figure 7.3

Figure 7.3) (a) Schematic of a dual PDH microwave generator with fully integrated Si/III-V/Si₃N₄/CMOS utilizing CRR lasers and high Q resonators. (b) Locked output with negligible drift and lower frequency noise compared to the (c) unlocked case.

The phase noise of this generated carrier is critical in many applications, as it will

deteriorate the S/N of systems such as radar and reference clocks that rely on low frequency

signals. The heterodyne beat note has a phase noise that is the convolution of the two lasers'

phase noise, generally quoted as single sideband PSD of phase fluctuations (S_φ) with units of

rad^2/Hz.

$$S_\phi = S_{\phi 1} \otimes S_{\phi 2} \tag{7.3}$$

This is related to the previously measured frequency noise PSD (S_v) through a time derivate

in power, or $(-j2\pi f)^2$ term, where f is the Fourier (offset) frequency. For example, a white

FM PSD, such as found in Lorentzian laser linewidths, would have a $1/f^2$ slope in phase

noise PSD.

$$S_v = f^2 S_\phi \tag{7.4}$$

By utilizing the PDH system, the resonator stability is transferred the laser, and the phase noise of the microwave signal is reduced via the electronic feedback loop. In addition, the tunable lasers allow for generation of microwave signals as high as the photodetector can operate, currently nearing 80 GHz.

7.2.4   Optoelectronic Oscillator

A second type of microwave photonic generator that would benefit from high optical Q factors is the optoelectronic oscillator (OEO). Essentially, the PDH system is operated at much higher modulation frequencies to produce signals at multiples of the resonator FSR. The electronic feedback loop is operating at GHz speeds, and the feedback is fed back to an intensity or phase modulator. The greater the loop delay of the system, the lower the phase noise of the system will be. The benefit of a high Q factor is that many closely spaced modes can be filtered out by the resonator if the delay line is very long. Using the previously mentioned integration of platforms, a system such as this is possible with high power lasers, modulators, ULLWs, detectors, and closely integrated electronics. Such an integrated OEO system is shown in Figure 7.4
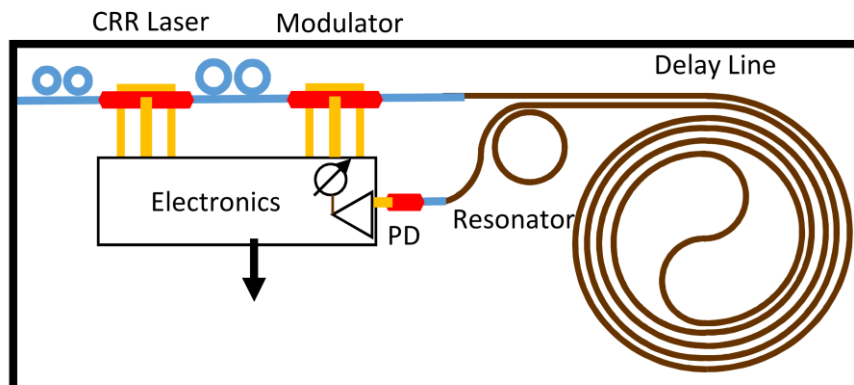

Figure 7.4) Integrated OEO schematic

The phase noise reduction for such a combined resonator and delay line system can be modeled from [7]:

$$S_\phi = \frac{1+(2\pi f \tau_{delay})^2}{2-2\cos(2\pi f \tau_{delay})+(\frac{2fQ_{\mu wave}}{\nu_{\mu wave}})^2+\frac{4fQ_{\mu wave}}{\nu_{\mu wave}}\sin(2\pi f \tau_{delay})} RN \qquad (7.5)$$

where τ_{delay} is the delay time, Q is the microwave Q factor, and $\nu_{\mu wave}$ is the microwave operating frequency, and RN is the residual noise occurring from shot, thermal, and flicker noise sources of the system. The phase noise spectrum is presented in Figure 7.5, where adding a 100 m delay reduces phase noise beyond the overall Q filtering of the system (the Leeson frequency), but adds closely spaced sidemodes in the process. The high Q resonator adds an additional delay and filters out the sidemodes and for stable, single mode operation. A low Q electronic filter is easily implemented to filter out the very high frequency sidemodes located at the resonator's FSR.
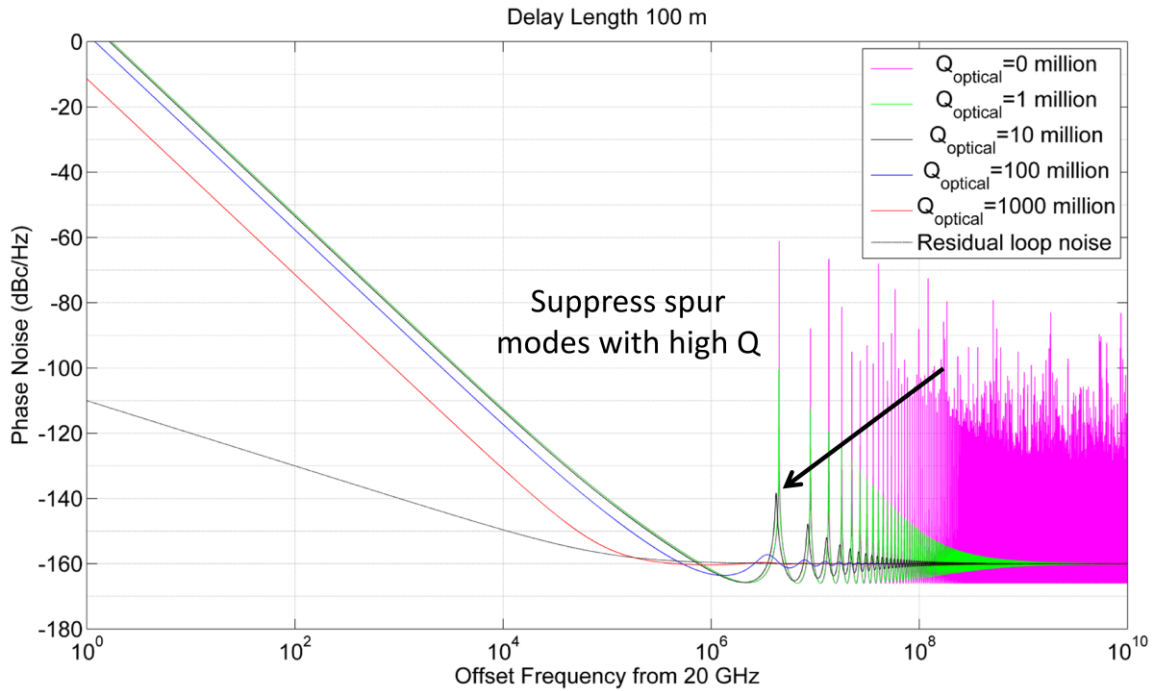
Figure 7.5) Modeled OEO phase noise output with a delay line of 100 m, residual noise floor of -160 dBc/Hz, and various optical Q factors.

7.3   References

[1]   L. Chen, A. Sohdi, J. E. Bowers, L. Theogarajan, J. Roth, and G. Fish, "Electronic and photonic integrated circuits for fast data center optical circuit switches," *IEEE Communications Magazine*, vol. 51, no. 9, pp. 53–59, 2013.

[2]   M. Piels, J. F. Bauters, M. L. Davenport, M. J. R. Heck, and J. E. Bowers, "Low-Loss Silicon Nitride AWG Demultiplexer Heterogeneously Integrated With Hybrid III– V/Silicon Photodetectors," *J. Light. Technol.*, vol. 32, no. 4, pp. 817–823, Feb. 2014.

[3]   J. F. Bauters, "Ultra-Low Loss Waveguides with Application to Photonic Integrated Circuits," 2013.

[4]   M. Armenise, C. Ciminelli, F. Dell'Olio, and V. Passaro, *Advances in Gyroscope Technologies*. Heidelberg: Springer-Verlag Berlin Heidelberg, 2010.

[5]   C. Ciminelli, F. Dell'Olio, M. N. Armenise, F. M. Soares, and W. Passenberg, "High performance InP ring resonator for new generation monolithically integrated optical gyroscopes," *Opt. Express*, vol. 21, no. 1, pp. 556–564, Jan. 2013.

[6]   S. Ezekiel, S. P. Smith, and F. Zarinetchi, "Basic Principles of Fiber-Optic Gyroscopes," in *Optical Fiber Rotation Sensing*, W. K. Burns, Ed. San Diego, CA: Academic Press, 1994.

[7]   E. Rubiola, *Phase Noise and Frequency Stability in Oscillators*. Cambridge, UK: Cambridge University Press, 2009.